

The aerodynamic diameter and specific surface area of branched chain-like aggregates

Citation for published version (APA):

Kops, J. A. M. M. (1976). *The aerodynamic diameter and specific surface area of branched chain-like aggregates*. [Phd Thesis 1 (Research TU/e / Graduation TU/e), Applied Physics and Science Education]. Technische Hogeschool Eindhoven. <https://doi.org/10.6100/IR2424>

DOI:

[10.6100/IR2424](https://doi.org/10.6100/IR2424)

Document status and date:

Published: 01/01/1976

Document Version:

Publisher's PDF, also known as Version of Record (includes final page, issue and volume numbers)

Please check the document version of this publication:

- A submitted manuscript is the version of the article upon submission and before peer-review. There can be important differences between the submitted version and the official published version of record. People interested in the research are advised to contact the author for the final version of the publication, or visit the DOI to the publisher's website.
- The final author version and the galley proof are versions of the publication after peer review.
- The final published version features the final layout of the paper including the volume, issue and page numbers.

[Link to publication](#)

General rights

Copyright and moral rights for the publications made accessible in the public portal are retained by the authors and/or other copyright owners and it is a condition of accessing publications that users recognise and abide by the legal requirements associated with these rights.

- Users may download and print one copy of any publication from the public portal for the purpose of private study or research.
- You may not further distribute the material or use it for any profit-making activity or commercial gain
- You may freely distribute the URL identifying the publication in the public portal.

If the publication is distributed under the terms of Article 25fa of the Dutch Copyright Act, indicated by the "Taverne" license above, please follow below link for the End User Agreement:

www.tue.nl/taverne

Take down policy

If you believe that this document breaches copyright please contact us at:

openaccess@tue.nl

providing details and we will investigate your claim.

THE AERODYNAMIC DIAMETER
AND
SPECIFIC SURFACE AREA OF
BRANCHED CHAIN - LIKE AGGREGATES

J. A. M. M. KOPS

THE AERODYNAMIC DIAMETER
AND
SPECIFIC SURFACE AREA OF
BRANCHED CHAIN - LIKE AGGREGATES

PROEFSCHRIFT

TER VERKRIJGING VAN DE GRAAD VAN DOCTOR IN DE
TECHNISCHE WETENSCHAPPEN AAN DE TECHNISCHE
HOGESCHOOL EINDHOVEN, OP GEZAG VAN DE RECTOR
MAGNIFICUS, PROF.DR. P. VAN DER LEEDEN, VOOR EEN
COMMISSIE AANGEWEEZEN DOOR HET COLLEGE VAN
DEKANEN IN HET OPENBAAR TE VERDEDIGEN OP
DINSDAG 28 SEPTEMBER 1976 TE 16.00 UUR

DOOR

JOANNES ARNOLDUS MARCUS MARIA KOPS

GEBOREN TE OOSTERHOUT (N.BR.)

DIT PROEFSCHRIFT IS GOEDGEKEURD DOOR DE PROMOTOREN

PROF. DR. D.A. DE VRIES

EN

PROF. DR. W. STÖBER (MÜNSTER)

Grote dank ben ik verschuldigd aan de directie van het Reactor Centrum Nederland voor de gelegenheid die ze me hebben geboden om de studie , welke ten grondslag ligt aan dit proefschrift, te verrichten. Bovendien dank ik de directie van Ultra - Centrifuge Nederland N.V. voor de gegeven medewerking bij de tot stand koming van dit proefschrift.

Mijn bijzondere erkentelijkheid gaat uit naar de leden van de aerosol-groep van het R.C.N., onder leiding van Joop van de Vate. In het bijzonder dank ik Govert Dibbets, Leo Hermans, Cor Roet voor de uitvoering van de experimenten, en Dick Pouw voor diens waardevolle commentaar.

Dankbaar heb ik gebruik gemaakt van het commentaar van prof.dr.D.A. de Vries en prof.dr.W.Stöber.

Veel waardering heb ik voor de uitvoering van het typewerk, dat werd verzorgd door mevr. A. Schuyt-Fasen

De reprografische dienst van het R.C.N. onder leiding van de heer van Rooy dank ik voor de druktechnische uitvoering.

De studie gerapporteerd in dit proefschrift werd gesubsidieerd door het ministerie van Volksgezondheid en Milieuhygiëne.

Aan mijn ouders,
Jeanni en Stephanie

CONTENTS

1. INTRODUCTION	7
2. THEORY	12
2.1. Fluid drag on spherical particles in creeping motion	12
2.2. Fluid drag on non-spherical particles in creeping motion ...	15
3. CALIBRATION OF A STÖBER CENTRIFUGAL AEROSOL SPECTROMETER	23
3.1. Introduction	23
3.2. Theory	26
3.3. Materials and methods	28
3.4. Results	32
3.4.1. <i>Calibration experiments</i>	32
3.4.2. <i>The influence of the cooling system</i>	34
3.5. Discussion	36
4. THE AERODYNAMIC DIAMETER OF BRANCHED CHAIN - LIKE AGGREGATES ...	40
4.1. Introduction	40
4.2. Materials and methods	42
4.2.1. <i>Aerosol generation</i>	42
4.2.2. <i>Measurement of the primary particle size</i> <i>distribution</i>	44
4.2.3. <i>Experimental procedure</i>	47
4.3. Results	49
4.3.1. <i>Primary particle size distribution</i>	49
4.3.2. <i>The aerodynamic diameter</i>	52
4.4. Discussion	63
4.4.1. <i>Linear aggregates</i>	64
4.4.2. <i>Threedimensional networks</i>	66
4.4.3. <i>The transition from linear aggregates to</i> <i>threedimensional networks</i>	69
4.4.4. <i>Comparison with literature data</i>	71
4.4.5. <i>Discussion of errors</i>	73
4.5. Concluding remarks	75

5. THE SPECIFIC SURFACE AREA OF BRANCHED CHAIN - LIKE AGGREGATES	76
5.1. Introduction	76
5.2. Materials and methods	77
5.2.1. <i>Specific surface area from gas adsorption</i>	77
5.2.2. <i>Experimental procedure</i>	81
5.3. Results and discussion	83
5.4. Conclusion	88
APPENDIX I. METHODS FOR MEASURING THE AERODYNAMIC DIAMETER	89
I.1. Introduction	89
I.2. Methods	90
I.2.1. <i>Electric mobility spectrometers</i>	90
I.2.2. <i>Millikan chambers and elutriators</i>	93
I.2.3. <i>Centrifuges</i>	96
I.2.4. <i>Impactors</i>	98
I.3. Systematic errors	101
I.4. Conclusion	104
APPENDIX II. THE POINT TO PLANE ELECTROSTATIC PRECIPITATOR	105
REFERENCES	107
LIST OF FREQUENTLY USED SYMBOLS	113
SUMMARY	115
SAMENVATTING	117
CURRICULUM VITAE	119

1. INTRODUCTION

An aerosol can be defined as a suspension of liquid or solid particles in a gas. Strictly speaking the word aerosol implies that the gas phase is air, but it is common practice to use the term aerosol in all cases where particles are suspended in a gas, irrespective of its nature. A comprehensive treatment of the problem of nomenclature in aerosol physics has been given by Preining [79].

Aerosols play an important role in nature and human life. So for instance, patients suffering from lung diseases take medicines in the form of aerosols by inhalation. Also in meteorology aerosols play an important role, for instance in the formation of clouds.

Nowadays aerosol research is more and more focussed on the role of aerosols in the problem of air pollution. So manmade as well as natural aerosols will play a role in the formation of photochemical smog [89], and on the other hand aerosols are produced during photochemical smog formation [78,83,90]. Many chemical processes in the atmosphere are catalysed by aerosols [9,14,44,69] and some chemical processes in the atmosphere would not occur in the absence of aerosols.

The above mentioned effects illustrate the role of aerosols in the so-called secondary air pollution. Apart from this, aerosols have a large direct impact on the quality of the air, as far as they represent a real hazard on inhalation. Particles of inhaled aerosols are deposited in the respiratory tract. The harmfulness of the inhaled particles depends on the particle material, the gases adsorbed on the particle surface, and last but not least on the location of deposition of the particles in the respiratory tract. Particles deposited down to the terminal bronchioli (cf. figure 1.1) are mainly removed by a natural protection mechanism (cilia which are moving upwards a film of mucus). However, the protection mechanism of the alveolated airways is much less effective. Therefore particles deposited in the alveolated airways may damage the lung walls, or they may dissolve and be transported to the blood stream.

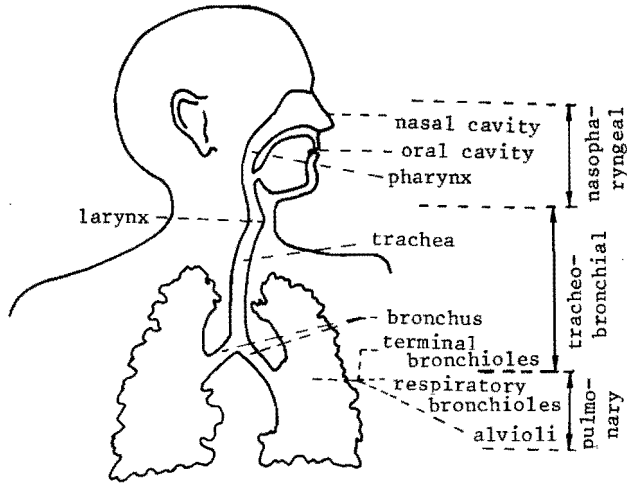


Figure 1.1. Schematic diagram of the respiratory tract.

The fact that inhaled particles can be the cause of lung diseases was firstly recognized in the mining industry, where in former days miners contracted silicosis because of frequent inhalation of quartz particles. Since that time research has been done in the field of aerosol inhalation, but at the moment the particle deposition in the lungs is not yet entirely understood. A widely accepted model of the deposition of particles in the respiratory tract is given by the Task Group on Lung Dynamics of the I.C.R.P. [10]. According to this model the deposition of inhaled particles is, apart from the physiology of respiration and the anatomy of the respiratory tract, governed by the aerodynamic diameters of the particles. The aerodynamic diameter of a particle is defined as the diameter of a sphere of unit density, *) having the same settling rate under influence of gravity as the particle in question. Figure 1.2 shows a diagram of the model given by the Task Group on Lung Dynamics. This model gives a somewhat simplified picture of the particle deposition in the lungs, and there is some discrepancy with other findings [18,19,34].

*) As the unit one chooses 1 g.cm^{-3} .

Nevertheless the model illustrates that a proper hazard evaluation of atmospheric aerosols should involve both a chemical and a physical (aerodynamic) characterisation. As to aerodynamic characterisation of an aerosol a distinction has to be made between macroscopic and microscopic characteristics. The macroscopic characterisation involves the determination of the aerodynamic diameter distribution of the aerosol particles [10,20,45,57], while the microscopic characterisation is the determination of the relation between the aerodynamic diameter and the microstructure of the particles.

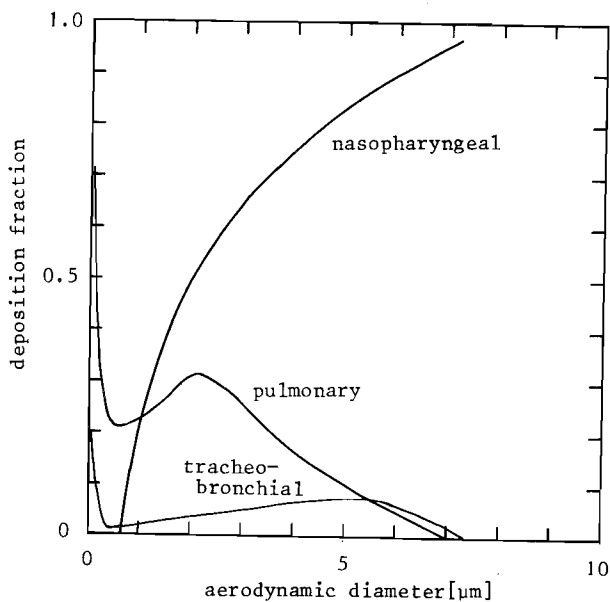


Figure 1.2. Particle deposition in the respiratory tract according to the Task Group on Lung Dynamics [101], 15 resp./min.; tidal volume 1450 cm³.

This thesis deals mainly with the microscopic aerodynamic characterisation of chain-like aggregates. In addition the specific surface area of these aggregates is considered. These chain-like aggregates are produced for instance by combustion of hydrocarbon fuels (in automobile engines) and the condensation of metallic vapors (near iron works). The chain-like

aggregates studied by us were produced by means of an exploding wire, which method is described in chapter 4. Aerosol particles produced in this way are rather similar to atmospheric chain-like aggregates as is shown in figure 1.3, which shows an electron microscope picture of an iron oxide aggregate produced by means of an exploding wire, as well as an electron microscope picture of an iron oxide aggregate sampled in the neighbourhood of the "Hoogovens" (iron works in IJmuiden, The Netherlands).

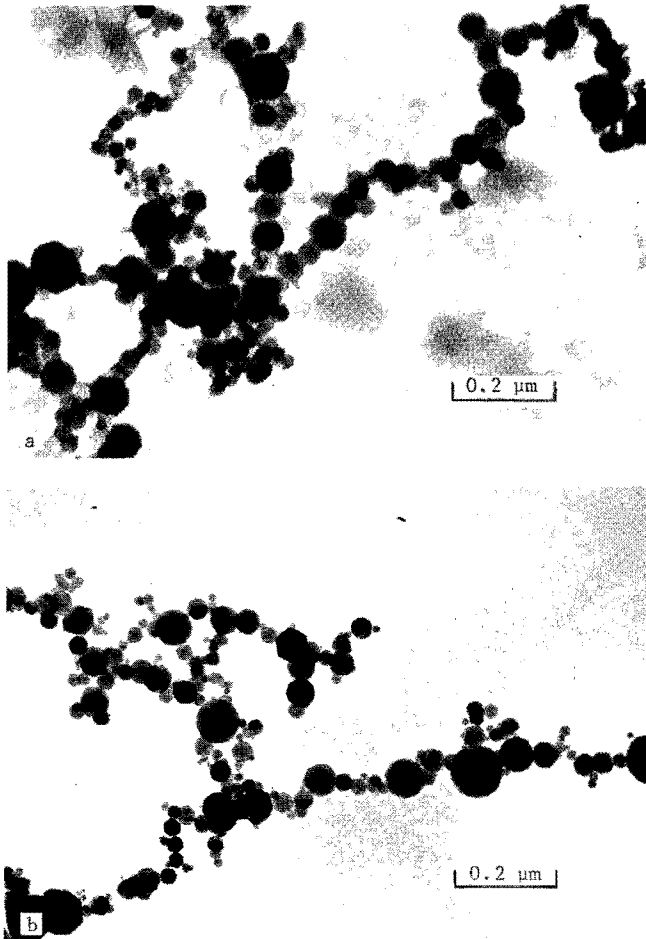


Figure 1.3. a: Electron microscope picture of an atmospheric iron oxide aggregate.

b: Electron microscope picture of an iron oxide aggregate produced by an "exploding wire".

In chapter 2 of this thesis the theoretical background of the fluid drag on spherical as well as non-spherical particles is discussed.

In order to allow a microscopic aerodynamic characterisation of the branched chain-like aggregates, in this study these aggregates were separated according to their aerodynamic diameter with an aerosol centrifuge according to Stöber and Flachsbart [95]. The calibration of this instrument is described in chapter 3.

The study dealing with the microscopic aerodynamic characterisation of the aggregates is reported in chapter 4. The results show that two classes can be distinguished, viz. linear aggregates, and threedimensional networks. The corresponding microscopic aerodynamic characteristics agree with literature data obtained for respectively linear and cluster aggregates of monodisperse polystyrene spheres.

The specific surface area of the aggregates is determined from adsorption isotherms of Kr at 78.8 K by means of the B.E.T. adsorption theory, which is reported in chapter 5. The results of these experiments agree fairly well with the surface area calculated from the geometric dimensions of the particles.

2. THEORY

2.1. Fluid drag on spherical particles in creeping motion ($Re < 0.1$)

The resistance of a gas to the motion of a spherical particle depends on the ratio of the mean free path (\bar{l}) of the gas molecules to the particle radius ($\frac{1}{2}d$), which ratio is called the Knudsen number ($Kn = 2\bar{l}/d$). Up to now, only in the two limiting regions (viz. $Kn \gg 1$ and $Kn \ll 1$) theoretical formulae could be obtained for the resistance of a gas to the motion of a sphere.

For spheres with a diameter much smaller than \bar{l} ($Kn \gg 1$), it can be assumed that the particle does not disturb the Maxwellian velocity distribution of the gas molecules. In that case the effect of the collisions of the particle and the gas molecules yields the following expression for the fluid drag:

$$F = - \frac{6\pi\eta d^2 v}{4(A+Q)\bar{l}} \quad (2.1.1)$$

with: F = resistance of the gas to the moving sphere,
 η = dynamic viscosity of the gas,
 v = velocity of the sphere,

A and Q = factors, depending on the nature of the molecule-particle interaction (the accommodation coefficients for momentum and energy [113]).

For spheres with a diameter much larger than \bar{l} ($Kn \ll 1$), the gas can be considered as a continuum, so that the fluid drag on the sphere is given by the well known Stokes formula:

$$F = -3\pi\eta d v \quad (2.1.2)$$

The Stokes formula only holds for Reynolds numbers below about 0.1 (creeping motion), which condition is mostly fulfilled in aerosols.

Formulae (2.1.1) and (2.1.2) describe fairly well the fluid drag on a sphere in the limiting regions. In the intermediate region equation (2.1.1) does not hold, because the particles are so large compared to \bar{l} , that they seriously disturb the Maxwellian velocity distribution of the gas molecules. The Stokes formula does not hold in this region, because the spheres are not large enough to justify the continuum model, according to which no slip occurs at the particle surface.

A theoretical treatment of the particle-gas interaction in the intermediate region is extremely complicated. It is therefore not surprising that theoretical studies up to now are confined to the near-continuum flow region and the near-free molecular region [113]. The results of De Wit [113] show a strong influence of the accommodation coefficients

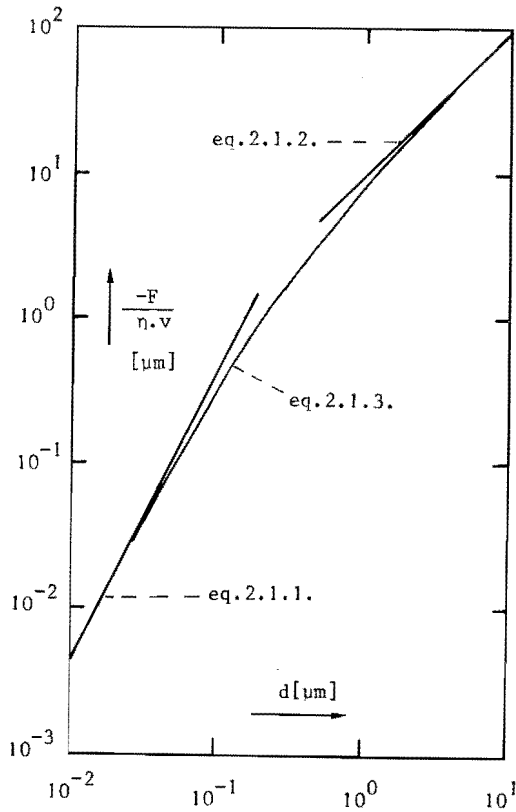


Figure 2.1. Relation between $-F/\eta v$ and d according to equations (2.1.1), (2.1.2) and (2.1.3).

for tangential momentum and energy. No methods exist for an accurate determination of these accommodation coefficients. Hence, the applicability of the theoretical results is limited even in the near-continuum and near-free molecular regions. In the intermediate region interpolation formulae have to be used. Generally the empirical formula of Knudsen and Weber [49] is applied to describe the fluid drag in this region. This formula, which fits experimental results quite well, reads:

$$F = - \frac{3\pi\eta d v}{C_s(d)} \quad (2.1.3)$$

where $C_s(d)$, the so-called slip correction factor, is given by:

$$C_s(d) = 1 + A \frac{2\bar{l}}{d} + Q \frac{2\bar{l}}{d} \exp\left[-\frac{Bd}{2\bar{l}}\right] \quad (2.1.4)$$

and A, B and Q are empirical factors. For particles moving in air (for which $\bar{l} = 6.53 \times 10^{-8}$ m at 300 K and atmospheric pressure) mostly the values obtained by Millikan [66] for oil drops are used. These are:

A = 1.246; B = 0.87; and Q = 0.42.

Formula (2.1.3) together with (2.1.4) approaches (2.1.2) for large values of d, while it approaches (2.1.1) for small values of d, as is illustrated graphically in figure 2.1.

More recently Fuchs and Stechkina [27], by means of crude assumptions / theoretically derived an alternative expression for $C_s(d)$, viz.:

$$C_s(d) = \left\{1 + a\left(\frac{2\bar{l}}{d}\right)\right\}^{-1} + b \frac{2\bar{l}}{d} \quad (2.1.5)$$

where a and b are constants depending on the nature of the gas and the particle surface. They must be found experimentally. From Millikan's data [66] one finds for oil drops falling in air: a = 0.42 and b = 1.76. Formula (2.1.5) does not describe experimental results better than (2.1.4) does. Therefore the Fuchs-Stechkina formula up to now has only been used incidentally [80]. In the present study the Knudsen-Weber formula will be employed.

2.2. Fluid drag on non - spherical particles in creeping motion ($Re < 0.1$)

A theoretical treatment of the behaviour of non-spherical particles is very complicated. Therefore the fluid drag on non-spherical particles is related to that on spherical particles by the introduction of a dynamic shape factor (κ). This factor is defined as the ratio of the resistance of a gas to the motion of the particle under consideration and the resistance to a spherical particle having the same volume and velocity.

The dynamic shape factor will be a function of the orientation of the particle with respect to the direction of the motion, of the Knudsen-number, and sometimes even of the Reynoldsnumber as will be shown below.

Using the dynamic shape factor together with equation (2.1.3) one has for the resistance of a gas to the motion of a non-spherical particle:

$$F = - \frac{3\pi\eta d_e \kappa v}{C_s(d_e)} \quad (2.2.1)$$

where d_e is the so-called volume equivalent diameter (i.e. the diameter of sphere having the same volume as the particle in question).

Theoretical computations of dynamic shape factors will only be possible for particles with a regular shape. Up to now exact mathematical results are known only for spheroids (i.e. ellipsoids with an axis of rotational symmetry) in the continuum flow region. These results have been obtained [61] from Overbeck's solution [73] of the fluid drag on ellipsoids in creeping motion. They confirm that the dynamic shape factor of a spheroid depends on its orientation with respect to the direction of the motion. According to these results the dynamic shape factor of an oblate spheroid (ratio of polar diameter and equatorial diameter = $q < 1$) moving in the direction of its polar axis, is given by:

$$\kappa_{0II} = \frac{4}{3}(1-q^2) q^{-1/3} \left\{ \left(\frac{1-2q^2}{\sqrt{1-q^2}} \right) \arccos q + q \right\}^{-1} \quad (2.2.2)$$

while the dynamic shape factor of an oblate spheroid moving in a direction perpendicular to its polar axis, is given by:

$$\kappa_{0I} = \frac{8}{3}(1-q^2) q^{-1/3} \left\{ \left(\frac{3-2q^2}{\sqrt{1-q^2}} \right) \arccos q - q \right\}^{-1} \quad (2.2.3)$$

The dynamic shape factor of a prolate spheroid ($q > 1$) moving in the direction of its polar axis is:

$$\kappa_{p\parallel} = \frac{4}{3}(q^2-1) q^{-1/3} \left\{ \left(\frac{2q^2-1}{\sqrt{q^2-1}} \right) \ln(q + \sqrt{q^2+1}) - q \right\}^{-1} \quad (2.2.4)$$

and for motion perpendicular to its polar axis,

$$\kappa_{p\perp} = \frac{8}{3}(q^2-1) q^{-1/3} \left\{ \left(\frac{2q^2-3}{\sqrt{q^2-1}} \right) \ln(q + \sqrt{q^2-1}) + q \right\}^{-1} \quad (2.2.5)$$

The mathematical expressions given above can be simplified for small and large values of q , corresponding with spheroidal discs and spheroidal needles respectively.

Experimental results of McNown and Malaika [61] are in agreement with formulae (2.2.2) to (2.2.5).

Other theoretical studies of the fluid drag on non-spherical particles mainly deal with circular cylinders. For instance Burgers [7] derived for continuum flow ($Kn = 0$) an approximate expression for the fluid drag on a circular cylinder moving parallel to its axis. From his result the dynamic shape factor ($\kappa_{c\parallel}$) can be calculated.

$$\kappa_{c\parallel} = 0.58 \left(\frac{L}{d_c} \right)^{2/3} \left\{ \ln \left(\frac{2L}{d_c} \right) - 0.72 \right\}^{-1} \quad (2.2.6)$$

where L is the length and d_c is the diameter of the cylinder.

The fluid drag on an infinitely long circular cylinder in creeping motion ($Re \lesssim 0.1$) in a direction perpendicular to its axis has been obtained theoretically for the continuum flow region by Lamb [54] and Davies [21] by means of Oseen's approximation [33]. Pich [75] obtained an approximate solution for arbitrary Kn and $Kn \times Re \ll 1$. He assumed a small layer around the cylinder in which the flow has a molecular character while beyond that layer continuum flow was assumed for which he applied Oseen's method. According to Pich's result, the fluid drag, F' , per unit length of the cylinder is given by:

$$F' = -4\pi\eta v \{ 2.0022 - \ln Re + 1.747 Kn - \ln(1 + 0.749 Kn) \}^{-1} \quad (2.2.7)$$

where $Re = d_c \rho_g v / \eta$, ρ_g = fluid density, $Kn = 2\bar{l} / d_c$, and $Kn \times Re \ll 1$.

The results of Lamb and Davies follow from (2.2.7) by taking Kn equal to zero. Although (2.2.7) has been derived for infinitely long cylinders, it can be assumed to be also applicable to finite cylinders with a length much larger than the diameter. In that case the dynamic shape factor ($\kappa_{c\perp}$) is given by:

$$\kappa_{c\perp} = 1.16 \left(\frac{L}{d_c}\right)^{2/3} \cdot C_s(d_e) \times \\ \times \{2.0022 - \ln Re + 1.747 Kn - \ln(1 + 0.749 Kn)\}^{-1} \quad (2.2.8)$$

The continuum flow version of (2.2.7) has been verified experimentally by Finn [25]. However, White [111] found experimentally that the applicability of Lamb's and Davies' result is limited due to the inevitably finite extent of the fluid. According to White at $Re = 10^{-3}$ the continuum flow version of (2.2.7) becomes applicable if walls are some 10,000 cylinder diameters away, which distance increases with decreasing Re. The solution of Pich agrees fairly well with experimental results of Coudeville et al. [13].

Because for large values of q prolate spheroids do not differ much in shape from cylinders, it is interesting to compare the results obtained for prolate spheroids with those derived for cylinders.

The dynamic shape factor of a cylinder moving parallel to its axis according to Burgers' equation (2.2.6) agrees fairly well indeed with the dynamic shape factor of a prolate spheroid moving parallel to its polar axis (eq. 2.2.4) as is shown in figure 2.2.

The dynamic shape factor of a prolate spheroid moving in a direction perpendicular to its polar axis, as given by eq. (2.2.5) has been obtained for continuum flow ($Kn = 0$). Therefore (2.2.5) must be compared with the continuum flow version of eq. (2.2.8). However, such a comparison is complicated by the fact that the dynamic shape factor as given by (2.2.8) depends on Re, which means that no unique relation between $\kappa_{c\perp}$ and L/d_c can be given. In figure 2.2 the relation between $\kappa_{c\perp}$ and L/d_c is shown graphically for several values of Re.

Figure 2.2 shows a rather considerable discrepancy between $\kappa_{c\perp}$ and $\kappa_{p\perp}$. Nevertheless, both relations are supported by experimental results [25,61,111]. From this it must be concluded that the validity of the analytical expressions of dynamic shape factors obtained for spheroids and circular cylinders is limited to a certain range of respectively q

and L/d_c as well as Re . However, too few experimental results are available to determine the validity limits of these expressions.

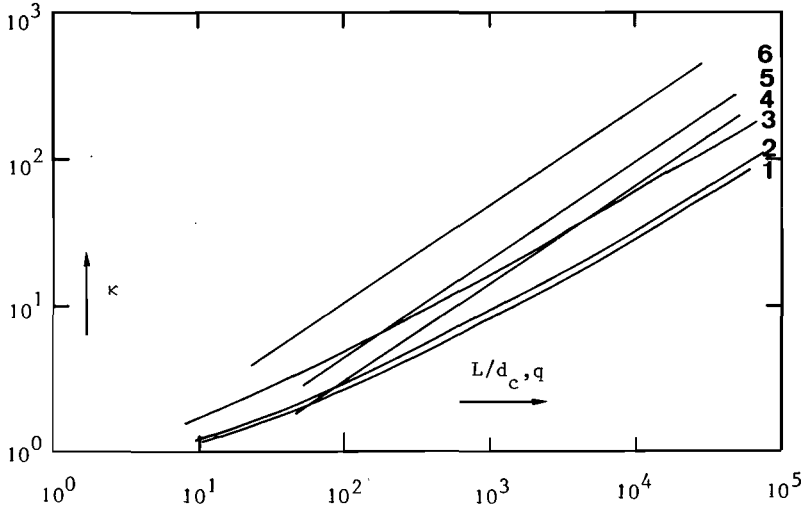


Figure 2.2. Dynamic shape factor of prolate spheroids and cylinders in dependence of the ratio of their axes (q for spheroids, and L/d_c for cylinders).

- 1: $\kappa_{p//}$ according to equation (2.2.4);
- 2: $\kappa_{c//}$ according to equation (2.2.6);
- 3: $\kappa_{p\perp}$ according to equation (2.2.5);
- 4: $\kappa_{c\perp}$ according to equation (2.2.8) with $Kn=0$ and $Re=2.10^{-3}$;
- 5: $\kappa_{c\perp}$ according to equation (2.2.8) with $Kn=0$ and $Re=3.10^{-2}$;
- 6: $\kappa_{c\perp}$ according to equation (2.2.8) with $Kn=0$ and $Re=7.10^{-1}$.

The discussion given above clearly illustrates that the dynamic shape factor of a non-spherical particle depends on the orientation of the particle, the Knudsennumber (Kn), and possibly on the Reynoldsnumber (Re).

The fact that non-spherical particles in creeping motion ($Re < 0.1$) have dynamic shape factors depending on Re has heretofore only been established for long circular cylinders moving perpendicular to their axis. However, for Re larger than 0.1 this feature becomes more significant as has been discussed by Hochrainer and Hänel [41].

Concerning the orientation of a particle it must be remarked that due to Brownian rotation, the orientation of a particle will change all the time. Therefore, if there are no forces strong enough to counteract the Brownian rotation and keeping the particle in a specific orientation, the particle will be randomly oriented in time, which implies that the fluid drag on the particle can be characterised by a mean dynamic shape factor. For instance it can be shown that the dynamic shape factor of a prolate spheroid undergoing random change of orientation and moving with a constant velocity is given by [92]:

$$\overline{(\kappa_p)}_1 = \frac{1}{3} \kappa_{pH} + \frac{2}{3} \kappa_{p1} \quad (2.2.9)$$

However, in case of a spheroid settling under influence of gravity a random change of orientation will cause a random change of the velocity while the fluid drag remains constant (viz. equal to the gravity force). In that case the dynamic shape factor, $\overline{(\kappa_p)}_2$, of a prolate spheroid is given by [33]:

$$\frac{1}{\overline{(\kappa_p)}_2} = \frac{1}{3} \frac{1}{\kappa_{pH}} + \frac{2}{3} \frac{1}{\kappa_{p1}} \quad (2.2.10)$$

The feature that the dynamic shape factor of a non-spherical particle usually depends on Kn is shown below.

Analogous to the case of spherical particles one can write for the fluid drag on a non-spherical particle at arbitrary Kn:

$$F(Kn) = \frac{F(Kn=0)}{C_n(Kn)} \quad (2.2.11)$$

where $C_n(Kn)$ is the slip correction factor for the non-spherical particle.

Eq. (2.2.1) can be written as:

$$F(Kn) = - \frac{3\pi\eta\kappa(Kn)d_e v}{C_s(d_e)} \quad (2.2.12)$$

and,

$$F(Kn=0) = -3\pi\eta\kappa(0)d_e v \quad (2.2.13)$$

From equations (2.2.11) to (2.2.13) one finds:

$$\kappa(Kn) = \left\{ \frac{C_s(d_e)}{C_n(Kn)} \right\} \kappa(0) \quad (2.2.14)$$

Usually $C_s(d_e)$ will differ from $C_n(Kn)$, which implies that κ depends on Kn . Often expressions of $C_n(Kn)$ are needed. However, up to now such an expression has been derived for spheres only. The slip correction factor of a long circular cylinder moving in a direction perpendicular to its axis can be evaluated from the results of Pich (eq. 2.2.7). Therefore approximation methods are used to obtain the slip correction factor of non-spherical particles. The approximation methods employed up to now are all based on the slip correction factor obtained for spheres. They differ in the quantity substituted for the sphere diameter. Sometimes the slip correction factor of a non-spherical particle has been approximated by the Knudsen-Weber formula (eq. 2.1.4) or the Fuchs-Stechkina formula (eq. 2.1.5), with the sphere diameter simply replaced by some particle dimension [108] or the volume equivalent diameter [31,80]. These methods were used for lack of a better one, and in most cases the slip correction factor derived in this way shows a poor agreement with reality. Dahneke [15,16,17] has described a method, which gives better approximations. However, this method is only applicable when the fluid drag on the particle is known at $Kn = 0$ as well as at a distinct large value of $Kn(Kn_1)$. $C_n(Kn_1)$ can then be obtained from equation (2.2.11). Subsequently one calculates at which Knudsen number (Kn_{adj}) the slip correction factor of a sphere (adjusted sphere) equals $C_n(Kn_1)$. Hence:

$$C_n(Kn_1) = C_s(Kn_{adj}) = 1 + A Kn_{adj} + Q Kn_{adj} \exp\left[-\frac{B}{Kn_{adj}}\right] \quad (2.2.15)$$

with

$$Kn_1/Kn_{adj} = d_{adj}/2L_c = w \quad (2.2.16)$$

where L_c is the characteristic length of the non-spherical particle used in defining Kn_1 , and d_{adj} is the diameter of the "adjusted sphere". According to this method, an approximation of C_n at arbitrary Kn follows from equations (2.2.15) and (2.2.16) by dropping the index 1, viz.:

$$C_n(Kn) = 1 + A \frac{Kn}{w} + Q \frac{Kn}{w} \exp\left[-\frac{B \cdot w}{Kn}\right] \quad (2.2.17)$$

As has become clear from the discussion given in this chapter, information about the fluid drag on arbitrarily shaped particles can only be obtained from experiment. From equation (2.2.1) it can be seen that the fluid drag on a non-spherical particle can be characterised by two parameters, viz. d_e and κ . From an experimental viewpoint, however, there is need for a single measurable parameter, directly describing the behaviour of the particle. Because many aerosol problems are dealing with the settling of particles, two parameters have been introduced, which characterise the settling rate, viz. the Stokes diameter (d_s), and the aerodynamic diameter (d_a).

The Stokes diameter of a particle is defined as the diameter of a sphere having the same density and settling rate as the particle in question [26], while the aerodynamic diameter is the diameter of a sphere of unit density having the same settling rate as the particle in question [34,101].

The settling rate of a particle is entirely characterised by its aerodynamic diameter, whilst the Stokes diameter gives information about the settling rate only when the density of the particle is known. Furthermore the aerodynamic diameter has the advantage that it can be determined experimentally without knowing the density of the particle.

In aerosol physics the aerodynamic diameter has proved to be a suitable parameter for aerosol characterisation.

In order to obtain the relation between d_a , κ and d_e , the terminal settling velocity of the particle must be calculated. This terminal settling velocity follows from the equilibrium of forces, thus:

$$\frac{3\pi\eta d_e \kappa v_s}{C_s(d_e)} = \frac{\pi}{6} \cdot d_e^3 (\rho - \rho_g) g \quad (2.2.18)$$

with:

- ρ = density of the particle,
- ρ_g = density of the gas,
- g = acceleration of gravity,
- v_s = terminal settling velocity.

Thus, v_s becomes:

$$v_s = \frac{d_e^2 (\rho - \rho_g) g C_s(d_e)}{18\eta\kappa} \quad (2.2.19)$$

For a reference sphere with unit density (ρ_0), having the same settling rate as the particle, one has in the same way:

$$v_s = \frac{d_a^2 (\rho_0 - \rho_g) g C_s(d_a)}{18\eta} \quad (2.2.20)$$

Neglecting ρ_g with respect to ρ and ρ_0 , one finds from (2.2.19) and (2.2.20):

$$d_a = \kappa^{-\frac{1}{2}} (\rho/\rho_0)^{\frac{1}{2}} \{C_s(d_e)/C_s(d_a)\}^{\frac{1}{2}} d_e \quad (2.2.21)$$

By inserting the expressions for the dynamic shape factors of spheroids and circular cylinders into equation (2.2.21) expressions for the aerodynamic diameters of these particles are obtained.

Because κ occurs in equation (2.2.21), d_a may depend on the orientation of the particle, on K_n , and on Re .

3. CALIBRATION OF A STÖBER CENTRIFUGAL AEROSOL SPECTROMETER

3.1. Introduction

In many cases, the behaviour of aerosol particles can be characterised by their aerodynamic diameter. Only for some regularly shaped particles the aerodynamic diameter can be calculated from the dimensions of the particle, provided that the density of the particle is known (cf. chapter 2). In practice, however, most particles do not have such regular shapes. Therefore in aerosol research a great deal of effort has been spent in developing and evaluating experimental methods for aerodynamic diameter determination. In appendix I these methods are discussed critically, especially with respect to their applicability in the present study, the purpose of which is to determine a relation between the microstructure and the aerodynamic diameter of branched chain-like aggregates. The conclusion of this discussion is, that the spiral centrifuge designed by Stöber and Flachsbart [96] is the most suitable apparatus for this purpose.

The rotor of the spiral centrifuge is shown in figure 3.1. The duct, which is 1.8 m long and 4.3 cm deep, is formed by six hemicircles with increasing radii. The aerosol is injected in a laminar flow of clean air at the inner wall and distributed over the whole depth of the spinning duct. The aerosol enters the inlet from above, while the clean air is introduced in the duct from below through the bearing system. In order to obtain a laminar flow, the clean air passes through a system of parallel thin plates. Due to the centrifugal force, the particles move through the clean air flow towards the outer wall of the spinning duct, while simultaneously they are driven along the duct by the clean air flow. As a result, the particles are deposited on a removable collection foil, which entirely covers the outer wall of the duct. The distance (l) of the deposition location from the beginning of the foil, depends on the aerodynamic diameter (d_a) of the particles. At a rotor speed of 3200 revolutions per minute, a clean air flow of

83 cm³/s and an aerosol flow of 4.2 cm³/s, the apparatus shows a satisfactory resolution in the aerodynamic diameter range from 0.06 μm up to 2 μm.

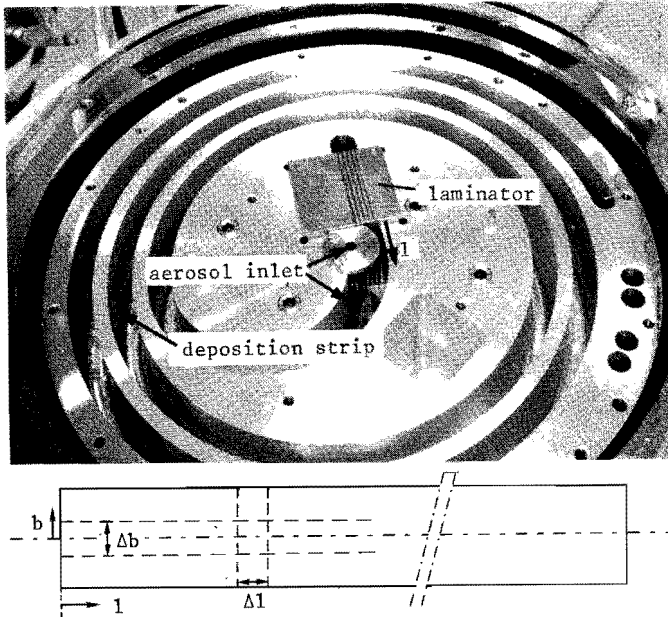


Figure 3.1. Rotor with spiral duct (above) and schematic diagram of the deposition strip.

Probably as a result of the curvature of the duct [11], and the coriolis force, caused by the velocity of the air relative to the spinning rotor [94], a double vortex is formed in the air flow (cf. figure 3.2).

Due to this double vortex flow, a theoretical calculation of the relation between l and d_a , will be very complicated. Therefore this relation has to be obtained from calibration experiments, carried out with test aerosols. Such test aerosols consist of regularly shaped particles of known density, the aerodynamic diameter of which can be calculated from their size. Therefore spherical particles are preferably used as test aerosols, although sometimes non-spherical particles such as cubes (NaCl) are employed.

Widely used test aerosols are monodisperse polystyrene spheres which can be produced by spraying emulsions of monodisperse polystyrene spheres, so called latices. These latices can be obtained from different manu-

facturers (for instance Dow and Pêchiney) in a wide range of sizes (down to $0.08 \mu\text{m}$).

Such monodisperse polystyrene spheres are deposited on the deposition strip of the centrifuge as a number of narrow bands (cf. figure 3.10) corresponding to singlets, doublets, triplets etc. These deposits show that the relation between l and d_a depends on the distance (b) from the center line of the deposition strip, which is caused by the somewhat parabolic flow pattern in the duct. Therefore the calibration curve (relation between d_a and l) is determined only for particles deposited along the center line of the collection foil.

The deposit concentration depends on b as well.

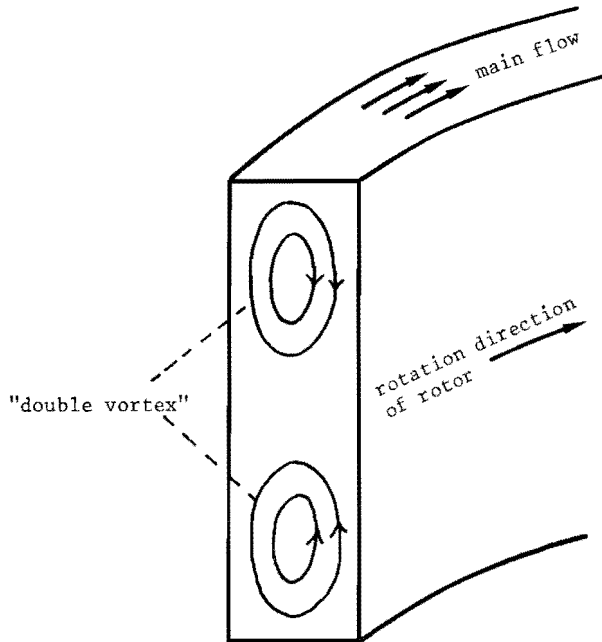


Figure 3.2. Schematic picture of the secondary "double vortex" flow in the duct of the spiral centrifuge.

In order to use the centrifuge for measurements of an aerodynamic diameter distribution, the distribution function, $\phi(d_a)$, must be determined from the deposit concentration, $\phi^*(l)$, along the center line of the collection foil. Therefore a transformation function must be determined by which

$\phi^*(l)$ can be transformed into $\phi(d_a)$. This transformation function must account for all size dependent mechanisms occurring in the centrifuge such as aerosol losses in the inlet system.

In the present study, the spiral centrifuge is not used for measurements of aerodynamic diameter distributions, but only for the separation of particles according to their aerodynamic diameter. Nevertheless, the calibration reported in this chapter includes the evaluation of a transformation function by which $\phi^*(l)$ can be transformed into $\phi(d_a)$, thus providing all the information needed for using the instrument for the determination of aerodynamic diameter distributions.

3.2. Theory

Let us consider a narrow strip width Δb along the center line of the collection foil (figure 3.1), and assume that the deposit density in this narrow strip does not vary with b . Let further $P(d_a) \Delta b$ be the probability that a particle with an aerodynamic diameter d_a is deposited on the strip width Δb , and $T(l, d_a) \Delta l$ be the probability that a particle with an aerodynamic diameter d_a , deposited on the strip width Δb , is deposited between l and $l + \Delta l$ (cf. figure 3.1).

Then:

$$\phi^*(l_1) = \int_0^{\infty} T(l_1, d_a) P(d_a) \phi^*(d_a) dd_a \quad (3.2.1)$$

where $\phi^*(l_1)$ = surface density of the deposit at the location l_1 on the centre line,

$\phi^*(d_a) dd_a$ = number of particles entering the centrifuge with an aerodynamic diameter between d_a and $d_a + dd_a$.

Let us assume that we can write:

$$T(l_1, d_a) = T\{l_1 - l(d_a)\} \quad (3.2.2)$$

which means that $T(l_1, d_a)$ is only a function of the distance between l_1 and the most probable deposition place, $l(d_a)$, as given by the calibration curve.

From (3.2.1) and (3.2.2) one obtains:

$$\phi^*(l_1) = \int_{l(d_a=0)}^{l(d_a=\infty)} T(l_1-1) P\{d_a(l)\} \phi^*\{d_a(l)\} \frac{dd_a(l)}{dl} dl \quad (3.2.3)$$

With $d_a(l)$ being the inverse calibration relation.

In equation (3.2.3) only ϕ^* is unknown, because T , P and $d_a(l)$ can be obtained from calibration experiments, while $\phi^*(l)$ can be obtained by counting the number of particles on the collection foil.

Equation (3.2.3) is an integral equation of the first kind. Approximations of $\phi^*(d_a)$ can be obtained by numerical methods. However, this will be a time consuming operation. Since, as will be shown later, the centrifuge has a very good size resolution, the error made by assuming that the resolution is ideal will be small. In that case:

$$T(l_1-1) = \delta(l_1-1) \quad (3.2.4)$$

The properties of the δ -function are:

$$\int_{-\infty}^{\infty} \delta(x) dx = 1 \quad \text{and} \quad \int_{-\infty}^{\infty} \delta(x) f(x) dx = f(0) \quad (3.2.5)$$

Equation (3.2.4) expresses the assumption that all particles with the same aerodynamic diameter are deposited at location l , as given by the calibration curve.

From (3.2.3) and (3.2.4) one finds:

$$\phi^*(l_1) = \int_{l(d_a=0)}^{l(d_a=\infty)} \delta(l_1-1) P\{d_a(l)\} \phi^*\{d_a(l)\} \frac{dd_a(l)}{dl} dl \quad (3.2.6)$$

and using (3.2.5):

$$\phi^*(l_1) = -P\{d_a(l_1)\} \left\{ \frac{dd_a(l)}{dl} \right\}_{l=l_1} \phi^*\{d_a(l_1)\} \quad (3.2.7)$$

$P(d_a)$ describes the aerosol losses as well as the ratio of the number of particles deposited on the strip width Δb to the number of particles deposited beside that strip. The minus sign in (3.2.7) results from (3.2.6), because $l(d_a=0)$ is larger than $l(d_a=\infty)$.

Equation (3.2.7) can be written as:

$$\phi^*(d_a) = b_r f_c(d_a) \cdot \phi^*\{l(d_a)\} \quad (3.2.8)$$

with:

$$f_c(d_a) = - \frac{dl(d_a)}{dd_a} \cdot \frac{1}{b_r \cdot P(d_a)} \quad (3.2.9)$$

$\phi^*(l)$ is the measured deposit concentration along the center line of the collection foil, and $f_c(d_a)$ can be obtained from calibration experiments as will be shown subsequently. The exact value of $P(d_a)$ is hard to determine. For this reason an arbitrary reference length b_r appears in equation (3.2.8). The normalized aerodynamic diameter distribution, $\phi(d_a)$, of the sampled aerosol can be determined from $\phi^*(d_a)$.

3.3. Materials and methods

To adjust the clean air flow and the aerosol flow, a flow system as shown diagrammatically in figure 3.3 was developed. The air is circulated in a closed circuit, comprising the spiral centrifuge, by a pump, the capacity of which is adjustable. Part of the air is withdrawn from the

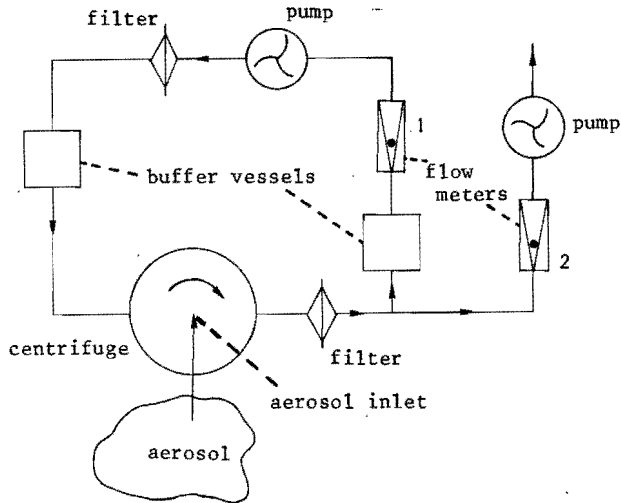


Figure 3.3. Flow system.

system by another adjustable pump. Therefore, the air withdrawn from the system will be replaced by aerosol entering the system through the aerosol inlet of the centrifuge. Two flowmeters are placed in the flow-system to measure the clean air flow (flowmeter 1) and the aerosol flow (flowmeter 2). Filters are placed in the flowcircuit, to remove particles which have escaped deposition in the centrifuge. To level out flow fluctuations, two buffervessels are placed in the circuit.

Evidently the flowsystem described above can only be used when it contains no significant leakages. However, the original designs of the Stöber centrifuge have the fault that the bearing system, through which the clean air enters the centrifuge, becomes leaky. Therefore a non-leaking bearing system according to Oeseburg and Roos [71] has been applied in the apparatus used in this study.

The calibration experiments were carried out with both monodisperse and polydisperse polystyrene spheres. The monodisperse aerosols were produced by spraying monodisperse latices from Dow and Pēchiney. The polydisperse polystyrene aerosols were generated by nebulizing a solution of polystyrene in xylene. The xylene vapour concentration in the final aerosol must be very small, otherwise the centrifuge does not separate the aerosol particles according to their aerodynamic diameters, and all particles are deposited on the lower half of the collection foil. This is probably caused by viscous forces and the difference in density between the aerosol flow and the clean air flow.

A proper polydisperse test aerosol (figure 3.4) was obtained by adding a large amount of clean air to the aerosol (figure 3.5).

For the calibration experiments with the polydisperse polystyrene aerosol, about 20 electron microscope grids were placed along the center line of the collection foil. These electron microscope grids were coated and held in place by a formvar film. The diameters of the deposited particles were obtained from electron microscope (Philips EM 200) pictures. A carbon replica of a diffraction grating with 2160 lines per millimeter was used as a length standard for the determination of the electron microscope magnification.

Because of the large deviations between the manufacturers data and the data obtained by some investigators [36,76,84,97], the diameters of the monodisperse polystyrene spheres were measured from electron microscope

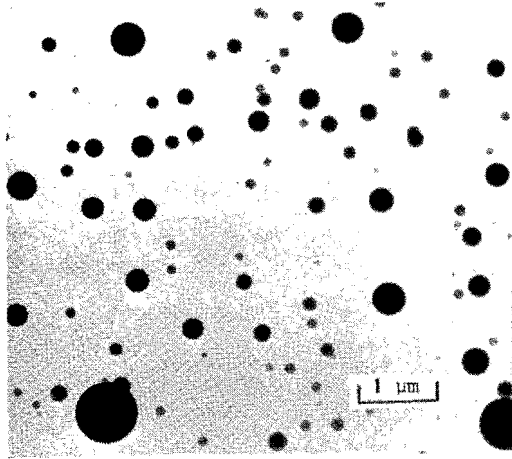


Figure 3.4. Polydisperse polystyrene test aerosol.

photographs as well. The aerodynamic diameters of the polystyrene spheres were calculated from:

$$\rho_0 d_a^2 C_s(d_a) = \rho d^2 C_s(d) \quad (3.3.1)$$

with: $\rho_0 = 1 \text{ g.cm}^{-3}$
 $\rho = \text{density of polystyrene} = 1.05 \text{ g.cm}^{-3}$
 $d = \text{diameter of the sphere}$
 $C_s = \text{slip correction factor (cf. chapter 2).}$

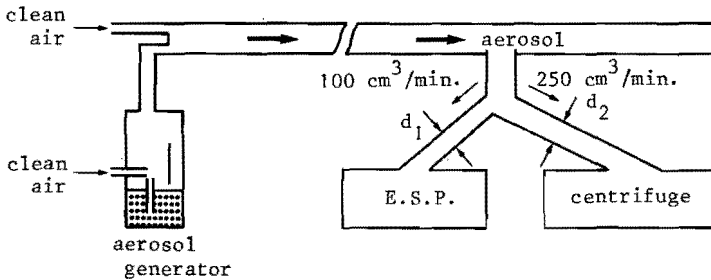


Figure 3.5. Aerosol generation and sampling system; $d_1/d_2 = (100/250)^{1/2}$.

Apart from the calibration curve, the transformation function, $f_c(d_a)$, and the resolving power could also be obtained from the experiments with the polydisperse aerosol. The size distribution of the particles deposited on the same electron microscope grid, was used for the determination of the resolving power. These distributions were measured from electron microscope pictures, using a semi-automatic particle size analyser. The transformation function, $f_c(d_a)$, was obtained by comparing $\phi^*(1)$ with the aerodynamic diameter distribution as determined separately from electron microscope pictures of a sample taken with a point to plane electrostatic precipitator (E.S.P.) according to Morrow and Mercer [68]. With an E.S.P., aerosol particles are sampled directly on an electron microscope grid in a non-size-selective way. In appendix II the E.S.P. is described in detail.

Several precautions were taken to make sure that the centrifuge as well as the E.S.P. sampled an aerosol with identical size distributions. Both instruments sampled simultaneously at the same location of an aerosol flow, and with identical sampling rates. (The diameters of the sampling tubes are chosen such that they are adjusted to the different sampling flows; E.S.P. $1.7 \text{ cm}^3/\text{s}$ and the centrifuge $4.2 \text{ cm}^3/\text{s}$). In figure 3.5 a schematic drawing is given of the aerosol generation and sampling system.

Because of the non-size-selective sampling of the E.S.P., the aerodynamic diameter distribution obtained from the E.S.P. sample represents the aerodynamic diameter distribution, $\phi^*(d_a)$, of the aerosol sampled with both the E.S.P. and the spiral centrifuge. Using equation (3.2.8), the transformation function, $f_c(d_a)$, can be obtained from $\phi^*(d_a)$ (obtained from the E.S.P. sample) and $\phi^*(1)$ (obtained by counting the particle numbers along the center line of the deposition strip of the centrifuge).

Also attention was paid to the influence of the cooling system of the centrifuge. It was shown that variations in the cooling system influenced the deposition pattern of monodisperse aerosols. This phenomena was studied with respect to its influence on the deposition pattern, the calibration curve, the transformation function, and the resolving power of the spiral centrifuge.

3.4. Results

3.4.1. Calibration experiments

Figure 3.6 shows the calibration curve as obtained at the operating conditions: rotor speed = 3200 revolutions per minute; clean air flow = $83 \text{ cm}^3/\text{s}$, and aerosol flow = $4.2 \text{ cm}^3/\text{s}$. The scatter in the data can be explained by the inaccuracy of the electron microscope magnification measurements. The calibration curve can be represented by:

$$\log\left(\frac{d_a}{d_{a,r}}\right) = 5.563 - 9.539 \log\left(\frac{l}{l_r}\right) + 5.497 \left\{ \log\left(\frac{l}{l_r}\right) \right\}^2 - 1.171 \left\{ \log\left(\frac{l}{l_r}\right) \right\}^3 \quad (3.4.1.)$$

where, $d_{a,r} = 1 \text{ }\mu\text{m}$, and $l_r = 1 \text{ cm}$.

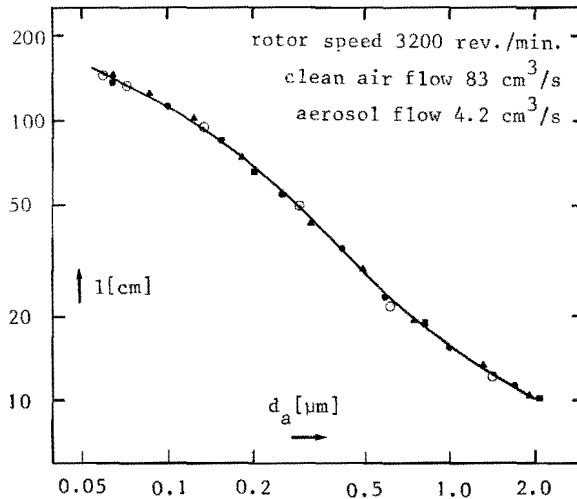


Figure 3.6. Calibration curve determined with monodisperse (o) and polydisperse (●▲) aerosols.

The transformation function, $f_c(d_a)$, as obtained from the calibration data, is shown in figure 3.7. The arbitrary reference length, b_r , was chosen such that $b_r P(d_a) = 1$ for $d_a = 0.3 \text{ }\mu\text{m}$. The transformation function

was derived from three experiments. The data resulting from these experiments have a relative standard deviation of about 15%. In each experiment about 10^4 particles were counted and sized to obtain $\phi^*(d_a)$ and $\phi^*(1)$. The empirical transformation function, as obtained in this study, differs schematically from the absolute value of the derivative of the calibration curve (cf. fig. 3.7), which is at variance with the results obtained by Stöber et al. [99].

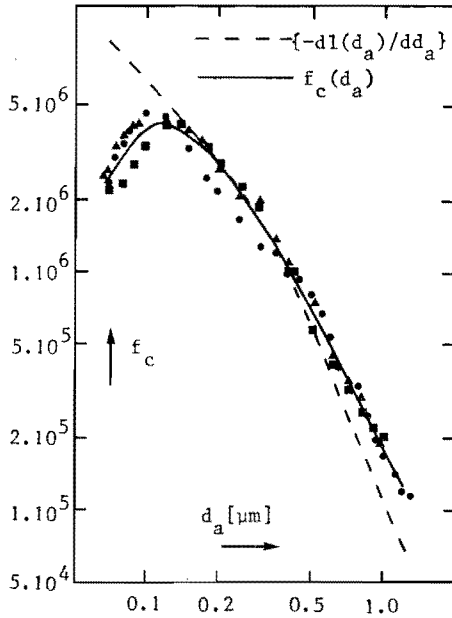


Figure 3.7. $f_c(d_a)$ curve, and the $-d \ln(d_a)/dd_a$ curve.

The empirical transformation function can be represented by:

$$\begin{aligned} \log f_c = & 5.28 - 1.63 \log\left(\frac{d_a}{d_{a,r}}\right) + 1.11 \left\{ \log\left(\frac{d_a}{d_{a,r}}\right) \right\}^2 + \\ & + 1.43 \left\{ \log\left(\frac{d_a}{d_{a,r}}\right) \right\}^3 \end{aligned} \quad (3.4.2)$$

where $d_{a,r} = 1 \mu\text{m}$.

The standard deviation of the aerodynamic diameter distribution of the particles deposited at the same location l (in this case on the same electron microscope grid) is, although slightly dependent on $\phi(d_a)$, a good measure for the resolving power of the spiral centrifuge. The ratio of this standard deviation, $\sigma(d_a)$, and d_a related to d_a is shown in figure 3.8.

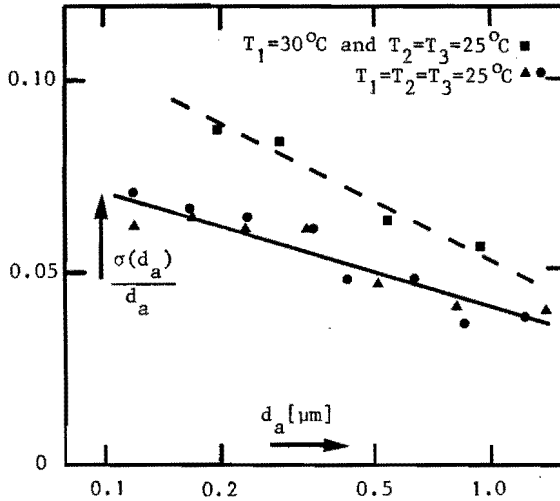


Figure 3.8. $\sigma(d_a)/d_a$ versus d_a at different cooling conditions.
 σ has been determined from: $\sigma^2(\bar{x}) = \frac{\sum_i \Delta N_i (\bar{x} - x_i)^2}{\sum_i \Delta N_i}$.

3.4.2. The influence of the cooling system

The cooling system of the spiral centrifuge as used, is shown schematically in figure 3.9. The bearings, the rotor housing, and the upper plate can be kept at independent constant temperatures T_3 , T_2 and T_1 . Variation of these temperatures causes a variation of the deposition pattern of mono-disperse aerosols. As is shown in figure 3.10, the aerosol particles tend to deposit towards the cold side of the rotor. A simultaneous and equal increase or decrease of all three temperatures did not change the deposition pattern.

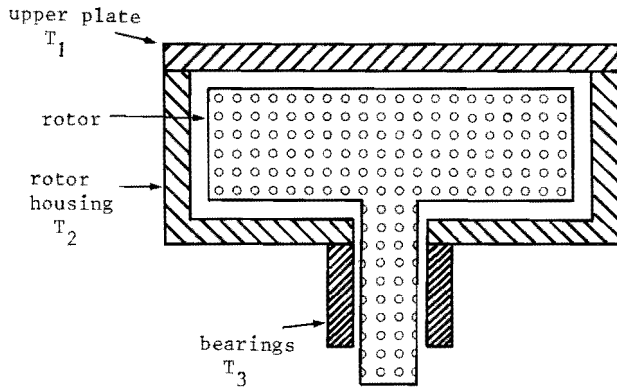


Figure 3.9. Diagram of the cooling system of the centrifuge. The upper plate, rotor housing, and the bearings can be kept independently at the temperatures T_1 , T_2 , and T_3 .

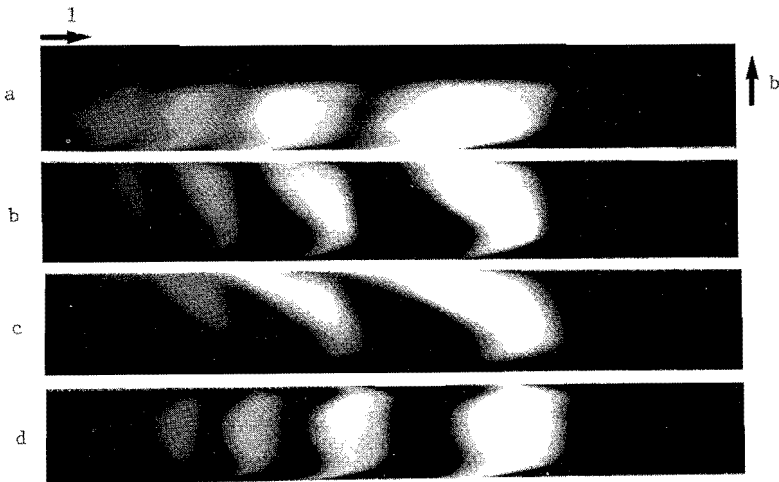


Figure 3.10. Deposit pattern of a monodisperse aerosol ($d = 0.357 \mu\text{m}$) at different cooling conditions.

- a: $T_1 = 35^\circ\text{C}$, $T_2 = 25^\circ\text{C}$, $T_3 = 15^\circ\text{C}$;
- b: $T_1 = 15^\circ\text{C}$, $T_2 = T_3 = 25^\circ\text{C}$;
- c: $T_1 = 15^\circ\text{C}$, $T_2 = 25^\circ\text{C}$, $T_3 = 35^\circ\text{C}$;
- d: $T_1 = T_2 = T_3 = 25^\circ\text{C}$.

In order to investigate the influences of the temperature variations on the calibration curve, the transformation function, and the resolving power of the centrifuge, the calibration was repeated at cooling conditions ($T_1 = 30^{\circ}\text{C}$, $T_2 = T_3 = 25^{\circ}\text{C}$) different from those at which the calibration experiments reported in the previous section were carried out ($T_1 = T_2 = T_3 = 25^{\circ}\text{C}$). The results of this calibration showed a calibration curve as well as a transformation function being identical to those as reported in section 3.4.1. However, the resolving power deteriorated, as is shown in figure 3.8.

3.5. Discussion

In many studies [8,38,70,99] in which the spiral centrifuge has been used for measuring aerodynamic diameter distributions, it has been assumed that the transformation function is identical with the absolute value of the derivative of the calibration curve. Such an assumption implies a constant value of the function $P(d_a)$, which function represents

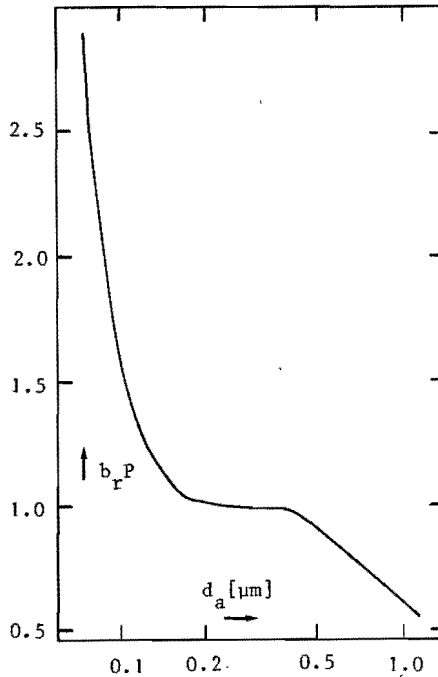


Figure 3.11. $b_r P(d_a)$ in relation to d_a .

size selective mechanisms in the centrifuge as for instance aerosol losses in the inlet (cf. section 3.2). The absence of such size selective processes is rather unlikely. Therefore, it is not surprising that $P(d_a)$, as resulting from this calibration study, is far from constant, as is shown graphically in figure 3.11. The $P(d_a)$ curve clearly can be divided into three parts, viz.:

- (I) $d_a < 0.2 \mu\text{m}$: steeply increasing $P(d_a)$ with decreasing d_a ;
- (II) $0.2 \mu\text{m} < d_a < 0.4 \mu\text{m}$: nearly constant $P(d_a)$;
- (III) $d_a > 0.4 \mu\text{m}$: increasing $P(d_a)$ with decreasing d_a .

Part (I) of the $P(d_a)$ curve can be explained by the influence of the secondary "double vortex" flow in the spiral duct. With increasing l , this "double vortex" tends to cumulate the particle deposit towards the center line of the collection foil, as already was suggested by Stöber et al. [99].

Part (III) can be explained by the aerosol losses in the inlet, which loss of course increases with increasing d_a .

Obviously part (II) is a transition region between parts I and III where there is little nett influence of all size selective processes, resulting in an almost constant $P(d_a)$.

In the theoretical consideration given in section 3.2, it is assumed that the size resolution of the centrifuge is ideal. The error introduced by this assumption in the evaluation of aerodynamic diameter distributions from $\phi^*(l)$ by means of equation (3.2.9), will be small, if the standard deviation of the aerodynamic diameter distribution, $\phi^*(d_a)$, is larger than $\sigma(d_a)$ (cf. figure 3.8), being the standard deviation of the particles sampled at the same location l . For measuring distributions with smaller standard deviations the function $T(l, d_a)$ (cf. section 3.2) must be known with sufficient accuracy. In principle, $T(l, d_a)$ can be derived from the experiments described in this chapter, but this demands a sufficiently accurate measurement of the size distributions of the particles deposited at the same location l . This accuracy, however, was limited by the accuracy of the particle size analyser used.

In practice, however, aerosols generally will have aerodynamic diameter distributions with standard deviations significantly larger than $\sigma(d_a)$.

Number as well as mass aerodynamic diameter distributions can be

evaluated in the way described above. Concerning the measurements of mass distributions, however, it would be worthwhile to use a larger part of the foilwidth than in this study. This would enlarge the amount of mass to be determined, which is desirable because of the relatively large amount of mass needed for most mass measuring methods. Such an increase of the effectively used stripwidth along the center line of the collection foil will probably demand a transformation function different from the one obtained in the present study.

An attempt has been made by Ferron and Bierhuizen [24] to determine an aerodynamic diameter mass distribution from the mass deposited over the whole width of the collection foil. They determined the deposited mass distribution over the collection foil width with respect to 1, together with the amount of mass deposited in the inlet and the amount of mass having escaped deposition in the centrifuge (this mass was captured by a final filter). In their experiments a polydisperse NaCl aerosol, labeled with ^{24}Na , has been used as a test aerosol. Unfortunately, their results are not given in terms of a transformation function, as is done in this study. Their study is incomplete because of the absence of particle size measurements, and a reference spectrometer. Nevertheless their results give valuable information about the deposition mechanism in the centrifuge.

Concerning the influence of the cooling system on the particle deposition, the responsible mechanism is still unknown. The direction of the variation (the particles tend to deposit towards the cold side of the rotor) would suggest thermophoretic effects. Unfortunately, the theory on thermophoresis has not been developed for the Knudsen-region of the observed particles. However, from the results of experimental studies [109,113] it can be concluded that the temperature gradients as applied in this study should cause a displacement of the observed $0.357\ \mu\text{m}$ spheres (cf. figure 3.9) due to thermophoresis, being less than $0.1\ \text{mm}$. Therefore, the deposit variations as observed cannot be ascribed to thermophoresis.

Apart from thermophoresis, the different temperatures of the upper plate and the bearing system might cause a difference in the temperatures of the aerosol and the clean air, because the former enters through the upper plate while the latter enters through the bearing system. This should cause a transport of the aerosol in a vertical direction when mixed with the clean air, because of the different densities. The result of this mechanism on the particle deposits, however, should be opposite

to what is observed, unless the particles are concentrated already in the inlet system in a thin layer entering the duct at the boundary of the aerosol flow and the clean air flow and therefore, due to viscous forces, are taken along with the clean air flow in the vertical direction opposite to the main part of the aerosol flow.

However, whatever the responsible mechanism might be, it appeared from the experiments with the polydisperse aerosol that the effect is equal for all diameters, which suggests that the mechanism is only active in the inlet system or at least in the very first part of the spiral duct.

Finally it must be remarked that all data reported in this chapter are specific for the centrifuge used, under the chosen working conditions.

4. THE AERODYNAMIC DIAMETER OF BRANCHED CHAIN - LIKE AGGREGATES

4.1. Introduction

The settling of aerosol particles is an important feature in aerosol physics. Therefore many studies have dealt with particle settling or in more general terms with the fluid drag on particles. Unfortunately the results of these studies have not been presented in a uniform terminology, which complicates comparison. Several quantities have been introduced for particle characterisation such as the Stokes diameter, the dynamic shape factor (cf. section 2.2) and several other shape factors. Since the introduction of the aerodynamic diameter (cf. section 2.2) for particle characterisation by Hatch and Gross [34] the use of this quantity has progressively increased. This was stimulated by its use by the Task Group on Lung Dynamics [10]. The advantage of characterisation of particles by their aerodynamic diameter is, as already remarked in section 2.2, that it provides the possibility of a direct comparison of the settling rates of particles composed of different materials without the necessity to know such parameters as density and particle volume. Therefore in this study the aerodynamic diameter is used for particle characterisation.

Originally, for lack of accurate aerosol classifiers, fundamental studies of the fluid drag on non-spherical particles had to be limited to particles which could be observed by the bare eye or by simple optical instruments. Therefore, instead of aerosol particles, large model particles of various shapes (discs, aggregates of spheres, spheroids, cylinders, etc.) were employed. The particles were allowed to settle in viscous liquids and their settling rates at different orientations were determined. The results of such studies, as carried out for instance by Kunkel [53], McNown and Malaika [61], Heiss and Coull [37], and recently by Horvath [42], provide very valuable information about the fluid drag on non-spherical particles. By the progress in the development of aerosol classifiers, the possibility of fundamental studies of the fluid drag on aerosol particles increased rapidly. However, experimentation with aerosol particles is limited, due to the absence of a wide variety of aerosol particles with well defined shapes. In addition the orientation of airborne particles during settling,

will mostly be uncontrolled and even unknown.

Nevertheless studies of the fluid drag on well defined test aerosols such as NaCl particles (cubes) and aggregates of monodisperse polystyrene spheres will give very helpful additional information, for instance about the slipcorrection factor to be applied for non-spherical particles. Recently such a study has been carried out by Stöber and coworkers [92,99] with respect to the fluid drag on aggregates of polystyrene spheres. Their results agree fairly well with the results Horvath [42] obtained for aggregates of model spheres.

Although the studies mentioned above concern particle shapes which can hardly be compared with the usually very irregularly shaped atmospheric particles, the results of these studies can be very helpful in the microscopic characterisation of atmospheric particles. For instance, Stöber [99] showed that there is a significant agreement between the aerodynamic characteristics of linear chains of monodisperse polystyrene spheres and those of asbestos fibres.

The present study deals with aggregates consisting of a large number of submicron particles. Such aggregates are produced by industry and automobiles and are therefore widely spread in the atmosphere. Branched chain-like aggregates of several materials already were subject of an extensive study reported in 1932 by Whytlaw-Gray and Patterson [112]. The aggregates were observed in a Millikan chamber during settling under the influence of gravity as well as with an electric field applied. From these experiments the settling rates of the aggregates under the influence of gravity as well as their mass was obtained. The aggregates were characterised by an apparent diameter and density corresponding to a sphere having equal mass and settling rate as the aggregate in question. Apparent densities as low as one tenth of the density of the particle material were obtained. More recently a study of the fluid drag on branched chain-like aggregates composed of up to 500 primary particles, has been reported by Vomela and Whitby [108]. Their experiments were carried out with the aerosol classifying system according to Whitby and Clark which is discussed in appendix I.2.1. Their results, which certainly will have been influenced by the difficulties arising in the classification of non-spherical particles with the system used (cf. appendix I.2.1), show the branched chain-like aggregates to have Stokes diameters very close to and even larger than their volume equivalent diameter. The difference between the

Stokes diameter and the volume equivalent diameter found by these authors was ascribed to experimental errors. They state that these very unlikely results can be explained by the influence of the increased surface area of the aggregate with respect to the volume equivalent sphere, on the fluid drag, being completely leveled out by the increased influence of the velocity slip. This explanation is not very convincing. In reality their surprising data result from an erroneous calculation of the Stokes diameter, which error was also made by other authors, as pointed out by Stöber [94].

In the present study the fluid drag on branched chain-like aggregates composed of up to 10^5 primary particles is determined using a spiral centrifuge, as reported below.

4.2. Materials and methods

4.2.1. Aerosol generation

Throughout the experiments exploding wire aerosols were used except in one case where a fluorescein aerosol was studied. The fluorescein aerosol was generated by spraying an aqueous solution of 0.1 N ammonia and fluorescein, which method has been described by Stöber and Flachsbart [97]. Before the introduction of the sprayed droplets into an aerosol vessel, they were dried by means of silica gel, so that spherical fluorescein particles remained. In the aerosol vessel the particles were allowed to coagulate in order to form aggregates. The size distribution of the primary particles depends on the nebulizing conditions and on the fluorescein concentration of the sprayed solution. Stöber and Flachsbart evaluated the density of the fluorescein particles from their aerodynamic diameters obtained by means of a spiral centrifuge (the density is found from equation 3.3.1), as well as by means of a conventional method (from volume and mass of a sample). The density resulting from the aerodynamic diameters was 1.58 g/cm^3 , whereas by means of the conventional method a density of 1.35 g/cm^3 was obtained. According to Stöber and Flachsbart this discrepancy possibly was caused by a systematic error in the calibration of their spiral centrifuge. In the present study the density of the fluorescein particles was calculated from their aerodynamic diameters measured with a spiral centrifuge, which resulted in a density of $(1.42 \pm 0.03) \text{ g/cm}^3$. This value is employed in this study.

As already mentioned, exploding wire aerosols were the main subject of study. The basic principle of the exploding wire method is, that a high energy capacitor is discharged very rapidly through a metallic wire, as is shown schematically in figure 4.1. Due to the large amount of energy dissipated in the wire, it evaporates. A few microseconds later condensation starts, and small particles are formed.

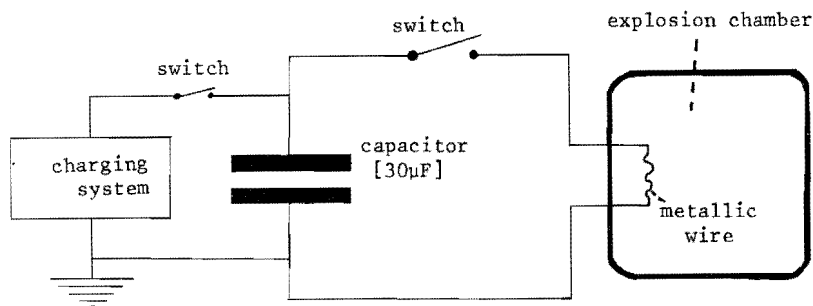


Figure 4.1. Exploding wire generation principle.

In the past the exploding wire phenomenon has been studied extensively. However, most of these studies were focussed on phenomena related to the explosion itself. Much less attention has been paid to the product of the exploding wire, the aerosol. However, from studies dealing with exploding wire particles, reported up to now [3,46,74,106] it can be concluded that the primary particles produced by an exploding wire are nearly always smooth and spherical. The primary particle size distribution depends reproducibly on the specific explosion energy (energy input per unit mass). On the whole the primary particles become coarser with decreasing specific explosion energy. However, some deviation from this behaviour is observed in this study with respect to gold wires (cf. table 4.1).

The specific explosion energy cannot simply be calculated from the amount of energy stored in the capacitor before the explosion, because not all this energy is dissipated in the wire (there are energy losses in the electrical circuit, a shock wave results which consumes energy etc.). Experimental determination of the specific explosion energy, as for instance carried out by van de Vate [106] by means of a calorimetric method, was considered to be outside the scope of this study. Therefore the explosions will not be characterised in terms of specific explosion energies,

but simply by the dimensions and the material of the wire and the tension on the capacitor (30 μ F) before the explosion. All wires exploded were about 4 cm long. The tension on the capacitor was chosen to be 10 kV or 15 kV. Explosions were carried out using wires of the following elements: iron (5 different diameters), gold (4 different diameters), and copper (1 diameter). The chemical nature of the resulting aerosols was determined by means of X-ray diffraction. The results are given in table 4.1. The results are in agreement with those of Barkow and coworkers [3] as far as gold and copper wires are concerned. However, from their experiments with iron wires they concluded that an explosion of an iron wire yields a Fe_3O_4 aerosol. The eventual results of the aerodynamic characterisation of the aggregates are only slightly influenced by the fact whether the aerosol material is Fe_2O_3 or Fe_3O_4 . Therefore no further attention is paid to this point.

The density of the primary particles was assumed to be the customary tabulated density of the aerosol material.

4.2.2. Measurement of the primary particle size distribution

The primary particle size distributions were determined by means of electron microscopy. In order to obtain samples for electron microscopic observation, the particles were deposited on formvar or carbon coated electron microscope grids by means of the spiral centrifuge as well as a point to plane electrostatic precipitator (cf. appendix II). The electron microscope pictures were analysed with a semi-automatic particle size analyser.

Because the long term accuracy of the calibration of electron microscope magnifications is limited to about 5%, and the manufacturers data usually are not reliable to better than about 10%, length standards have to be used for the evaluation of the magnification. External and internal length standards can be distinguished. In contrast to an internal length standard an external length standard cannot be observed in the electron microscope simultaneously with the object under study. Therefore the use of an external length standard requires a replacement of the object under study in the electron microscope by the length standard. This might cause variations in the electron microscope magnification due to variations in the specimen to objective distance. Furthermore there might be some difference in the photographic magnifications of the electron microscope pictures of

the length standard and the object under study.

Widely used as an internal as well as an external length standard are replicas of diffraction gratings, available with up to 2160 lines/mm. However, electron microscope magnification measurements by means of these replicas are inaccurate at the magnifications needed in this study (up to about 50000 times) because then the number of lines in the picture is very limited. Therefore in the present study negatively stained catalase crystals were used as an internal length standard. These have lattice spacings

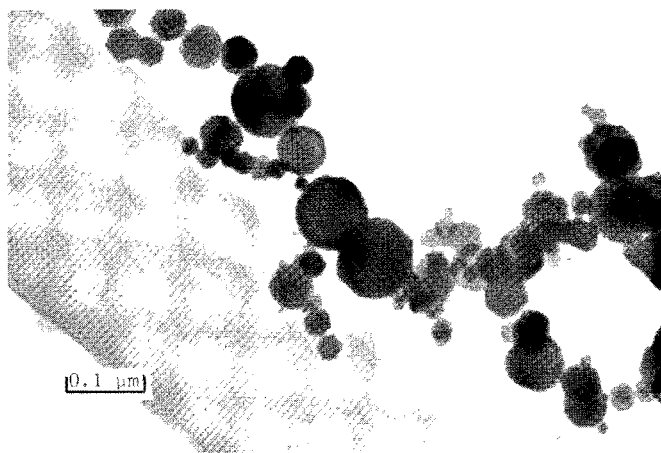


Figure 4.2. Electron microscope picture of a negatively stained catalase crystal and an iron oxide aggregate.

which are easily visible under the electron microscope, as is shown in figure 4.2. The distance between the lines is half the lattice spacing. This lattice spacing has been studied by several investigators. These studies have been summarised by Wrigley [114]. Apart from some extremes the results show half the lattice spacing of the catalase crystals to lie between 8.45 nm and 8.9 nm, which made Wrigley conclude that this spacing is 8.6 ± 0.2 nm. However, in the present study a value of 8.2 nm was obtained by means of electron microscopy using pieces of a carbon replica of a diffraction grating (obtained as a suspension from Fullham, Inc.) as an additional internal length standard. Nevertheless in this study the value of 8.6 ± 0.2 nm as quoted by Wrigley was used, because it is based on experiments being quantitatively as well as qualitatively superior to those from which our value was obtained. In spite of the fact that some uncertainty exists about the value of the lattice spacing of

the catalase crystals, they allow determinations of electron microscope magnifications in the range from 10000 to 150000 with an accuracy of better than 5%.

In order to obtain negatively stained catalase crystals for electron microscopic observation, a drop of a suspension of crystals is deposited on a formvar or carbon coated electron microscope grid. This drop is allowed to dry almost completely. Then, just before the grid becomes dry, a drop of negative stain material is added, which is drained off as completely as possible after about one minute. The negative stain penetrates in the cavities between the protein molecules of the catalase. This results in the contrast as shown in figure 4.2, when the crystals are observed in an electron microscope. The protein shows up in the figure as the white lines. In this study phosphotungstic acid adjusted to pH = 6 by means of KOH or NaOH was employed as negative stain material. Another possibility is to use 4% sodium silicotungstate as was done by Wrigley.

The suspensions of catalase crystals were obtained from Boehringer as well as from Ladd. In contrast to the suspension available from Boehringer, the crystals in the Ladd suspension are fixed with glutaraldehyde. As described by Wrigley [114] this fixation prevents the crystals from dissolving when they are mixed with the material under study. In the present study, however, no damage was observed when unfixed crystals were brought into contact with the aerosol particles studied, and therefore the Boehringer suspension *) was used in most experiments. No information is available on possible damage of catalase crystals when contacted with the material of which aerosol particles consist, because up to now negatively stained catalase crystals have to our knowledge not been used in aerosol research.

We observed that fixed as well as unfixed negatively stained catalase crystals were seriously damaged in a point to plane electrostatic precipitator. This could be avoided by evaporating a layer of carbon onto the crystals.

*) In the catalase obtained from Boehringer the crystals were dissolved, because the pH was increased above 6. Recrystallisation was obtained easily after reduction of the pH of the solution by the addition of 0.1 M acetic acid.

4.2.3. Experimental procedure

The aerosols were produced in an aerosol tank as described in section 4.2.1. The exploding wire aerosols studied, were radioactively labeled (iron oxide with ^{59}Fe , gold with ^{198}Au , and copper oxide with ^{64}Cu), by irradiation of the wires with neutrons. In order to obtain aggregates, the aerosols were allowed to coagulate during a certain time (a quarter of an hour up to 29 hours, depending on the desired aggregate sizes). After that time the aerosol was sampled with the spiral centrifuge. The relation between the mean mass of the aggregates and their aerodynamic diameter was obtained from measurements of the mass distribution and the particle number distribution along the strip. The particle number along the strip was obtained by counting from optical microscope pictures for large aggregates and from electron microscope pictures for small aggregates. In the experiments with the radioactively labeled "exploding wire" aerosols, the mass distribution along the deposition strip was obtained from radioactivity measurements with a scintillation counter. In the experiments with the fluorescein aerosol, this mass distribution was obtained by means of fluorimetry. Figure 4.3 summarizes the various steps of the method described above.

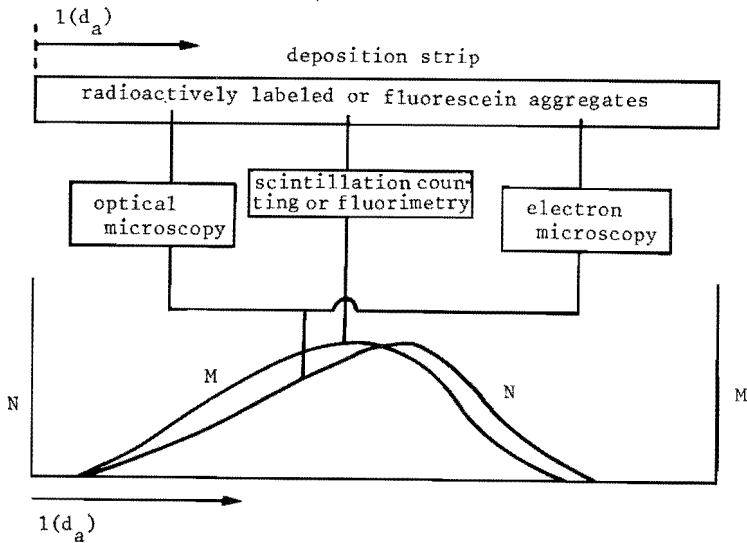


Figure 4.3. Schematic representation of the measuring procedure.

$l(d_a)$ = calibration curve of the centrifuge;

M = mass concentration; N = aggregate number concentration.

Unfortunately, the mass and particle number distribution along the strip could not be obtained from the same centrifuge sample, because these measurements put somewhat contradictory demands on the deposit as will be shown below.

The mass measurements demand a sufficiently high amount of mass to be deposited on the strip. In order to obtain the mass distribution, slices of adhesive tape (area about 2 cm^2) were placed along the center line of the collection strip. In the case of fluorescein aerosols, the mass deposited on these slices was dissolved in 25 ml 0.1 N NH_4OH . The amount of mass in this solution was evaluated by means of fluorimetry. To obtain an acceptable degree of accuracy, more than about 10 ng in the 25 cm^3 solution was needed. Therefore more than 10 ng fluorescein aerosol had to be deposited on the tape slices. In the case of the radioactively labeled "exploding wire" aerosols, the radioactivity on the tape slices was measured with a scintillation counter. From these measurements, the corresponding amount of mass was determined using a standard of known mass and specific radioactivity identical to the metallic part of the aerosol particles. The radioactivity measurements did demand an activity of at least 40 s^{-1} . The corresponding amount of mass depends on the specific radioactivity of the aerosol material. The specific radioactivity, however, is limited because of practical reasons (irradiation time), and irradiation protection considerations. It was found, that an activity of about 40 s^{-1} corresponded with an amount of aerosol material of the order of at least 0.1 μg .

The particle number distribution measurements demanded a number concentration of the deposit on the strip so small that the aggregates did not overlap. Otherwise they could not be distinguished. Some insight in the deposit concentration to be allowed, was obtained by comparing particle number measurements obtained from deposits with concentrations of known difference.

Except for very small aggregates, the demands to be put on the aerosol deposit on the centrifuge strip for the mass and particle number measurements could not be fulfilled at the same time. Therefore the following experimental procedure was chosen: A long time (24 up to 29 hours) after the the aerosol generation, when the aerodynamic diameter distribution remained virtually constant, the aerosol was sampled during a short time (about 1 minute). From this sample the number distribution along the strip was evaluated. Subsequently, during a longer time (1 hour) the

aerosol was sampled to obtain the mass distribution along the strip. Then the aerosol was sampled again during a short time for a second measurement of the particle number distribution. From these mass and particle number distributions, the relation between the aerodynamic diameter and the mass (m) of the aggregates was calculated. The number distribution was measured twice to correct for variations of the concentration and the aerodynamic diameter distribution of the aerosol.

From the relation between d_a and m , the relation between d_a and n (= number of primary particles of the aggregates) was calculated using the density of the aerosol material, and the primary particle size distribution.

4.3. Results

4.3.1. Primary particle size distribution

By the method used (cf. section 4.2.2), the particle sizes are not measured continuously, but they are divided into size classes. A typical histogram as obtained in this way is shown in figure 4.4. The distribution appears to be asymmetric, with a longer tail at large diameters. The phenomenon of asymmetric size distributions was already recognised in the last century by Galton [28] and McAllister [60]. Galton argued that size distributions have to be asymmetric by nature, because symmetric distributions do not allow sizes larger than twice the mean size.

For further treatment mathematical expressions describing the size distributions are needed. It has been shown [51,81], that asymmetric particle size distributions often can be described by a log-normal distribution, to which already was alluded by Galton and McAllister. The log-normal distribution is given by:

$$\left. \begin{aligned} f(x) &= \frac{1}{x \sqrt{2\pi} \ln \sigma_g} \exp \left[-\frac{(\ln x - \ln x_g)^2}{2 \ln^2 \sigma_g} \right] & \text{for } x > 0 \\ f(x) &= 0 & \text{for } x \leq 0 \end{aligned} \right\} \quad (4.3.1)$$

where, $f(x)$ = probability distribution function,

x = log-normal distributed quantity,

x_g = geometric mean: $\ln x_g = \overline{\ln x}$,

σ_g = geometric standard deviation: $\ln^2 \sigma_g = \overline{(\ln x - \ln x_g)^2}$.

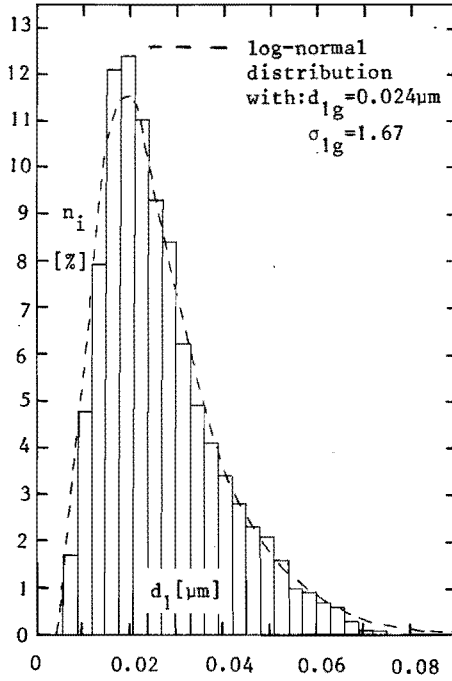


Figure 4.4. Typical histogram obtained from primary particle size distribution measurements. d_1 = primary particle diameter, n_i = number of primary particles in size class i .

From (4.3.1) one finds:

$$\overline{(x^r)}^{1/r} = \left[\int_{-\infty}^{\infty} x^r f(x) dx \right]^{1/r} = x_g \exp\left[\frac{1}{2} r \ln^2 \sigma_g\right] \quad (4.3.2)$$

where $r = 1, 2, 3$ etc.

The cumulative distribution function, $F(x)$, can be derived from equation (4.3.1), viz.:

$$\left. \begin{aligned} F(x) &= \int_{-\infty}^x f(y) dy = \frac{1}{2} + \frac{1}{2} \operatorname{erf}\left\{ \frac{\ln x - \ln x_g}{\ln \sigma_g} \right\} && \text{for } x > 0 \\ F(x) &= 0 && \text{for } x \leq 0 \end{aligned} \right\} \quad (4.3.3)$$

When plotting the cumulative log-normal distribution on so-called log-normal probability paper (x on a logarithmic scale, and $F-\frac{1}{2}$ on an inverse error function scale) a straight line is obtained. The quantities characterising the log-normal distribution (x_g and σ_g) can be simply obtained from the cumulative plot, viz.:

$$x_g = x_{50}, \text{ and } \sigma_g = x_{84}/x_{50} = x_{50}/x_{16} \quad (4.3.4)$$

where x_{50} , x_{84} , and x_{16} are the values of x for which F is 50%, 84%, and 16% respectively.

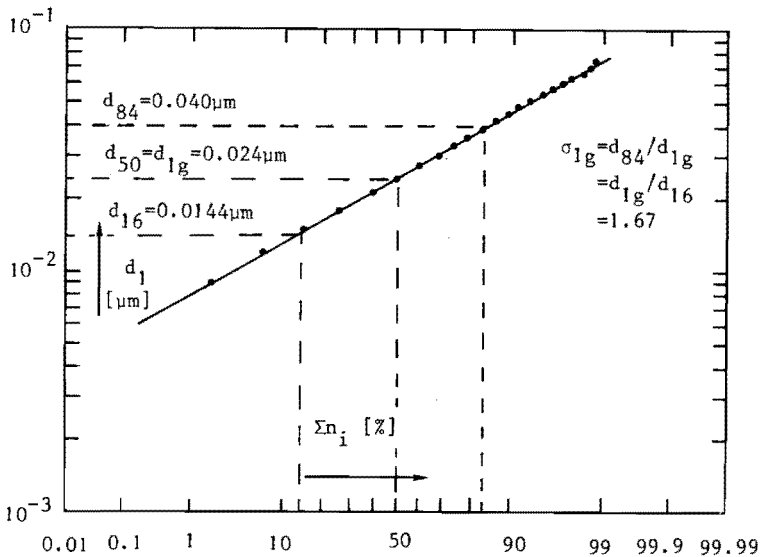


Figure 4.5. Cumulative primary particle size distribution on log-normal probability paper.

Kottler [52] argues that the log-normal distribution is useful for size distributions of particles resulting from dispersion of solids as well as from a process in which the growth of the particles is proportional to their size. The latter mechanism, for instance, occurs for particles resulting from a nuclear explosion, as has been shown by Stewart [91]. Concerning the primary particle size distribution of "exploding wire" aerosols, there is some discrepancy in the results reported in literature [74]. However, the primary particle size distributions obtained in this study satisfy the log-normal distribution fairly well, as is shown in figures 4.4 and 4.5. Therefore in this study the primary particle

size distributions of the "exploding wire" aerosols as well as the fluorescein aerosol are assumed to be log-normal. The geometric mean diameters (d_{1g}) and the geometric standard deviations (σ_{1g}) found, are given in table 4.1.

4.3.2. The aerodynamic diameter

Some typical results obtained for relations between the aerodynamic diameter and the mass, respectively number of primary particles, of the aggregates are given in figure 4.6.

The $n(d_a)$ curves were calculated from the $m(d_a)$ curves, obtained as described in section 4.2.3, using equation (4.3.2), which holds for the log-normal primary particle size distribution. Hence:

$$n(d_a) = m(d_a) \cdot \left\{ \frac{6}{\pi \rho d_1^3} \right\} = \frac{6m(d_a)}{\pi \rho d_{1g}^3 \exp\left[\frac{9}{2} \ln^2 \sigma_{1g}\right]} \quad (4.3.5)$$

The two solid straight lines in figure 4.6 represent the equations:

$$d_a = k_1 n^{\frac{1}{6}} (\rho/\rho_0)^{\frac{1}{2}} d_{1g} \exp\left[2 \ln^2 \sigma_{1g}\right] \quad (4.3.6)$$

and,

$$d_a = f_1 n^{\frac{1}{3}} (\rho/\rho_0)^{\frac{1}{2}} d_{1g} \exp\left[\frac{3}{2} \ln^2 \sigma_{1g}\right] \quad (4.3.7)$$

where k_1 and f_1 are factors independent of d_a and n .

Equations (4.3.6) and (4.3.7) can be deduced from equation (2.2.21) as follows. Introducing a new shape factor, $\tilde{\kappa} = \kappa C_s(d_a)/C_s(d_e)$, one finds from equation (2.2.21):

$$d_a = (\tilde{\kappa})^{-\frac{1}{2}} (\rho/\rho_0)^{\frac{1}{2}} d_e$$

and, with:

$$d_e = n^{\frac{1}{3}} (d_1^3)^{\frac{1}{3}} = n^{\frac{1}{3}} d_{1g} \exp\left[\frac{3}{2} \ln^2 \sigma_{1g}\right]$$

one has:

$$d_a = (\tilde{\kappa})^{-\frac{1}{2}} (\rho/\rho_0)^{\frac{1}{2}} n^{\frac{1}{3}} d_{1g} \exp\left[\frac{3}{2} \ln^2 \sigma_{1g}\right]$$

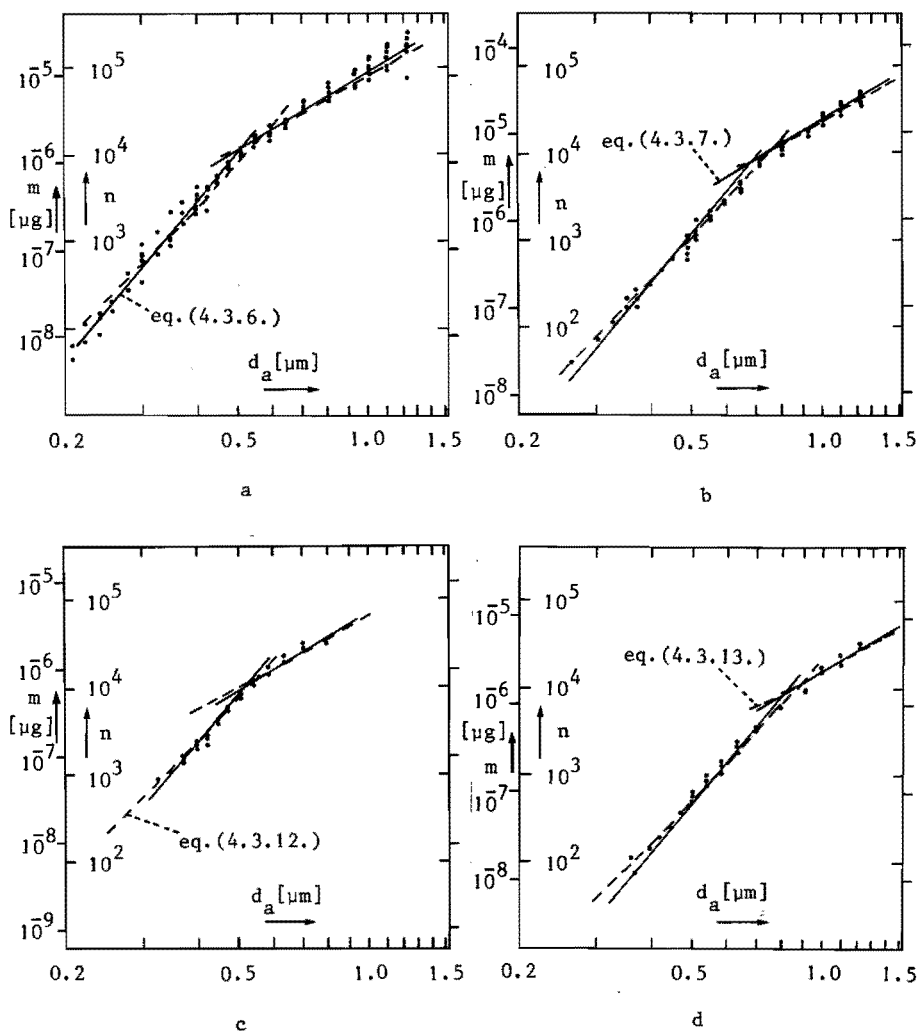


Figure 4.6. Relation between the aerodynamic diameter (d_a) and the number of primary particles (n), respectively mass (m) of branched chain-like aggregates.

- a: iron oxide, $d_{1g} = 0.028 \mu\text{m}$, $\sigma_{1g} = 1.67$;
- b: iron oxide, $d_{1g} = 0.042 \mu\text{m}$, $\sigma_{1g} = 1.68$;
- c: copper oxide, $d_{1g} = 0.020 \mu\text{m}$, $\sigma_{1g} = 1.55$;
- d: gold, $d_{1g} = 0.018 \mu\text{m}$, $\sigma_{1g} = 1.60$.

Hence, this equation is equivalent with eq. (4.3.7) with:

$$\tilde{\kappa} = 1/f_1^2 \quad (4.3.8)$$

which has been verified by Stöber [92,99] for cluster aggregates containing up to 23 monodisperse polystyrene spheres.

For the derivation of equation (4.3.6) a quantity called the sphericity (ϕ) is introduced: $\phi = \pi d_e^2/A$, where A is the surface area of the aggregate, given by:

$$A = n \pi d_1^2 = n \pi d_{lg}^2 \exp[2 \ln^2 \sigma_{lg}].$$

Hence one has:

$$\phi = n^{-\frac{1}{3}} \exp[\ln^2 \sigma_{lg}]$$

and,

$$d_a = (\tilde{\kappa}\phi)^{-\frac{1}{2}} (\rho/\rho_0)^{\frac{1}{2}} n^{\frac{1}{6}} d_{lg} \exp[2 \ln^2 \sigma_{lg}].$$

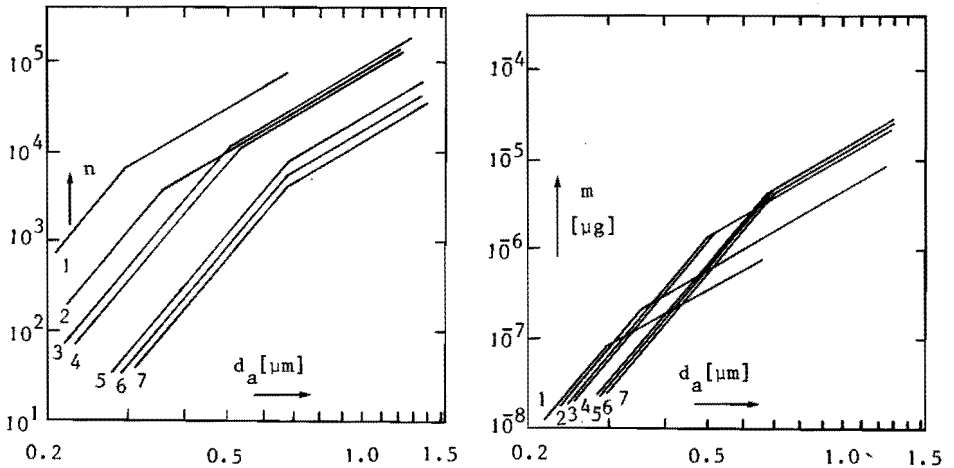


Figure 4.7. Summary of the results obtained for iron oxide aggregates according to the model given by equations (4.3.6) and (4.3.7)

Primary particle size distributions;

- 1: $d_{lg} = 0.013 \mu\text{m}$, $\sigma_{lg} = 1.51$; 2: $d_{lg} = 0.019 \mu\text{m}$, $\sigma_{lg} = 1.66$;
- 3: $d_{lg} = 0.024 \mu\text{m}$, $\sigma_{lg} = 1.67$; 4: $d_{lg} = 0.028 \mu\text{m}$, $\sigma_{lg} = 1.63$;
- 5: $d_{lg} = 0.042 \mu\text{m}$, $\sigma_{lg} = 1.63$; 6: $d_{lg} = 0.044 \mu\text{m}$, $\sigma_{lg} = 1.70$;
- 7: $d_{lg} = 0.047 \mu\text{m}$, $\sigma_{lg} = 1.70$.

Equation (4.3.6) corresponds to:

$$\tilde{\kappa}\phi = 1/k_1^2 \quad (4.3.9)$$

This relation has been established by Stöber [92,99] for linear aggregates of not more than 8 monodisperse polystyrene spheres.

In figure 4.7 a summary is given of the results obtained for the iron aggregates. The straight lines are described by equations (4.3.6) and (4.3.7). In table 4.1 the values of k_1 and f_1 are given. In figure 4.8 the relation between k_1 and the mean diameter of the primary particles (\bar{d}_1) is shown, while in figure 4.9 the relation between f_1 and \bar{d}_1 is given.

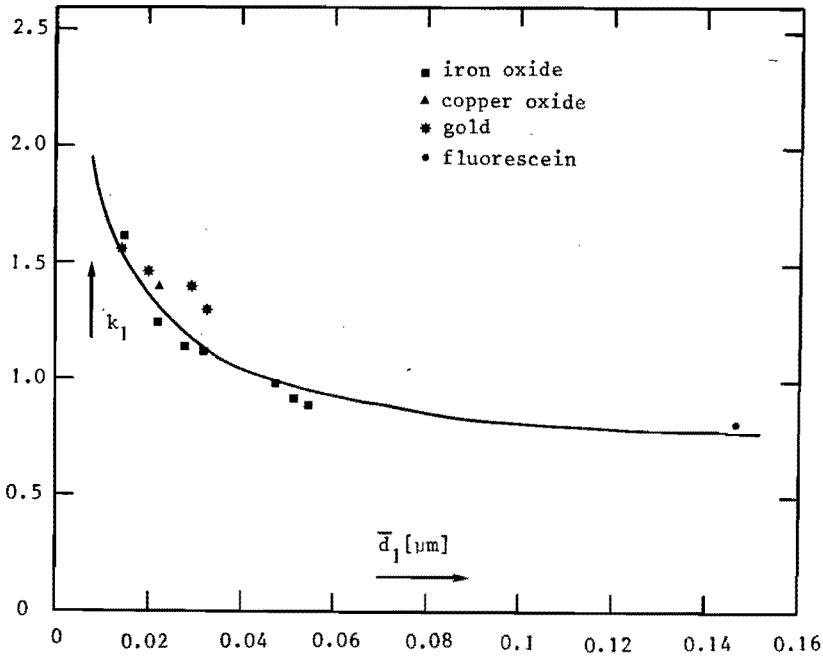


Figure 4.8. Relation between mean primary particle diameter (\bar{d}_1) and k_1 (eq. 4.3.6). The solid line represents equation (4.4.2) with: $\kappa = 0.65$, and $w = 3$.

According to equation (4.3.9), the fluid drag on the aggregates satisfying equation (4.3.6) is directly related to their surface area, and it also depends on the volume equivalent diameter. The fluid drag on the aggregates satisfying equation (4.3.7) is proportional to their volume equivalent diameters, as follows from equation (4.3.8). The agreement with the aerodynamic characteristics of linear and cluster aggregates of

Table 4.1. Review of experimental results on various aerosols.

generation method	chemical composition	ρ [g.cm ⁻³]	primary particle size distribution			k_1 (eq.4.3.6)	f_1 (eq.4.3.7)	$k_2\sqrt{C_n^1}$ (eq.4.3.12)	$f_2\sqrt{C_n^1}$ (eq.4.3.13)
			d_{1g} [μm]	σ_{1g}	\bar{d}_1 [μm]				
E.W. ⁺ , iron ⁺⁺ , 0.05 ⁺⁺⁺ , 15 ⁺⁺⁺⁺	Fe ₂ O ₃	5.24	0.013	1.51	0.014	1.61	0.419	2.12	0.496
E.W., iron, 0.1, 15	Fe ₂ O ₃		0.019	1.66	0.022	1.25	0.362	1.58	0.408
E.W., iron, 0.25, 15	Fe ₂ O ₃		0.024	1.67	0.027	1.14	0.276	1.39	0.307
E.W., iron, 0.25, 10	Fe ₂ O ₃		0.028	1.63	0.032	1.12	0.263	1.36	0.292
E.W., iron, 0.5, 15	Fe ₂ O ₃		0.042	1.63	0.047	0.99	0.252	1.16	0.278
E.W., iron, 0.5, 10	Fe ₂ O ₃		0.044	1.70	0.051	0.99	0.254	1.09	0.277
E.W., iron, 1.0, 15	Fe ₂ O ₃		0.047	1.70	0.054	0.90	0.258	1.04	0.283
E.W., gold, 0.1, 15	Au	19.1	0.013	1.50	0.014	1.57	0.390	1.90	0.436
E.W., gold, 0.2, 15	Au		0.018	1.60	0.020	1.47	0.360	1.69	0.390
E.W., gold, 0.5, 15	Au		0.029	1.55	0.033	1.32	0.310	1.44	0.320
E.W., gold, 1.0, 15	Au		0.025	1.57	0.028	1.40	0.310	1.53	0.320
E.W., copper, 0.2, 15	±40% CuO, 60% Cu ₂ O	6.25	0.020	1.55	0.022	1.40	0.360	1.65	0.404
Spraying	Amm. Fluoresc.	1.45	0.118	1.95	0.147	0.81	0.70	0.98	0.78

⁺ Exploding wire, ⁺⁺ material of exploded wire, ⁺⁺⁺ diameter of exploded wire [mm], ⁺⁺⁺⁺ tension on capacitor (kV)

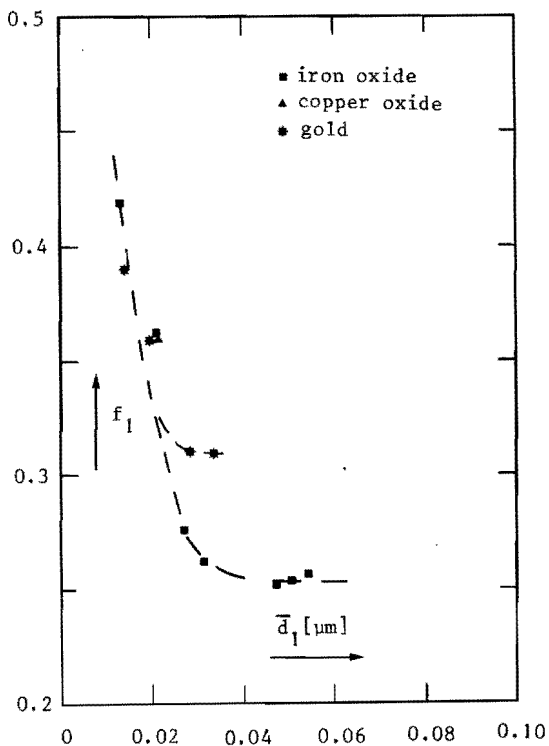


Figure 4.9. Relation between mean primary particle diameter (\bar{d}_1) and f_1 (equation 4.3.7), obtained for exploding wire aggregates.

monodisperse polystyrene spheres respectively, indicates that there should be some correspondence in shape. This suggests that the configuration of the aggregates satisfying equation (4.3.6) should be more or less linear, whereas the aggregates satisfying equation (4.3.7) should have a more or less spherical configuration. These suggestions are justified by electron microscope pictures of aggregates from both regions, which are shown in figure 4.10.

Equations (4.3.8) and (4.3.9), and therefore equations (4.3.7) and (4.3.6) involve neglect of the influence of slip, which is a significant simplification. Therefore another model is applied, in which the influence of slip is taken into account. The basic assumption of this model is, that equations (4.3.8) and (4.3.9) are correct in the continuum flow region.

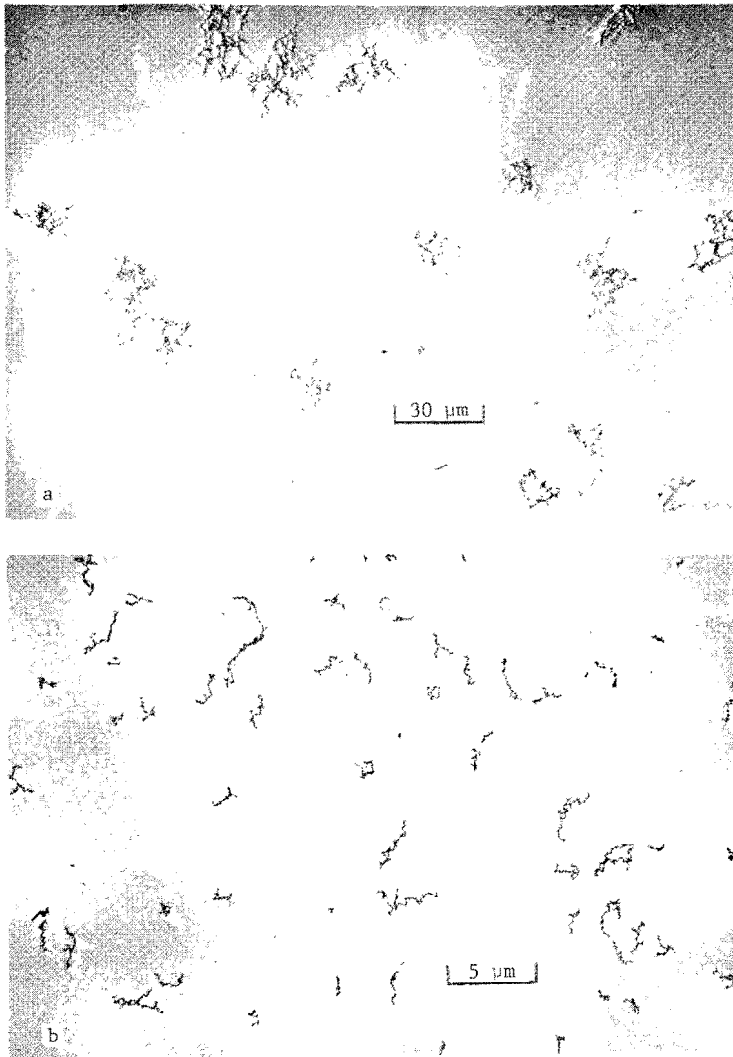


Figure 4.10. Electron microscope picture of branched chain-like iron oxide aggregates ($d_{lg} = 0.028 \mu\text{m}$, $\sigma_{lg} = 1.63$).
a: $d_a = 0.925 \mu\text{m}$, $n = 4.3 \times 10^4$;
b: $d_a = 0.259 \mu\text{m}$, $n = 145$.

Thus, for the linearly shaped aggregates it is assumed that:

$$\kappa(0)\phi = 1/k_2^2 \quad (4.3.10)$$

while for the irregularly shaped threedimensional networks it is assumed that:

$$\kappa(0) = 1/f_2^2 \quad (4.3.11)$$

where: $\kappa(0)$ = dynamic shape factor at $Kn = 0$,
 k_2 and f_2 are constants.

When the relation between $\kappa(0)$ and the dynamic shape factor at arbitrary Kn , $\kappa(Kn)$, as given by equation (2.2.14) is combined with equation (2.2.21), the following equations can be derived from (4.3.10) and (4.3.11):

$$d_a = k_2 \{C'_n(Kn)/C_s(d_a)\}^{\frac{1}{2}} n^{\frac{1}{6}} (\rho/\rho_0)^{\frac{1}{2}} d_{1g} \exp[2 \ln^2 \sigma_{1g}] \quad (4.3.12)$$

and,

$$d_a = f_2 \{C''_n(Kn)/C_s(d_a)\}^{\frac{1}{2}} n^{\frac{1}{3}} (\rho/\rho_0)^{\frac{1}{2}} d_{1g} \exp[\frac{3}{2} \ln^2 \sigma_{1g}] \quad (4.3.13)$$

where, C'_n = slip correction factor for the linearly shaped aggregates,
 C''_n = slip correction factor for the threedimensional networks.

These equations provide a relation between aerodynamic diameter and micro-structure, which is physically more meaningful than (4.3.6) and (4.3.7). In figure 4.6, equations (4.3.12) and (4.3.13) are presented by the dashed lines, assuming that C'_n as well as C''_n are independent of n . The good agreement between the experimental results and the dashed lines supports this assumption. A summary of the results obtained for the iron oxide aggregates, represented by equations (4.3.12) and (4.3.13) is shown in figure 4.11. The values obtained for $k_2\sqrt{C'_n}$ and $f_2\sqrt{C''_n}$ are given in table 4.1, while the relations between these quantities and \bar{d}_1 are shown in figures 4.12 and 4.13.

Often one is interested in the dynamic shape factors of the particles. Using equation (2.2.21), the dynamic shape factors of the aggregates can be calculated from the relation between d_a and n . Some typical results of relations between κ and n obtained in this way are given in figure 4.14. The solid lines in this figure represent equations (4.3.8) and (4.3.9), while equations (4.3.10) and (4.3.11) are represented by the dashed lines.

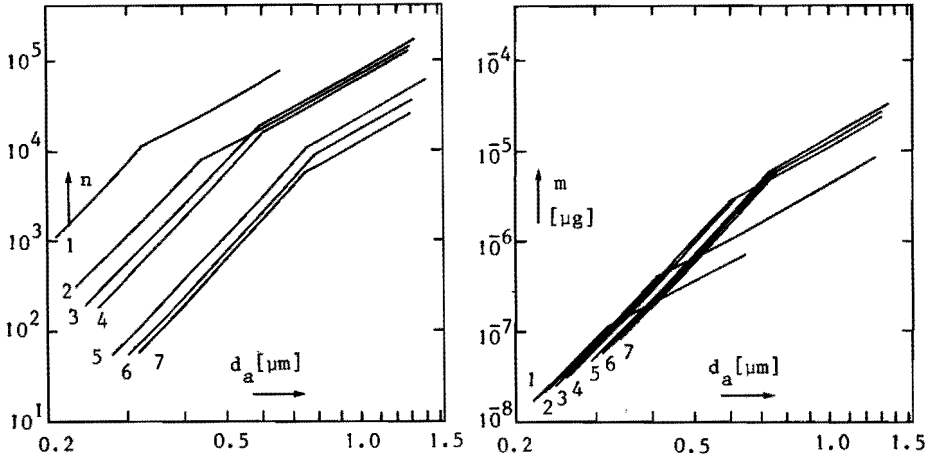


Figure 4.11. Summary of the results obtained for iron oxide aggregates, according to the model given by equations (4.3.12) and (4.3.13). Primary particle size distributions;

- 1: $d_{lg} = 0.013 \mu\text{m}$, $\sigma_{lg} = 1.51$; 2: $d_{lg} = 0.019 \mu\text{m}$, $\sigma_{lg} = 1.66$;
- 3: $d_{lg} = 0.024 \mu\text{m}$, $\sigma_{lg} = 1.67$; 4: $d_{lg} = 0.028 \mu\text{m}$, $\sigma_{lg} = 1.63$;
- 5: $d_{lg} = 0.042 \mu\text{m}$, $\sigma_{lg} = 1.63$; 6: $d_{lg} = 0.044 \mu\text{m}$, $\sigma_{lg} = 1.70$;
- 7: $d_{lg} = 0.047 \mu\text{m}$, $\sigma_{lg} = 1.70$.

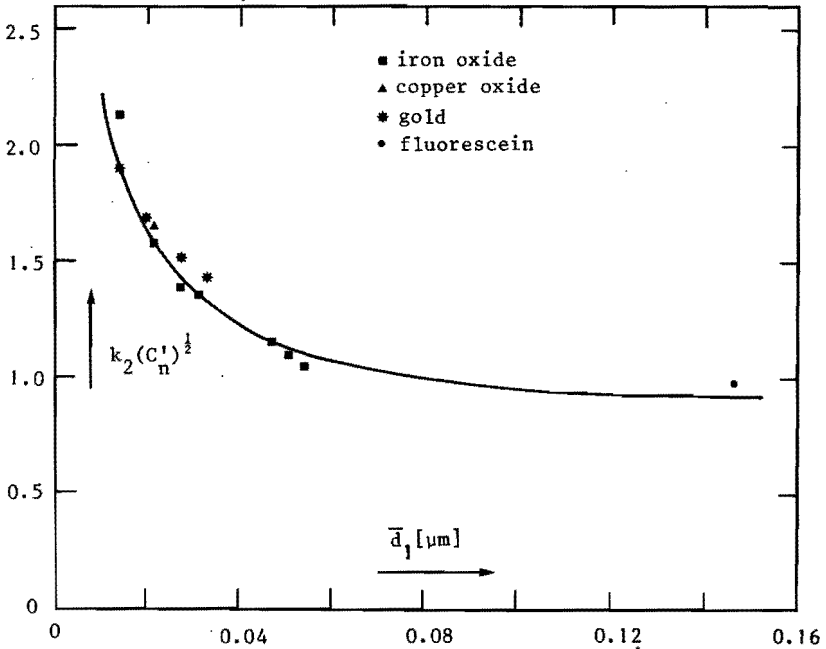


Figure 4.12. Relation between mean primary particle diameter (\bar{d}_1) and $k_2\sqrt{C'_n}$ (eq. 4.3.12). The solid line corresponds with equation (4.4.1) with: $k_2 = 0.77$, and $w = 3$.

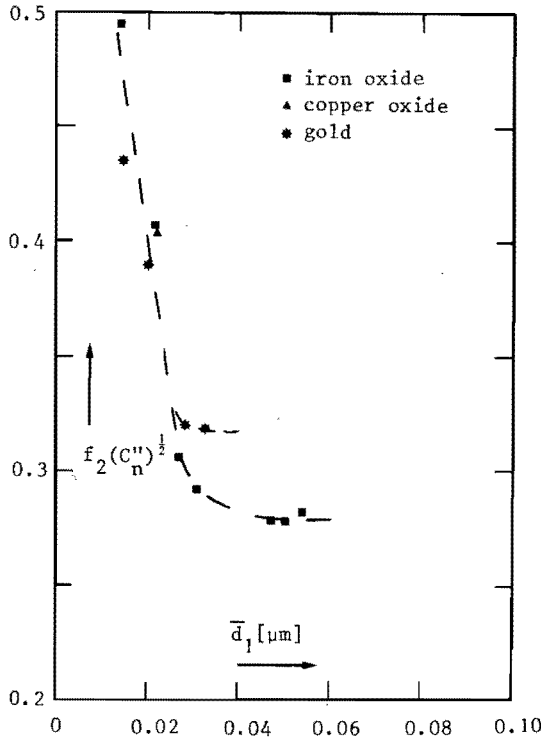


Figure 4.13. Relation between mean primary particle diameter (\bar{d}_1) and $f_2 \sqrt{C_n''}$ (eq. 4.3.13), obtained for exploding wire aggregates.

Because fluid drag is a surface effect, it is worthwhile to introduce a dynamic surface area shape factor, κ_s , defined as the ratio of the fluid drag on the particle in question, and the fluid drag on a sphere having equal velocity and surface area. By simple algebra the following expression for κ_s is obtained.

$$\kappa_s = (d_e/d_{se}) \{C_s(d_{se})/C_s(d_e)\} \kappa \quad (4.3.14)$$

where d_{se} = diameter of a sphere with the same surface area as the aggregate = $n^{1/2} d_{1g} \exp[\ln^2 \sigma_{1g}]$.

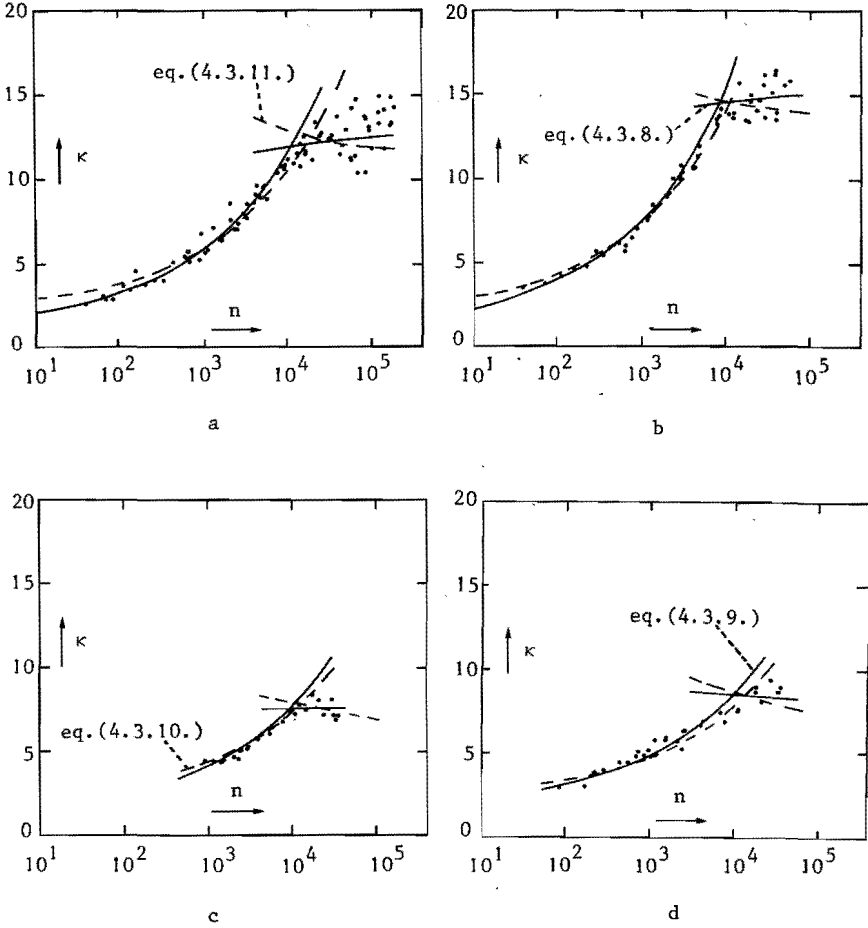


Figure 4.14. Relation between dynamic shape factor (κ) and the number of primary particles (n).

- a: iron oxide, $d_{1g} = 0.028 \mu\text{m}$, $\sigma_{1g} = 1.67$;
- b: iron oxide, $d_{1g} = 0.042 \mu\text{m}$, $\sigma_{1g} = 1.63$;
- c: copper oxide, $d_{1g} = 0.020 \mu\text{m}$, $\sigma_{1g} = 1.55$;
- d: gold, $d_{1g} = 0.018 \mu\text{m}$, $\sigma_{1g} = 1.60$.

For the linearly shaped aggregates the model, neglecting slip influences (eq. 4.3.9), gives with (4.3.14):

$$\kappa_s = (1/k_1)^2 \{C_s(d_{se})/C_s(d_a)\} n^{\frac{1}{6}} \exp[-\frac{1}{2} \ln^2 \sigma_{1g}], \quad (4.3.15)$$

while the model including slip influences (equation 4.3.10 together with 2.2.14) gives:

$$\kappa_s = (1/k_2)^2 \{C_s(d_{se})/C'_n(Kn)\} n^{\frac{1}{6}} \exp[-\frac{1}{2} \ln^2 \sigma_{1g}]. \quad (4.3.16)$$

For the threedimensional networks one finds for the model neglecting slip influences (eq. 4.3.8) from equation (4.3.14):

$$\kappa_s = (1/f_1)^2 \{C_s(d_{se})/C_s(d_e)\} n^{-\frac{1}{6}} \exp[\frac{1}{2} \ln^2 \sigma_{1g}], \quad (4.3.17)$$

while the model including slip influences (equation 4.3.11 together with 2.2.14) gives:

$$\kappa_s = (1/f_2)^2 \{C_s(d_{se})/C''_n(Kn)\} n^{-\frac{1}{6}} \exp[\frac{1}{2} \ln^2 \sigma_{1g}]. \quad (4.3.18)$$

In figure 4.15 some typical results obtained for the relation between κ_s and n are given. The solid lines in this figure represent equations (4.3.15) and (4.3.17), while equations (4.3.16) and (4.3.18) are represented by dashed lines. The results show that equation (4.3.15) as well as (4.3.16) have a minimum, which is a result of slip influences.

4.4. Discussion

The results obtained for the relations between n and d_a of branched chain-like aggregates show that two regions can be distinguished. These regions correspond with more or less linearly shaped aggregates and irregularly shaped threedimensional networks respectively. The relation between d_a and n holding for the linear aggregates is given by equations (4.3.6) or (4.3.12), while for the irregular networks this relation is given by equations (4.3.7) or (4.3.13). Equations (4.3.12) and (4.3.13) are physically more meaningful than equations (4.3.6) and (4.3.7), because they account for the influence of slip. Nevertheless the two sets of equations differ so little that they both fit the experimental results. The two regions as well as the transition between them are discussed below.

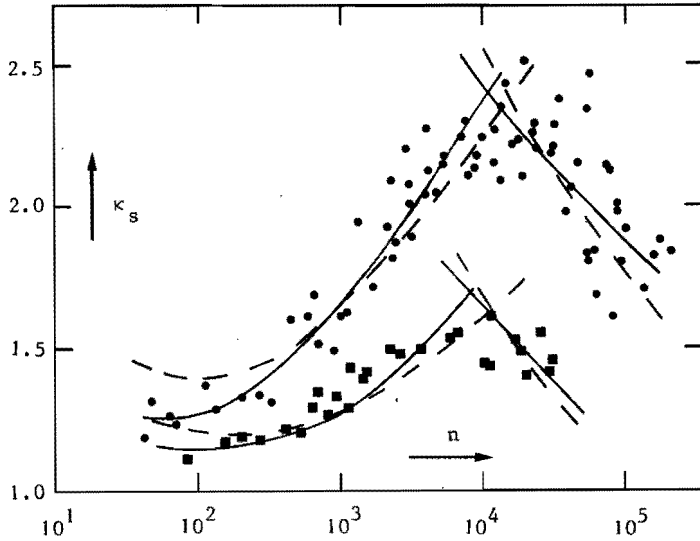


Figure 4.15. Relation between dynamic surface area shape factor (κ_s) and the number of primary particles (n) of branched chain-like aggregates. ●: iron oxide, $d_{lg} = 0.024 \mu\text{m}$, $\sigma_{lg} = 1.67$; ■: gold, $d_{lg} = 0.018 \mu\text{m}$, $\sigma_{lg} = 1.60$. The solid lines represent equations (4.3.15) and (4.3.17). The dashed lines represent equations (4.3.16) and (4.3.18).

4.4.1. Linear aggregates

The empirical relations (4.3.9) and (4.3.10) fairly well agree with the theoretical solutions obtained for prolate spheroids (cf. section 2.2) having an aspect ratio (q) smaller than about 100. In that q -region, the product $\kappa_p \phi$ of prolate spheroids, randomly rotating during settling (κ_p is given by eq. 2.2.10), varies around unity by not more than about 10%. However, above $q = 100$, $\kappa_p \phi$ steadily increases with increasing q ($\kappa_p \phi = 2.83$ at $q = 10^4$). This indicates that aggregates with less than about 100 primary particles can be approximated by prolate spheroids, while such an approximation cannot be applied to larger aggregates. The reason for this is an increasing irregularity of the aggregates with increasing aggregate size. Obviously this makes the fluid drag increase with increasing aggregate size not according to the expression for a prolate spheroid, but at a slower rate such that $\kappa \phi$ remains constant.

This possibly is due to an increase of void spaces in the aggregates. However, the physical reasons for the constancy of $\kappa\phi$ are not well understood as yet.

The proportionality factor k_1 in eq. (4.3.6) increases with decreasing primary particle size as is shown in figure 4.8. By extrapolating the $k_1(\bar{d}_1)$ relation to the primary particle size of the linear aggregates studied by Stöber ($d_1 > 0.2 \mu\text{m}$) [92,99], a value of k_1 is obtained that is significantly smaller than the one found by Stöber (i.e. $k_1 = 1.077$). The reason for this is that, in contrast to the aggregates studied by Stöber, the structure of the present aggregates is far from perfectly linear. This causes a larger fluid drag which results in a smaller value of k_1 . The increase of k_1 with decreasing \bar{d}_1 is caused by the slip effect, the influence of which increases with decreasing primary particle size. This illustrates the imperfection of the model given by equation (4.3.6), which neglects slip.

The factor $k_2\sqrt{C'_n}$ of equation (4.3.12), which includes slip influences, also increases with decreasing \bar{d}_1 . Similarly there is a discrepancy between the $k_2\sqrt{C'_n(\bar{d}_1)}$ -curve (figure 4.12) and the $k_2\sqrt{C'_n}$ value which can be calculated from Stöber's results ($k_2\sqrt{C'_n} > 1.077$). The reason for the increase of $k_2\sqrt{C'_n}$ with decreasing \bar{d}_1 is that the slip correction factor C'_n evidently increases with decreasing \bar{d}_1 , while k_2 is a constant. As already mentioned in section 2.2, up to now slip correction factors have been established as empirical factors for spherical particles only. The slip correction factors of non-spherical particles must be obtained by means of approximation methods. The best approximation method is the "adjusted sphere" method, introduced by Dahneke (cf. section 2.2). However, strictly speaking this method cannot be used in the present study, because it demands that the fluid drag is known in the continuum flow region as well as at an arbitrary large value of Kn, data which are not available. Nevertheless, by means of a slight modification of the method an approximation of C'_n can be obtained. In this modified method, similar to the original method, C'_n is approximated by:

$$C'_n(\text{Kn}) = 1 + A\left(\frac{\text{Kn}}{w}\right) + Q\left(\frac{\text{Kn}}{w}\right) \exp\left[-B\left(\frac{w}{\text{Kn}}\right)\right] \quad (4.4.1)$$

Where for A, B, and Q the Millikan data (cf. section 2.1) are employed. Starting from the measured values of $k_2\{C'_n(\text{Kn})\}^{\frac{1}{2}}$, values of w and k_2 are calculated such that a most probable fit is obtained. Assuming that the

mean radius of the primary particles may be considered as the characteristic length of the aggregates (thus: $Kn = \bar{l}/\frac{1}{2}\bar{d}_1$) we obtained: $k_2 = 0.77$ and $w = 3$. The solid line in figure 4.12 corresponds with these values of k_2 and w . The fit between the measured values and the approximate expression for $k_2\sqrt{C'_n}$ is fairly good.

In the model given by equation (4.3.6) also a slip correction factor for the aggregates, C'_n , can be introduced, by writing:

$$k_1 = K\{C'_n(Kn)\}^{\frac{1}{2}} \quad (4.4.2)$$

with constant K .

However, this model has less physical meaning than the previous one, because it still involves the neglect of $C_s(d_a)$. Nevertheless, an approximation for $C'_n(Kn)$ can be obtained by means of (4.4.1) and (4.4.2) in a similar way as described above. The solid line in figure 4.8 corresponds with $K = 0.65$ and $w = 3$. The fit with the experimental results is satisfactory. With respect to these results, it must be remarked that there is a significant discrepancy between some values of k_1 obtained for gold aggregates and iron oxide aggregates. From a theoretical point of view there might be an influence of the particle material, due to different accommodation of the gas molecules colliding with the particle [113]. This would result in different values of A , B , and Q in the slip correction formula. However, in aerosol physics, independent of the particle material, generally the Millikan data obtained for oil drops (cf. section 2.1) are employed successfully for A , B , and Q . This indicates that A , B , and Q are only slightly dependent on the particle material. Hence, it is rather unlikely that the discrepancy in the k_1 values results from a dependence of A , B and Q on the material used. A more probable explanation is, that this discrepancy is a result of the inadequacy of the model used, the more so as such a discrepancy is almost absent in the experimental results for $k_2\sqrt{C'_n}$.

4.4.2. Threedimensional networks

The two alternative equations (4.3.7) and (4.3.13) describing the relation between d_a and n of the threedimensional networks differ only slightly, as is shown in figure 4.6. The physical explanation of these equations is that the structure of the aggregates does not vary with their size. Al-

though the configuration of the aggregates is far from exactly spherical, they can be approximated by a sphere of equal mass and geometric size. Thus, assuming that no fluid passes through the aggregates, their aerodynamic diameter is approximately given by:

$$d_a = (\rho_a / \rho_0)^{\frac{1}{2}} \{C_s(d_p) / C_s(d_a)\}^{\frac{1}{2}} d_p \quad (4.4.3)$$

where: d_p = diameter of sphere of equal geometric size as the aggregate, the determination of which is described below,
 ρ_a = apparent density of the sphere
 $= m / (\frac{1}{6} \pi d_p^3) = \rho (d_e / d_p)^3$.

Equation (4.4.3) can be rewritten as:

$$d_a = (d_e / d_p)^{\frac{1}{2}} \{C_s(d_p) / C_s(d_a)\}^{\frac{1}{2}} (\rho / \rho_0)^{\frac{1}{2}} n^{\frac{1}{3}} d_{1g} \exp[\frac{3}{2} \ln^2 \sigma_{1g}] \quad (4.4.4)$$

Although equation (4.4.3), and therefore (4.4.4), hinges on the somewhat questionable assumption that no fluid passes through the aggregate, it is supported by measurements of aggregate sizes with respect to their mass and aerodynamic diameter. The results of these measurements are given in table 4.2. The aggregate sizes are obtained by means of optical microscopy. The diameter d_p is chosen as the diameter of a circle of equal area as the area within the outer contour of an aggregate projection. The results show that the aerodynamic diameter calculated from the aggregate size and mass by means of equation (4.4.3) differs by no more than a few percent from the aerodynamic diameter measured with the centrifuge.

Comparison of (4.4.4) with (4.3.13) indicates that the slip correction factor of the threedimensional networks, $C_n''(Kn)$, is equal to $C_s(d_p)$. Because of the magnitude of the d_p values of the aggregates, $C_s(d_p)$ and therefore C_n'' are practically equal to one. This, together with equations (4.4.4), (4.3.7), and (4.3.13) gives:

$$f_1 = \{C_s(d_a)\}^{-\frac{1}{2}} (d_e / d_p)^{\frac{1}{2}}, \quad \text{while} \quad f_2 = (d_e / d_p)^{\frac{1}{2}} \quad (4.4.5)$$

The ratio (d_e / d_p) is a measure of the packing density of the primary particles in the aggregates. Thus (4.4.5) shows, that f_1 and f_2 are measures of the packing density as well. According to equation (4.4.5)

Table 4.2. Size of threedimensional iron oxide aggregates related to their mass and aerodynamic diameter.*)

d_p [μm]	m [10^{-6} μg]	$(d_a)_1$ [μm]	$(d_a)_2$ [μm]	$(d_a)_1/(d_a)_2$
10.4	2.51	0.616	0.602	1.02
12.3	3.41	0.677	0.651	1.04
12.3	4.67	0.755	0.771	0.98
16.6	5.75	0.803	0.739	1.09
17.0	8.80	0.925	0.915	1.01
19.1	10.8	1.005	0.962	1.05
18.1	14.4	1.103	1.15	0.96

the packing density decreases slightly with increasing n , because f_1 does not depend on n and $C_s(d_a)$ decreases slightly with increasing n . This is rather unlikely, and it again illustrates the imperfection of the model described by equation (4.3.7), which neglects slip influences.

The values of f_1 and f_2 obtained for the exploding wire aggregates strongly increase with decreasing \bar{d}_1 in the region $\bar{d}_1 \lesssim 0.03 \mu\text{m}$, while for $\bar{d}_1 \gtrsim 0.03 \mu\text{m}$ these factors show only a slight dependence on \bar{d}_1 (cf. figures 4.9 and 4.13). Thus, in the former region the packing density strongly increases with decreasing \bar{d}_1 , whereas in the latter region the packing density hardly varies. This is supported by microscopic observations. A physical explanation for this behaviour could not be found, but it is in agreement with observations with respect to iron oxide aggregates produced by photochemical decomposition of ironpentacarbonyl vapors [100]. The aerosol produced in this way consists of more or less spherical aggregates composed by a very large number of closely packed, very small primary particles ($\bar{d}_1 < 2 \text{ nm}$). The values of f_1 and f_2 corresponding with the packing densities of these particles will be close to 0.9 as Stöber found for cluster aggregates. This is in agreement with the behaviour shown in figures 4.9 and 4.13.

*) The standard deviation of the d_p measurements is about 15%;
 m is deduced from the results reported in section 4.3;
 $(d_a)_1$ = aerodynamic diameter obtained by means of centrifuge;
 $(d_a)_2$ = aerodynamic diameter calculated from equation (4.4.3).

The f_1 and f_2 values obtained for the gold and iron oxide aggregates show some discrepancy in the region $\bar{d}_1 \gtrsim 0.03 \mu\text{m}$. The values of f_1 and f_2 found for the fluoresceine aggregates strongly deviate from the values obtained for the exploding wire aggregates. These discrepancies may originate from the role of Brownian rotation in the coagulation process, as is discussed in more detail in the next section.

4.4.3. *The transition from linear aggregates to threedimensional networks*

All the results reported indicate that the transition from the region described by (4.3.6) or (4.3.12) to the region described by (4.3.7) or (4.3.13) is rather sudden. This means that the transition from linearly shaped aggregates to threedimensional networks is a rather abrupt one. A conclusion which is supported by microscopic observations. The reason for this might be found in the coagulation process, more explicitly the role of the Brownian rotation in this process. One can imagine that two rotating chains, when coagulating, preferentially contact at the chain ends, thus forming a longer chain. However, Brownian rotation decreases with increasing chain length, which would cause an increased probability of the formation of threedimensional networks by coagulation. This probability also will depend on the translational velocities of the chains. On the time scale as well as length scale coagulation takes place, the translation of the particles will be mainly of Brownian nature. Brownian motion of a single particle cannot be described continuously in time. Therefore the above given reasoning cannot be supported by fundamental calculations. However, some information about the Brownian rotation can be obtained from consideration of the rotational energy of a particle. One has:

$$\frac{1}{2} J \overline{\omega^2} = \frac{1}{2} kT \quad (4.4.6)$$

where, J = moment of inertia,
 ω = angular velocity [rad/s],
 k = Boltzmann constant,
 T = temperature [K].

The bar denotes an average value.

The moment of inertia of a perfectly linear chain with respect to rotation around an axis perpendicular to the chain and passing through its

center of mass, is given by:

$$J = \frac{1}{72} \pi \rho n^3 d_{1g}^5 \exp[5.5 \ln^2 \sigma_{1g}] \quad (4.4.7)$$

In figure 4.16 the relation between $(\overline{\omega^2})^{\frac{1}{2}}$ and n is given for the aerosols studied. The arrows mark the transition from linearly shaped aggregates to threedimensional networks. From this figure it can be seen that the

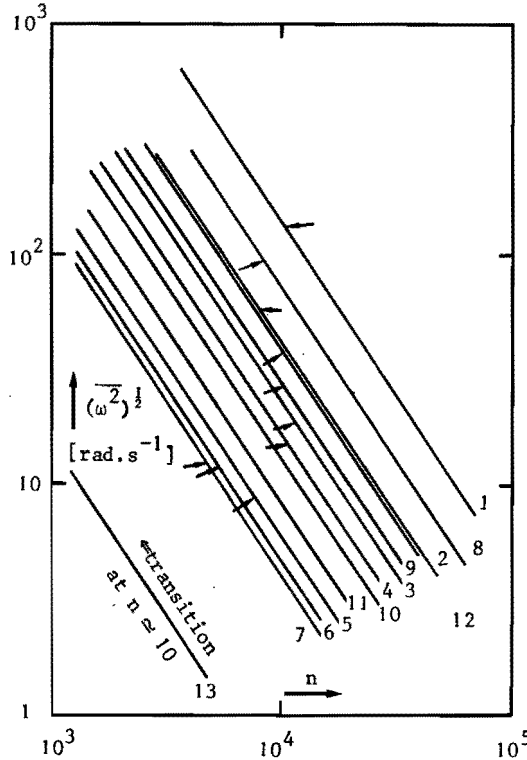


Figure 4.16. Relation between mean Brownian angular velocity $(\overline{\omega^2})^{\frac{1}{2}}$ and the number of primary particles of perfectly linear chains.

1-7 iron oxide; 8-11 gold; 12 copper oxide; 13 fluorescein.

Primary particle size distributions:

- | | |
|---|---|
| 1: $d_{1g} = 0.013 \mu\text{m}$, $\sigma_{1g} = 1.51$; | 2: $d_{1g} = 0.019 \mu\text{m}$, $\sigma_{1g} = 1.66$; |
| 3: $d_{1g} = 0.024 \mu\text{m}$, $\sigma_{1g} = 1.67$; | 4: $d_{1g} = 0.028 \mu\text{m}$, $\sigma_{1g} = 1.63$; |
| 5: $d_{1g} = 0.042 \mu\text{m}$, $\sigma_{1g} = 1.63$; | 6: $d_{1g} = 0.044 \mu\text{m}$, $\sigma_{1g} = 1.70$; |
| 7: $d_{1g} = 0.047 \mu\text{m}$, $\sigma_{1g} = 1.70$; | 8: $d_{1g} = 0.013 \mu\text{m}$, $\sigma_{1g} = 1.50$; |
| 9: $d_{1g} = 0.018 \mu\text{m}$, $\sigma_{1g} = 1.60$; | 10: $d_{1g} = 0.025 \mu\text{m}$, $\sigma_{1g} = 1.57$; |
| 11: $d_{1g} = 0.029 \mu\text{m}$, $\sigma_{1g} = 1.55$; | 12: $d_{1g} = 0.020 \mu\text{m}$, $\sigma_{1g} = 1.55$; |
| 13: $d_{1g} = 0.118 \mu\text{m}$, $\sigma_{1g} = 1.95$. | |

The arrows mark the transition from linearly shaped aggregates to threedimensional networks, as being observed.

transition of the exploding wire aggregates composed of primary particles with a mean diameter larger than about $0.03 \mu\text{m}$, indeed correspond with small values of $(\overline{\omega^2})^{\frac{1}{2}}$. However, for $\overline{d}_1 \lesssim 0.03 \mu\text{m}$ the Brownian angular velocity corresponding with the transition point strongly increases with decreasing \overline{d}_1 , while furthermore the transition point of the fluorescein aggregates is at a rather large value of $(\overline{\omega^2})^{\frac{1}{2}}$. Therefore, these calculations provide no strong arguments for the theory according to which the rather abrupt transition from linear aggregates to threedimensional networks results from the role of Brownian rotation in the coagulation process. Nevertheless it seems to be a plausible theory, the more so as it gives some explanation for the observed discrepancies in the values of f_1 and f_2 . The discrepancy between the values obtained for the gold and iron oxide aggregates (cf. figures 4.9 and 4.13) may be ascribed to the larger density of gold, which reduces the Brownian rotation. Thus the transition from linear aggregates to threedimensional networks is expected to occur at a smaller value of n . This results in larger values of f_1 and f_2 .

The large values of f_1 and f_2 of the fluorescein aggregates can be explained by the fact that these aggregates result from a coagulation process during which over a long time interval individual primary particles are introduced, this in contrast to the coagulation process for the exploding wire aggregates. Obviously in such a coagulation system the role of Brownian rotation is less significant.

4.4.4. Comparison with literature data

As already mentioned in section 4.1, the fluid drag on branched chain-like aggregates has also been studied by Vomela and Whitby [108], and Whytlaw-Gray and Patterson [112]. Unfortunately the accuracy of their results is too poor to allow a fair comparison with the present results. Furthermore these results are given in terms different from those in which the present results are given. Nevertheless, to allow some comparison, the results of Whytlaw-Gray and Patterson, as well as those of Vomela and Whitby were converted to obtain the quantities used in the present study.

Figure 4.17a shows the relation between m and d_e , recalculated from the results obtained by Whytlaw-Gray and Patterson for gold aggregates, generated in an arc between two gold electrodes. Because primary particle

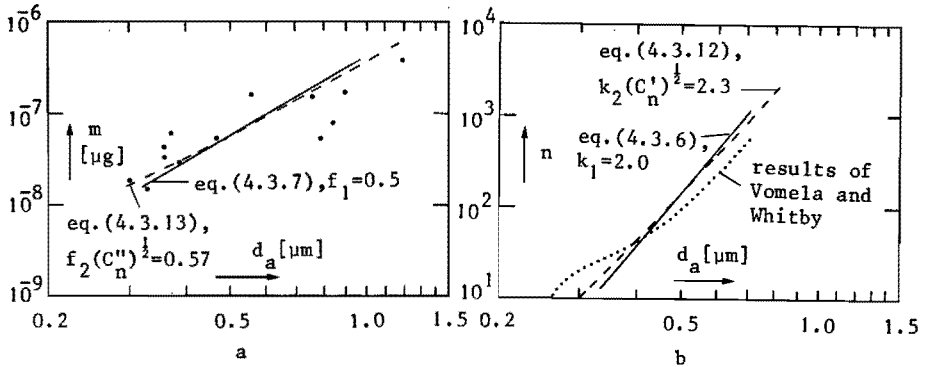


Figure 4.17. Comparison of our results with literature data.

a: results of Whytlaw-Gray and Patterson [112], obtained for gold aggregates (•).

b: results of Vomela and Whitby [108], obtained for copper oxide aggregates.

size distributions are not given in the original report, the number of primary particles of the aggregates could not be calculated. These results have been obtained by the original authors for aggregates with a more or less spherical configuration. Therefore, these results can be expected to obey equations (4.3.7) and (4.3.13). Figure 4.17a shows that, apart from the wide scatter they do not deviate too far from these equations. According to the present results, the values of f_1 and $f_2\sqrt{C''_n}$ (resp. 0.5 and 0.57) correspond with a mean primary particle diameter of about $0.01 \mu\text{m}$.

As already mentioned in section 4.1, due to an erroneous calculation, the original paper of Vomela and Whitby contains results which show Stokes diameters of branched chain-like aggregates being even larger than their volume equivalent diameters. This should correspond with dynamic shape factors smaller than unity, which is in total disagreement with the results of the present study (cf. figure 4.14). The $n(d_a)$ -curve shown in figure 4.17b is obtained from the results of Vomela and Witby for copper oxide aggregates, produced by an exploding wire, by a correct calculation. The electron micrographs reported in the original paper, indicate that the aggregates were mainly linearly shaped. Therefore, the $n(d_a)$ relation should obey relations (4.3.6) and (4.3.12). Figure 4.17b shows that there is some systematic deviation between these relations and the curve recalculated from the results of Vomela and Whitby. The values of k_1 and $k_2\sqrt{C''_n}$ corresponding with the relations (4.3.6) and (4.3.12) drawn in figure 4.17b are 2 and 2.3 respectively. These values are almost twice

the values resulting from the present study for the primary particle size of the aggregates studied by Vomela and Whitby (according to them: $d_{1g} = 0.039 \mu\text{m}$; $\sigma_{1g} = 1.3$, consequently $\bar{d}_1 = 0.04 \mu\text{m}$). This discrepancy can most probably be ascribed to experimental errors. For instance, the geometric standard deviation reported by them seems to be too small in the light of the values found by us.

4.4.5. Discussion of errors

In conclusion of this discussion the possible errors in the experimental results of the present study will be summarized.

The standard deviations in the values of k_1 , f_1 , $k_2\sqrt{C_n^I}$, and $f_2\sqrt{C_n^II}$, resulting from the scatter in the measuring results, are about 5%.

The values of k_1 and $k_2\sqrt{C_n^I}$ might be somewhat erroneous due to possible errors in the primary particle size distribution measurements. These errors will be mainly of a systematic nature. Such a systematic error might result from the uncertainty in the lattice spacing of the catalase crystals of about 4% (cf. section 4.2.2), leading to an identical uncertainty in the d_{1g} values reported. Furthermore the results of the primary particle size distribution measurements will be biased somewhat towards large diameters, due to the fact that particles being covered by larger ones, will not have been measured. This feature will result in geometric standard deviations being slightly too small, while it will have the opposite influence on the geometric mean diameters being measured. Although an exact value cannot be given, possible systematic errors in the values of k_1 and $k_2\sqrt{C_n^I}$ due to systematic errors in the primary particle size distribution measurements, surely will be not greater than about 5%. As discussed in appendix I.3, aerodynamic diameter classification of non-spherical particles by means of an aerosol centrifuge does involve systematic errors, if the fluid drag on the particles depends on their orientation, and furthermore they adopt a preferred orientation during settling in the centrifuge different from the orientation in their practical situation. With respect to this feature distinction has to be made between the linear aggregates and the threedimensional networks. It is rather unlikely that the fluid drag on the irregularly shaped threedimensional networks depends on their orientation, moreover electron microscope pictures do not indicate any preferred orientation of such aggregates sampled by the centrifuge. Therefore, the aerodynamic diameter

classification of the threedimensional networks will not have been affected by a systematic error of this kind. Thus the values of f_1 and $f_2 \sqrt{C_n^{(1)}}$ will not include systematic errors resulting from this aspect.

The fluid drag on the linear aggregates, however, very probably will depend on their orientation. Electron microscope pictures of deposits of such linearly shaped aggregates sampled by the centrifuge (cf. figure 4.10), do not give a definite answer about a possible preferred orientation of the aggregates. However, there seems to be some tendency of the aggregates to deposit in the centrifuge with their axes perpendicular to the settling direction. Therefore, because normally the aggregates will be randomly oriented due to Brownian rotation, the aerodynamic diameter classification of these linear aggregates might involve some systematic error. In order to obtain some idea about the magnitude of this possible error, this aspect will be considered for prolate spheroids.

From equations (2.2.5) and (2.2.10) it can be seen that the dynamic shape factor of a prolate spheroid settling with its polar axes perpendicular to the settling direction is maximally 20% larger than it is on the average for randomly oriented prolate spheroids. These figures, however, deal with the continuum flow region. In the Knudsen region, also a possible orientation dependency of the slip correction factor must be considered. A guideline in assessing the magnitude of this effect, might be the calculations of approximate slip correction factors of prolate spheroids at different orientations, carried out by Dahneke [17], by means of the "adjusted sphere" method. According to his results, the slip correction factor of a spheroidal needle, settling with its axis perpendicular to the settling direction, is about 20% smaller than it is on the average for randomly oriented spheroidal needles for the region of Kn considered here. Thus according to equation (2.2.14), the dynamic shape factor of a prolate spheroid settling with its polar axes perpendicular to the settling direction might be up to about 40% larger than the dynamic shape factor of a prolate spheroid undergoing random change of orientation. The resulting aerodynamic diameter will then be about 20% smaller (cf. eq. 2.2.21). The linearly shaped aggregates being studied, are far from perfectly linear, and therefore the dependence of the aerodynamic diameter on their orientation will surely be less than in the case of prolate spheroids. Furthermore the preferred orientation of these aggregates in the centrifuge, is far from predominant. Therefore it can be concluded that the possible systematic error in the aerodynamic diameter classification of

the linearly shaped aggregates will be less than say -10%.

All other uncertainties, such as the uncertainty in the exact chemical composition of the iron oxide particles (cf. section 4.2.1), have minor influences on the ultimate results. Therefore it can be concluded that the factors k_1 and f_1 of equations (4.3.6) and (4.3.7) as well as the factors $k_2\sqrt{C_n^r}$ and $f_2\sqrt{C_n^{rr}}$ of equations (4.3.12) and (4.3.13) as given in table 4.1 have standard deviations of about 5%. Furthermore, the values of k_1 and $k_2\sqrt{C_n^r}$ might include a systematic error within +5% and -15%, due to possible systematic errors in the primary particle size distribution measurements and the aerodynamic diameter classification of the linearly shaped aggregates.

4.5. Concluding remarks

In the present study two models have been obtained, describing the relation between the aerodynamic diameter and the microstructure (primary particle size distribution and number of primary particles) of branched chain-like aggregates. However, it must be recognised that the models were obtained for aggregates not exposed to extreme conditions such as high relative humidities or reactive gases. Such conditions may significantly influence the shape of the aggregates. Megaw and Wiffen [62] have observed that fluffy branched chain-like chromium aggregates rapidly change into compact aggregates when exposed to high humidities. Ranada et al. [82] have found that coagulation of PbCl particles results in chain-like aggregates at humidities lower than 70%, while at higher humidities compact aggregates are formed. In the present study compact agglomeration was observed when an exploding wire aerosol was generated in a 100% humidity atmosphere. Concerning the influence of reactive gases on aggregate structures, Pouw et al. [77] have observed that nitrogen oxides (concentration in the order of several ppm) influence the structure of exploding wire aggregates.

This indicates that future studies dealing with the influence of humidity and reactive gases on the aerodynamic diameter of branched chain-like aggregates will be of interest.

5. THE SPECIFIC SURFACE AREA OF BRANCHED CHAIN - LIKE AGGREGATES

5.1. Introduction

Originally, interest in the specific surface area (area per unit mass) of aerosol particles was a result of a train of thought according to which the harmfulness of inhaled particles would be increased when harmful gases or vapours are adsorbed at the particle surface [23]. The amount of gas or vapour being adsorbed by inhaled particles will be very small compared to the amount inhaled in the gaseous or vapour phase. Therefore nowadays the idea of increased hazard of respirable particles because of their capacity to adsorb dangerous gases and vapours has become questionable. However, more and more it is recognised that aerosol particles may play an important role in atmospheric chemistry. Therefore from this point of view, the specific surface area of aerosol particles remains of interest.

The study reported in this chapter deals with an evaluation of the specific surface area of branched chain-like iron oxide aggregates. For this purpose an experimental method for the measurement of surface area has to be chosen. The important role powders play in technology (e.g. most catalysts are powders) and the resulting interest in their specific surface areas led to the development of many experimental techniques. For a detailed discussion of these techniques, which lies beyond the scope of this thesis, the works of Orr and Dalla Valle [72], and Gregg and Sing [30] should be consulted.

The methods were judged with respect to their applicability to aerosols. Because usually the amount of aerosol which can be collected is relatively small, the quantity of material needed in the different methods was considered critically. Furthermore the demands put on the particle sizes and shapes by the different methods was considered. This led to the choice of a surface area measuring technique based on physical adsorption of gases, the so-called BET method. In section (5.2.1) this method is discussed in detail.

5.2. Materials and methods

5.2.1. Specific surface area from gas adsorption

When a solid is exposed to a gas or vapour, the solid will adsorb gas or vapour molecules. The interaction forces between the solid and the adsorbed molecules may be of physical or chemical nature, called physical adsorption and chemisorption respectively. Surface area measurements by means of gas adsorption are mainly based on physical adsorption. Brunauer, Emmett and Teller (B.E.T.) [6] have grouped physical adsorption isotherms into five classes. These five types are shown in figure 5.1. Although isotherms have been measured which do not fit any of these five types, the majority of the adsorption isotherms reported in literature are represented by one of the B.E.T. curves.

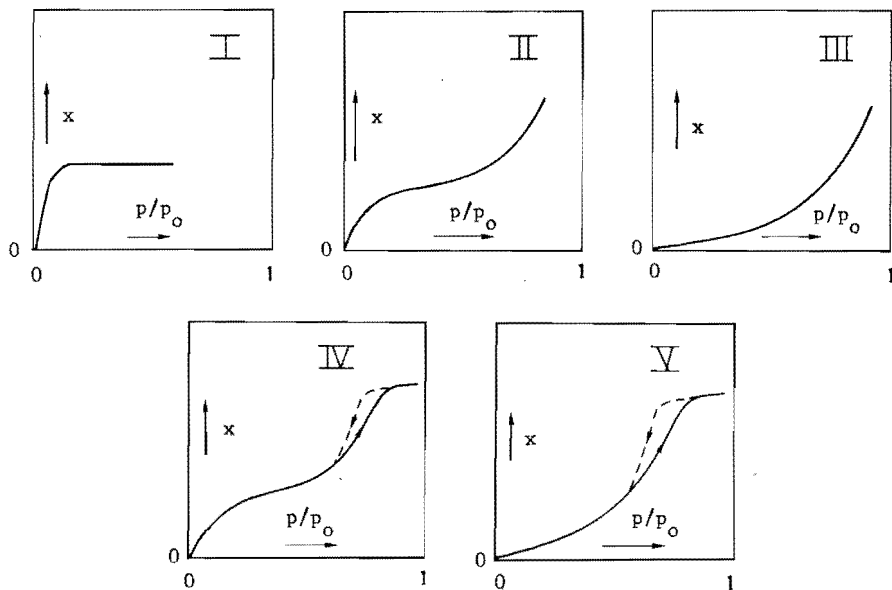


Figure 5.1. Adsorption isotherm classification according to Brunauer, Emmett, and Teller [6]. x = adsorbed volume; p = pressure; p_0 = saturation pressure.

Surface evaluation by means of gas adsorption requires that the adsorption theory provides a mathematical expression from which the surface area can be evaluated. However, a fundamental difficulty is, that any theory which

is mathematically manageable has to be based on over-simplified models of the adsorption phenomenon.

In the following the five B.E.T. isotherms will be discussed.

- Type I isotherms correspond with physical adsorption on microporous solids (pores of width below about 2 nm). The main part of the surface of such microporous solids consists of the surface of the micropores. In these micropores capillary condensation takes place. Therefore the amount of adsorbed gas rapidly increases with increasing pressure until the pores are filled.

Up to now one has not succeeded to treat this adsorption mechanism mathematically in a way allowing the evaluation of the surface area of the solid.

The classical but unsatisfactory interpretation of type I isotherm is the one given by Langmuir [55]. He derived the mathematical expression:

$$\frac{p}{x} = \frac{1}{x_m b} + \frac{p}{x_m} \quad (5.2.1)$$

where, p = gas pressure,
 x = adsorbed volume of gas per unit mass of solid,
 x_m = volume of a monomolecular layer per unit mass of solid,
 b = constant.

If x_m is expressed as a volume at standard temperature (T_s) and pressure (P_s), it is related to the specific surface (S) of the solid according to:

$$S = \frac{x_m \cdot A_m \cdot P_s}{k T_s} \quad (5.2.2)$$

where, k = the Boltzmann constant,
 A_m = area occupied per molecule of adsorbate.

Langmuir obtained equation (5.2.1) by considering the surface as an array of adsorption sites, each site being capable to adsorb one molecule. Furthermore he assumed that every molecule striking an empty adsorption site is adsorbed and reevaporates again after some time of sojourn. These assumptions do not hold for the mechanism of capillary condensation. Therefore application of the Langmuir theory to the adsorption on microporous solids, and thus calculation of the specific surface area from equations (5.2.1) and (5.2.2), may give rise to considerable errors.

- Types II and III isotherms correspond with physical adsorption on non-porous solids, e.g. solid walls. Brunauer, Emmett and Teller [6] assumed an adsorption model from which a mathematical expression (B.E.T. equation) could be evaluated, corresponding with types II and III isotherms. This B.E.T. equation is:

$$\frac{p}{x(p_0 - p)} = \frac{1}{x_m c} + \frac{c-1}{x_m c} \cdot \frac{p}{p_0} \quad (5.2.3)$$

where, p_0 = saturation pressure,
 $c = \exp [(E_a - E_L)/RT]$,
 E_a = molar energy of adsorption of molecules in the first layer,
 E_L = molar energy of liquefaction,
 R = gas constant,
 T = temperature [K].

For large values of c a plot of x/x_m versus p/p_0 according to equation (5.2.3) results in a type II isotherm, while for c -values of order 1 ($E_a - E_L \approx 0$) an isotherm of type III is obtained.

The B.E.T.-equation is based on the following main assumptions

- (i) there are no preferent adsorption sites (as in the Langmuir theory)
- (ii) energy of adsorption of molecules in the first layer, E_a , depends on adsorbent-adsorber pair
- (iii) energy of adsorption of molecules in 2nd, 3rd, etc. layers is equal to energy of liquefaction, E_L .
- (iiii) there is no interaction between neighbouring molecules in the same layer.

The B.E.T. theory has been strongly criticized with respect to these assumptions. Nevertheless, experimentally obtained adsorption isotherms of type II fairly well agree with the B.E.T. equation for relative pressures (p/p_0) between 0.05 and 0.35 [6].

Experimentally obtained type III isotherms show a far less satisfactory agreement with the B.E.T. equation.

Consequently, type II isotherms are considered to be very suitable for specific surface area evaluation by means of the B.E.T. equation, in contrast to type III isotherms.

- Types IV and V isotherms correspond with physical adsorption on porous solids containing no micropores. The first parts of these isotherms follow types II and III isotherms respectively and therefore they also correspond with the B.E.T. equation respectively for large c -values (type IV) and for c -values of order 1 (type V). The pores have a limited adsorption capacity. Therefore types IV and V isotherms exhibit saturation when the pores are filled (cf. figures 5.1).

As in the case of type II, experimentally obtained type IV isotherms fairly well satisfy the B.E.T. equation for relative pressures between 0.05 and 0.35. The agreement between experimentally obtained type V isotherms and the B.E.T. equation is most times less satisfactory. Consequently type IV isotherms are suitable for surface area evaluation by means of the B.E.T. equation, while type V isotherms are not.

As is shown in figure 5.1, isotherms of types IV and V have hysteresis loops, one branch of which corresponds with adsorption while the other branch represents desorption. The reason for this is that the desorption mechanism is not governed by the normal adsorption-desorption process, but must be seen as the evaporation of a liquid from filled pores. The adsorbed gas starts to evaporate from the filled pores as soon as the equilibrium pressure in the system has fallen to a critical pressure, p_c . Assuming cylindrical pores, p_c is given by the Kelvin equation:

$$\ln\left(\frac{p_c}{p_0}\right) = -\left(\frac{2\gamma V}{rRT}\right) \cos \phi_c \quad (5.2.4)$$

where, γ = surface tension of the adsorbent in the liquid phase,
 V = molar volume of the adsorbent,
 r = radius of the pore,
 ϕ_c = contact angle between adsorbent and adsorber.

Herewith it is illustrated that from these hysteresis loops the pore sizes may be evaluated. Indeed, practice has shown that the type IV isotherm allows reliable pore size evaluations. However, it is believed that uncertainties in the interpretation of the type V isotherm are such as to preclude its use for this purpose [30].

Summarizing the discussion given above, it can be stated that specific surface areas can be reliably evaluated by means of physical adsorption, provided that the isotherms are of types II or IV, while furthermore type IV isotherms allow reliable evaluations of pore sizes.

Most physical adsorption measurements used for specific surface evaluations deal with the adsorption of nitrogen at 77.8 K. This method generally is accepted as a standard method for specific surface area evaluation. However, numerous other adsorbents are used from time to time, e.g. benzene, toluene, nitrous oxide, water, krypton etc. [30]. More and more the adsorption of Kr at 77.8 K is used for specific surface area evaluations. The advantage of the use of Kr is its low vapour pressure at 77.8 K, due to which the ratio between unadsorbed and adsorbed molecules is reduced. Consequently the amount of solid surface area needed is reduced, e.g. successful surface area measurements by means of Kr adsorption down to surface areas of 100 cm^2 have been reported [2]. Another advantage is that Kr can be radioactively labeled with ^{85}Kr , which allows replacement of the conventional pressure measurements by radioactivity measurements. Disadvantages of the use of Kr are uncertainties about the values of p_0 as well as A_m . The uncertainty in the value of p_0 stems from the fact that 77.8 K is well below the triple point of Kr (116 K). It might seem logical therefore to take p_0 as the saturation pressure of solid Kr at 77.8 K. Doing this however, an isotherm is obtained with an unusually sharp change of slope at the large pressure side. Therefore Beebe and coworkers [4] proposed to take p_0 as the saturation pressure of supercooled liquid Kr at 77.8 K, which proposal has been followed by most other investigators. Concerning the A_m value, in literature values ranging from 0.177 nm^2 to 0.236 nm^2 have been proposed [4,22,35,85]. The advice of Beebe ($A_m = 0.195 \text{ nm}^2$), which results from careful comparisons of Kr and nitrogen adsorption data, has been most widely followed [2,12]. In spite of the uncertainties in the values of p_0 and A_m , in the present study Kr-adsorption at 77.8 K is employed, because this is most promising for application to aerosols on account of the amount of adsorber material needed.

5.2.2. *Experimental procedure*

In figure 5.2 the adsorption apparatus is shown schematically. The measuring part is located on the left hand side from stopcock 1. On the right hand side from stopcock 1, a pumping system as well as a krypton storage vessel are located. The krypton is labeled with ^{85}Kr , in order to allow pressure evaluations by means of radioactivity measurements. These radioactivity measurements are carried out by means of a Geiger-Müller tube.

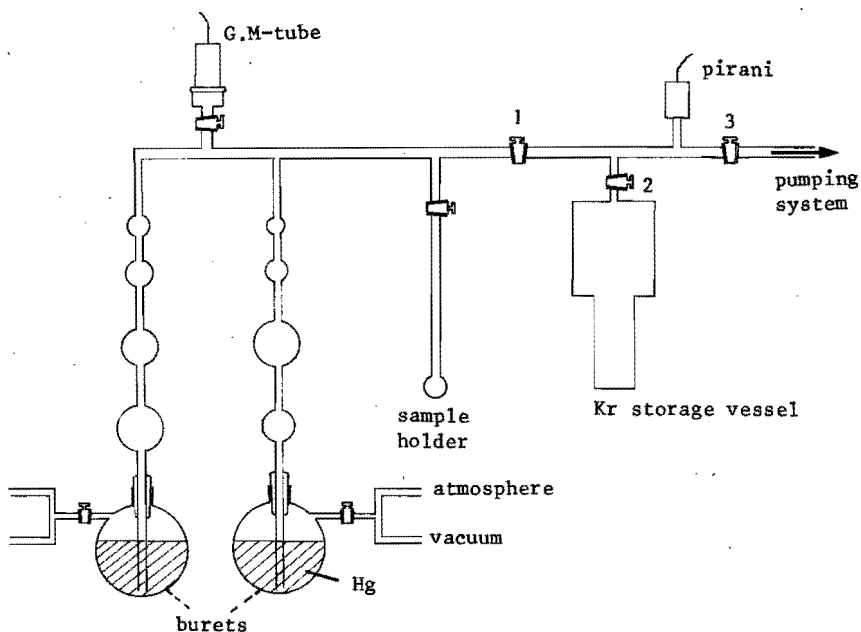


Figure 5.2. Schematic drawing of the adsorption apparatus.

The krypton is introduced in the measuring part of the adsorption apparatus through stopcocks 1 and 2 (evidently with stopcock 3 closed). During the introduction of the krypton, the storage vessel is kept at 77.8 K by immersing it in boiling liquid nitrogen. Therefore the Kr-pressure rises up to 273 Pa. Hence, the total amount of Kr introduced depends on the volume of the measuring part. This volume can be varied by means of two mercury burets. The volume of these burets can be varied between 0 cm^3 and 210 cm^3 . The volume of the measuring part apart from the burets is called the dead space volume. The dead space volume (70 cm^3) could be evaluated from the pressure variations resulting from known variations of the volume by means of the burets. When the introduction of krypton is completed, stopcock 1 is closed. The adsorption is started by decreasing the temperature of the adsorber down to 77.8 K, by immersing the sample holder in boiling liquid nitrogen. A result of the adsorption is a decrease of the Kr-pressure down to the equilibrium pressure (p), which is recorded by means of the Geiger-Müller tube. The amount of krypton adsorbed by the adsorber evidently is equal to the amount

of krypton introduced minus the amount of krypton in the gas phase at the equilibrium state. The latter is calculated from the equilibrium pressure (p) and the volume of the measuring part during the adsorption measurement, taking into account that a part of the volume is at 77.8 K (viz. the sample holder). The correction needed for the lower temperature of the sample holder, can easily be obtained from the relations between volume (to be varied by means of the burets) and pressure for the cases that the sample holder (without absorber) is immersed as well as not immersed in boiling liquid nitrogen.

In the way described above one point of the adsorption isotherm is obtained. Other points are obtained by varying the volume by means of the burets and allowing the Kr to adsorb further or to desorb (depending on whether the volume is increased or decreased) until a new equilibrium state is obtained.

Because the adsorption measurements will have to be used for specific surface area evaluations by means of the B.E.T. equation, the amount of krypton introduced in the measuring part has to be such that adsorption data in the relative pressure range between 0.05 and 0.35 can be obtained.

Prior to the adsorption measurements, the adsorbents have to be outgassed thoroughly, which is done by simultaneously increasing the temperature and evacuation. The outgassing temperature cannot be raised above a certain limit, in order to prevent changes of the chemical or physical nature of the sample. In the present study, dealing with Fe_2O_3 aggregates, on somewhat arbitrary grounds an outgassing temperature of 300°C was chosen. Outgassing times of more than 24 hours were taken. No chemical or physical changes of the iron oxide, due to the outgassing procedure, could be observed by means of X-ray diffraction.

The mass of the iron oxide samples was determined afterwards by means of the spectrophotometric O-phenanthroline method [107].

5.3. Results and discussion

As mentioned in section (5.2.1), surface area evaluation from gas adsorption isotherms requires that these isotherms are of type II or type IV according to the B.E.T. classification (cf. figure 5.1). Figure 5.3 shows an isotherm obtained for Kr adsorption by branched chain-like iron oxide aggregates at 77.8 K. The isotherm is of type II, which indicates the

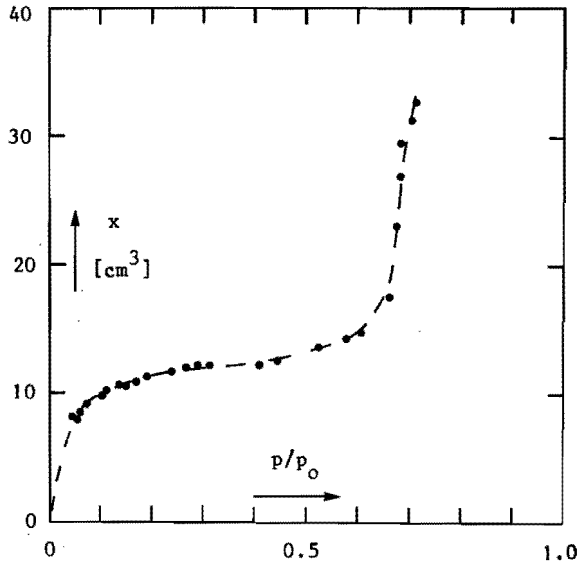


Figure 5.3. Adsorption isotherm obtained for the adsorption of Kr at 77.8 K by branched chain-like iron oxide aggregates, having a primary particle size distribution given by:
 $d_{lg} = 0.019 \mu\text{m}$ and $\sigma_{lg} = 1.66$.

applicability of Kr adsorption for specific surface area evaluations in the present study.

Plots of $p/(p_0 - p)x$ versus p/p_0 *) are shown in figure 5.4. In agreement with the B.E.T.-equation (5.2.3), these plots are straight lines in the region: $0.05 \lesssim p/p_0 \lesssim 0.30$. According to the B.E.T.-equation the reciprocal of the monolayer capacity per unit mass of adsorber (x_m^{-1}) is equal to the slope of these plots plus the intercept at the $p/(p_0 - p)x$ -axis. From the monolayer capacity the specific surface area is calculated by means of equation (5.2.2). The A_m value is taken as 0.195 nm^2 as is advised by Beebe and coworkers [4]. The results of the calculations are given in table 5.1. The surface area evaluations were reproducible within 5%. Comparison of the B.E.T. results (S_{BET}) with the specific surface areas calculated from the primary particle size distributions (S_{geom}), obtained

*) According to the advise of Beebe [4], p_0 is chosen as 385 Pa, being the saturation pressure of supercooled liquid krypton at 77.8 K.

Tabel 5.1. Specific surface areas of branched chain-like iron oxide aggregates obtained from their geometric dimensions as well as Kr adsorption isotherms at 77.8 K by means of the BET theory.

Geometric dimensions			Original BET results		Adsorption data corrected so that c=75			Adsorption data corrected so that c=30		
d_{lg} [μm]	σ_{lg}	$^+ S_{\text{geom}}$ [$\text{m}^2 \cdot \text{g}^{-1}$]	S_{BET} [$\text{m}^2 \cdot \text{g}^{-1}$]	r	S'_{BET} [$\text{m}^2 \cdot \text{g}^{-1}$]	$^{++} r'$	Δx [cm^3]	S''_{BET} [$\text{m}^2 \cdot \text{g}^{-1}$]	$^{+++} r''$	Δx [cm^3]
0.019	1.66	31.7	49.3	1.56	31.5	0.99	5.0	26.7	0.84	6.0
0.024	1.67	24.7	39.5	1.60	23.0	0.92	4.5	20.4	0.82	5.5
0.042	1.63	15.0	25.0	1.67	11.6	0.77	3.6	9.5	0.63	4.2
0.047	1.70	12.1	19.7	1.63	16.2	1.34	1.0	12.6	1.04	2.0

$^+ S_{\text{geom}} = 6 \cdot \{\rho \cdot d_{lg} \exp[2.5 \ln^2 \sigma_{lg}]\}^{-1}$; $^{++} r' = S'_{\text{BET}}/S_{\text{geom}}$; $^{+++} r'' = S''_{\text{BET}}/S_{\text{geom}}$

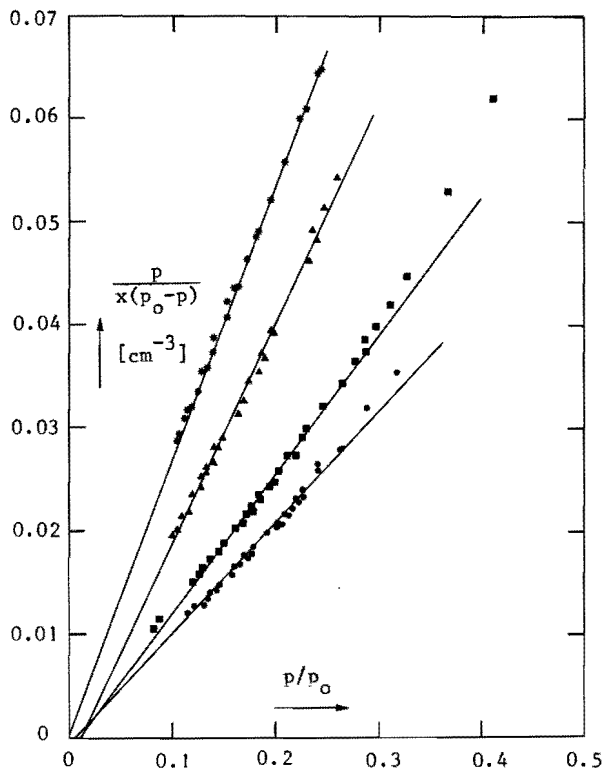


Figure 5.4. Adsorption isotherms obtained for branched chain-like iron oxide aggregates. Primary particle size distributions;
 ●: $d_{1g} = 0.019 \mu\text{m}$; $\sigma_{1g} = 1.66$; ■: $d_{1g} = 0.024 \mu\text{m}$; $\sigma_{1g} = 1.67$;
 ▲: $d_{1g} = 0.042 \mu\text{m}$; $\sigma_{1g} = 1.63$; *: $d_{1g} = 0.047 \mu\text{m}$; $\sigma_{1g} = 1.70$.

as reported in the previous chapter, show significant differences. The ratios of S_{BET} and S_{geom} , so-called roughness factors (r), cluster around 1.6, which is rather high. Furthermore it must be noticed that the plots given in figure 5.4, all except one, have negative intercepts at the $p/(p_0 - p)$ -axis, which results in negative values of c (cf. equation 5.2.3). Although, on account of the simplifications in the B.E.T. model, the relation between c and the heat of adsorption surely is not as significant as given in the original B.E.T. theory (cf. section 5.2.1), the value of c has to be positive.

The reason for these negative intercepts at the $p/(p_0 - p)$ -axis as well as the high roughness factors might be the feature that the adsorption iso-

therms are not purely of type II, but a combination of types II and I. The type I part might result from capillary condensation in a small area around the interfaces between the particles. This capillary condensation very likely will have been completed at the relative pressures, the adsorption data of the present study were obtained for $(p/p_0 \gtrsim 0.1)$. Therefore from the isotherms the type II part can be deduced by subtracting from the x -values the amount of Kr (Δx) being adsorbed according to the capillary condensation mechanism. However, the magnitude of Δx is not known. The best that can be done is to choose Δx such that the corrected isotherms correspond with c -values in agreement with those known for Kr-adsorption by iron oxide. Unfortunately, however, the values reported in

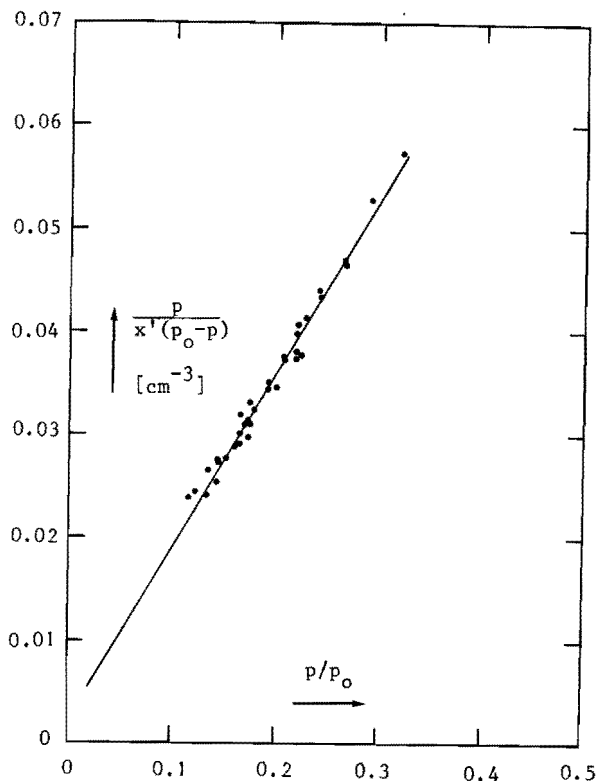


Figure 5.5. Isotherm with $c = 75$, deduced from the original isotherm obtained for the aggregates having a primary particle size distribution given by: $d_{lg} = 0.019 \mu\text{m}$, and $\sigma_{lg} = 1.66$. $x' = x - \Delta x$ with $\Delta x = 5 \text{ cm}^3$.

literature show a significant scatter. Sing and Swallow [87] gave values of c for the adsorption of Kr by ferric oxide ranging from 30 up to 75. Calculations were carried out with Δx values chosen such that the corrected isotherms had a c value of 75 as well as 30. The results of these calculations are given in table 5.1. An isotherm calculated in this way is shown in figure 5.5. In agreement with the B.E.T. equation this plot yields a straight line with a positive intercept at the $p/(p_0-p)$ -axis.

The calculations described above cannot lead to very accurate results. Nevertheless these results give roughness factors significantly closer to unity than the original results, which seems to be more realistic.

5.4. Conclusion

No firm conclusions can be drawn from the experiments described above, because of the large uncertainties in the results. Nevertheless it seems to be reasonable to conclude that the primary particles are smooth, because otherwise significant larger roughness factors would have been found. The most important conclusion, however, can be that it is clearly illustrated that surface area evaluations of aerosols by means of gas adsorption cannot be considered as routine experiments, because it demands careful analysis of the adsorption isotherms.

APPENDIX I. METHODS FOR MEASURING THE AERODYNAMIC DIAMETER

I.1. Introduction

Experimental methods for measuring the aerodynamic diameter of arbitrarily shaped particles with unknown density are based on comparing their settling rates with those of unit density spheres. A classification of these methods can be made according to the forces causing the settling of the particles, viz.:

- gravity (Millikan chambers and elutriators)
- centrifugal forces (centrifuges)
- inertia forces (impactors)

In some special cases, the aerodynamic diameter of a particle can be evaluated from its settling rate under the influence of an electric field. Electric mobility analysers are based on this principle.

In all these methods distinction can be made between classifying and non-classifying instruments. With a classifying instrument the aerodynamic diameter of individual particles can be determined, in contrast to a non-classifying instrument which only allows the determination of the aerodynamic diameter distribution.

It is not the aim of this appendix to give a comprehensive discussion of the working principles and the theoretical background of these methods. They are described briefly, and attention is paid to their advantages and disadvantages, especially with respect to the requirements an instrument should satisfy to be used for measurement of aerodynamic diameters in the present study. These requirements are that the particles can be classified accurately according to their aerodynamic diameter, while furthermore it must be possible to obtain information about the structure of these particles as a function of their aerodynamic diameter. Because the present study is limited to aggregates with aerodynamic diameters smaller than about 2 μm (respirable fraction) the above given requirements only have to be fulfilled in this aerodynamic diameter region.

1.2. Methods

1.2.1. Electric mobility spectrometers

The electric mobility (Z_p) of a particle is defined as the ratio of the final velocity of the particle, caused by a homogeneous electric field, and the strength of this electric field. Therefore one has:

$$Z_p = \frac{qC_s(d_e)}{3\pi\eta d_e \kappa} \quad (1.2.1)$$

where q is the electric charge of the particle.

The electric mobility of a particle can be determined by measuring its final velocity in an electric field of known strength. For particles of known density, charge and volume (d_e) the aerodynamic diameter can be calculated from their electric mobility using formulae (1.2.1) and (2.2.21).

Electric mobility analysers originally used were non-classifying instruments. They were based on the principle shown in figure I.1. The system consists of two parallel capacitor plates, one of which is kept at a tension (U), which can be varied, while the other is connected to

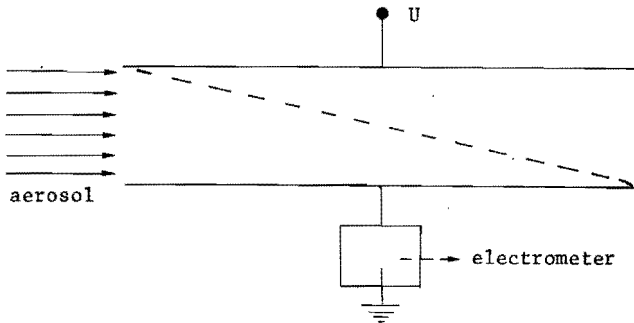


Figure I.1. Non-classifying electric mobility analyser.

an electrometer. The aerosol is introduced over the whole width between the plates. The electric mobility spectrum of the aerosol can be determined from the relation between U and the electrometer current [43].

An electric mobility analyser has been designed by Megaw and Wells [65] according to the principle shown in figure I.2. The apparatus consists of two parallel plates with opposite tension. The aerosol is injected in

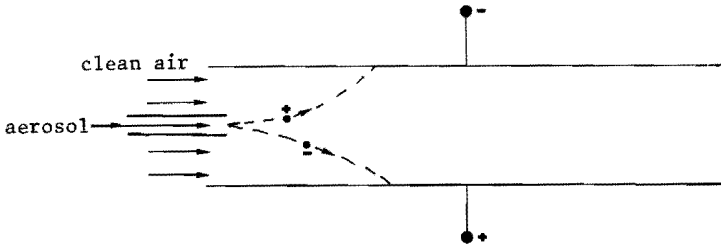


Figure I.2. Principle of the electric mobility analyser according to Megaw and Wells [63].

a clean air flow through a narrow slot midway between the plates. With this device the charge of arbitrarily shaped particles cannot be determined. Therefore from the electric mobility classification no information about the fluid drag can be obtained except in some special cases, for instance when it is certain that all particles have the same charge. Nevertheless the instrument can be very useful in fundamental aerosol studies, e.g. studies of the orientation of particles in an electric field [5].

A particle size classifier based on electric mobility classification has been described by Whitby and Clark [110]. Their system, which is shown schematically in figure I.3, consists of a charging device followed by an electric mobility analyser.

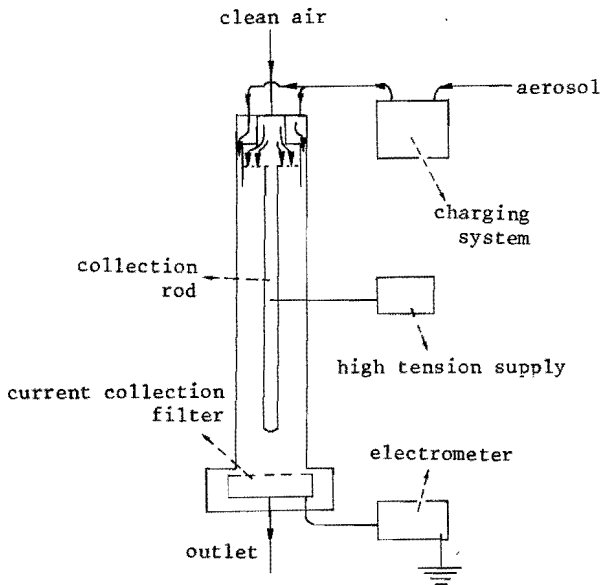


Figure I.3. Particle classifying system according to Whitby and Clark [110].

In the charging system the particles are charged by being exposed to small unipolar ions. The charge of the particles is related to their size, which relation will depend on the ion concentration, exposure time and the shape of the particles. The electric mobility classifier consists of a cylinder with a central collection rod which is kept at a high tension, followed by a current filter. The aerosol is introduced along the inner wall of the cylinder separated from the collection rod by a clean air flow.

The instrument can be operated in two modes. In the first one, the classifying mode, the collection rod is at a high constant tension. The particles move towards the rod with a velocity depending on their electric mobility. Therefore they are deposited on the rod separated according to their electric mobility. Particles having an electric mobility too small to be collected on the rod are captured by a current filter. The resulting current is monitored by an electrometer.

In the second mode of operation, the counting mode, the collection rod tension is varied in a stepwise manner. The number of particles escaping collection by the rod and therefore the filter current depends on the tension of the rod. From the relation between these two quantities the electric mobility spectrum of the aerosol can be calculated, provided that the relation between the electric mobility of the particles and their charge is known. If required this relation can be evaluated from the results of the first and second mode operation.

However, an electric mobility classifier classifies particles according to their aerodynamic diameters only when the electric mobility of the particles is a continuously decreasing or increasing function of their aerodynamic diameter. Formula (I.2.1) shows that the electric mobility of a particle besides being dependent on the aerodynamic properties of the particle is also dependent on its charge. Hence the classifier of Whitby and Clark classifies particles according to their aerodynamic diameters only when the charge the particles attain in the charging system depends upon their aerodynamic diameters in such a way that the electric mobility of the particles is a continuously decreasing or increasing function of their aerodynamic diameters. Whitby and Clark have shown that in their system spherical particles with diameters between $0.015 \mu\text{m}$ and $3 \mu\text{m}$ attain an electric mobility which is continuously decreasing with increasing particle diameter. So, in that size range the system separates spherical particles according to their size, although

irrespective of their density. However, for non-spherical particles a lot of difficulties arise, and only in very special cases the above mentioned requirements will be fulfilled. Nevertheless the system described above has been used by Vomela and Whitby [108] in a study on the fluid drag on branched chain-like aggregates, which is also the subject of the present study. Undoubtedly the above given requirements for the relation between the charge and the aerodynamic properties of the particles will not be fulfilled entirely by chain-like aggregates, so there will be some error in the results by Vomela and Whitby, which are discussed in section 4.4.4.

It may be concluded that the Witby and Clark classifier is a useful aerosol classifier for spherical particles of known density having diameters between 0.015 μm and 1 μm . The high sampling rate (up to 80 l/min) of this classifier is certainly an advantage in studying atmospheric aerosols. With respect to the classification of non-spherical particles the applicability of the apparatus is limited to very special cases.

1.2.2. Millikan chambers and elutriators

In this subsection, instruments are discussed by which aerodynamic diameters can be determined from the settling of the particles under the influence of gravity. Also a brief discussion is devoted to Millikan chambers, which are instruments in which apart from the gravitational field other forces, e.g. electrical or thermophoretic forces can be applied to enhance or retard the settling of the particle.

A. Millikan chambers

A Millikan chamber is a small aerosol chamber in which floating particles are made visible for optical microscopic observation by light scattering from lateral illumination. The experimental procedure is to select a single particle for observation. In that way the settling rate of the particle can be measured, which allows the calculation of its aerodynamic diameter.

Dependent on the type of Millikan chamber the settling of the particles under the influence of gravity, can be enhanced or counteracted by both electrical and thermophoretic forces. These forces are caused by a difference in respectively tension and temperature between the upper and lower wall of the chamber.

Millikan chambers can be constructed such that experiments can be performed at different gas pressures.

Because of the possibility to observe floating particles at different gas pressures, under the influence of gravitational, electrical or thermophoretic forces, Millikan chambers are very useful instruments. For instance they have been used successfully in experimental studies on thermophoresis [109,113], Brownian motion of particles [109] and slip correction factors [66]. However, concerning aerodynamic diameter measurements the applicability of these instruments is limited due to the Brownian motion of the particles, which causes measurements of aerodynamic diameters smaller than $1.0 \mu\text{m}$ to be inaccurate. Another disadvantage of Millikan chambers is that the experiments are very cumbersome and time consuming. Besides these disadvantages, the main reason rendering a Millikan chamber unsuitable for the objectives of this study is the fact that particles are not available for inspection of their microstructure after their aerodynamic diameters have been measured.

B. Elutriators

Elutriators are instruments which separate particles according to their aerodynamic diameters due to the different settling rates of the particles under the influence of gravity. Vertical and horizontal elutriators must be distinguished. In a vertical elutriator the particles are carried upwards in a diverging air stream up to the level at which the air velocity equals the settling velocity of the particles. By optical observation the level at which particles remain floating can be determined. The aerodynamic diameter of the particles can be calculated from the air velocity corresponding to that level. Vertical elutriators can be used successfully for size separation of coarse particles (powders). However for small particles ($d_a < 10 \mu\text{m}$) these instruments are unsuitable.

In a horizontal elutriator particles settle perpendicular to an air stream. Horizontal elutriators with circular cross sections [102], rectangular cross sections [88], as well as diverging cross sections [105] have been developed.

The most promising elutriation classifier has been developed by Timbrell [105]. This device is shown in figure I.4. The aerosol can be drawn into the elutriator in two ways. The normal way of operation is with valve 3 closed and valve 2 open, so that clean air is extracted by an aspirator.

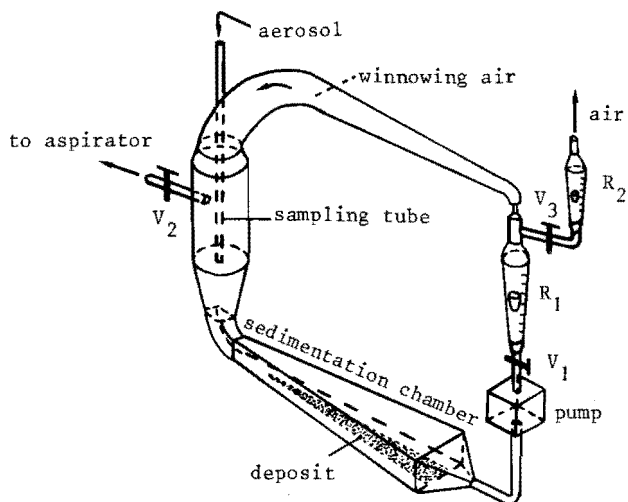


Figure I.4. Horizontal elutriator according to Timbrell [105].

The alternative way of operation is with valve 2 closed and valve 3 open. In that case air will leak out of the system at a rate that is adjusted by valve 3 and measured by flowmeter 2. In both cases, the air leaving the system will be replaced by aerosol at a rate of about $1 \text{ cm}^3/\text{min}$. This aerosol flow is rather low in comparison to other samplers. The particles are carried along with the air flow, and simultaneously they settle with a velocity determined by their aerodynamic diameters. Therefore the particles are deposited at a distance from the deposition chamber entrance, which is related to their aerodynamic diameters. Timbrell's calibration [105] gives a classification of aerosol particles in the aerodynamic diameter range from $25 \mu\text{m}$ down to $1.5 \mu\text{m}$. Timbrell claims that at other operation conditions classification down to $0.8 \mu\text{m}$ is possible. Due to the low settling velocity and the rapid increase of Brownian motion in the submicron range, the accuracy will be poor in that region.

It may be concluded that an elutriator according to Timbrell is a useful aerosol classifier, but has the disadvantages of a low aerosol sampling rate ($1 \text{ cm}^3/\text{min}$) and a lower size limit ($d_a \approx 1 \mu\text{m}$) somewhat too high for hazard evaluation of atmospheric aerosols. This size limit also eliminates the Timbrell elutriator as an aerosol classifier for the purpose of this thesis.

I. 2. 3. Centrifuges

An obvious way to separate particles from the gas phase is to employ centrifugal forces. Therefore it is not surprising that several aerosol analysers have been developed which operate by centrifugal forces.

The first successful centrifugal aerosol classifier was developed by Sawyer and Walton [86], which instrument is shown schematically in figure I.5. It consists of a rotating solid cone to which a conical shell is fastened rigidly. The aerosol enters the annular space at the wall of the solid cone surrounded by clean air. The clean air flow rate depends on the rotor speed while the aerosol flow is equal to the flow which is withdrawn from the instrument (cf. figure I.5).

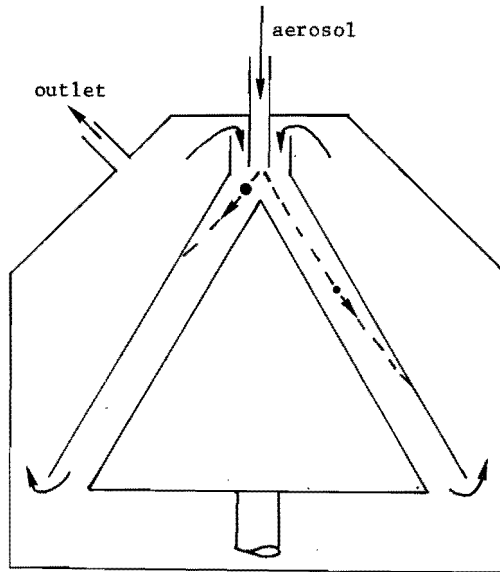


Figure I.5. Conifuge according to Sawyer and Walton [86].

The aerosol particles are carried down the annulus by the clean air. Simultaneously, due to the centrifugal force, they move towards the conical shell with a velocity depending on their aerodynamic diameter. As a result the particles are deposited on the outer cone separated according to their aerodynamic diameters.

The original conifuge of Sawyer and Walton successfully classifies

particles in the aerodynamic diameter range from about 0.5 μm up to 30 μm . Later modified versions have been developed [48,103] by which particles with aerodynamic diameters between 0.05 μm and 3 μm can be classified.

Goetz [29] developed a centrifugal aerosol spectrometer in which the aerosol is drawn through two helical ducts cut into a rotating aluminum cone. Particles with aerodynamic diameters down to 0.3 μm are deposited on a conical shell, closely fitting to the cone. Since at the entrance the particles are distributed over the entire cross section of the channel, no real aerodynamic diameter classification of the aerosol particles is achieved. Therefore this instrument is unsuitable for the present study. Even for indirect measurements of the aerodynamic diameter distributions the applicability of the Goetz spectrometer is limited due to practical problems in analysing the particle deposits [64].

The first aerosol centrifuge with a duct having a horizontal mid-plane was developed by Kast [47]. The duct of this centrifuge is an archimedian spiral. The instrument samples particles, with aerodynamic diameters down to 1 μm , on a collection foil, which covers the outer wall of the duct. Since, just as in the Goetz spectrometer, the particles enter the duct distributed over the whole cross section, the particles are not really separated according to their aerodynamic diameter.

Since the development of the Kast centrifuge, several centrifugal aerosol classifiers with circular [39,104] as well as spiral ducts [50,96] in a horizontal plane have been developed. The working principles of these centrifuges all are somewhat similar. Therefore, these principles are not described here, and the reader is referred to the detailed description of the Stöber centrifuge given in chapter 3 of this thesis.

Although these centrifugal classifiers are applicable for aerodynamic diameter characterisation of aerosol particles and hence would be very useful for hazard evaluation of atmospheric aerosols, up to now centrifugal classifiers have not been widely used for this purpose. Reasons for this are the high costs of centrifuges and the complicated operating conditions (an exception is the Hochrainer device [39], a small handy instrument which needs no cooling system or auxiliary apparatus such as pumps and filters). Another reason is the time consuming analysis of the centrifuge samples. Concerning the latter, a recent development on the Stöber centrifuge might improve its applicability for atmospheric aerosol classification. In this instrument vibrating quartz crystals have been

placed on the deposition strip [67]. The vibration frequency depends on the mass deposited. This allows an accurate mass evaluation.

For laboratory study purposes the spiral centrifuge according to Stöber and Flachsbart [96] has proved to be a very suitable instrument, and for that purpose it is the most widely used centrifugal classifier. The original calibration results of Stöber et al. [96] show a good size resolution in the aerodynamic diameter range from $4\ \mu\text{m}$ down to $0.08\ \mu\text{m}$. Recently Stöber [94] has developed a new smaller spiral centrifuge. This centrifuge separates particles having aerodynamic diameters from several microns down to about $0.3\ \mu\text{m}$. This instrument has the advantage that no cooling of the bearings is needed. However, the size resolution of the large Stöber centrifuge is superior to that of the small one. Concerning size resolution the large Stöber centrifuge is superior to all other centrifugal classifiers as well.

I.2.4. Impactors

Impactors are aerosol samplers which analogous to the centrifuges use the inertia of the particles to separate them from the gas phase. The separation principle is shown in figure I.6. Originally impactors were not used as aerosol classifiers but for sampling aerosol particles for optical microscope observation. The sampling efficiency and the minimum aerodynamic diameter of the particles being collected depend on the dimensions x and y (cf. figure I.6) and the flow velocity. May [59] was

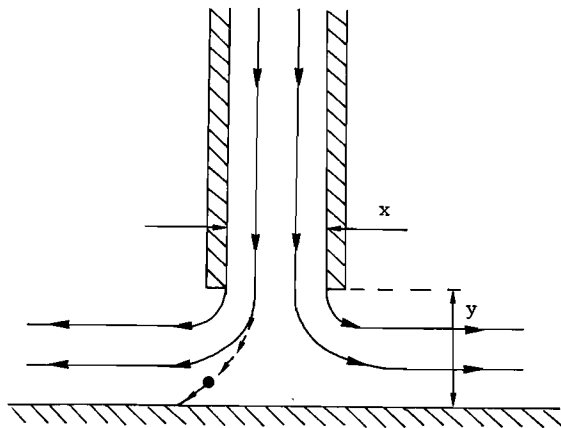


Figure I.6. Impact mechanism.

the first to use this impact mechanism in developing an instrument able to separate aerosol particles into aerodynamic size classes. This instrument shows a cascade of impactor stages, every following stage having dimensions such that smaller particles can be collected than in the previous stage. A schematic picture of May's device is shown in figure I.7. An improvement on May's design was made by Laskin [56], who added a final filter stage to collect the particles which escape impact. Since then several cascade impactors have been developed [1,58,65], and cascade impactors play a very important role in aerosol sampling technology.

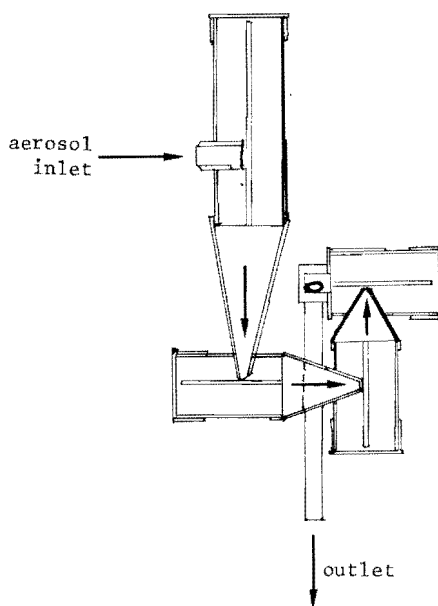


Figure I.7. Cascade impactor according to May [59].

A cascade impactor would be ideal if the collection efficiency of the stages would be 100% for particles with an aerodynamic diameter larger than a certain cut-off diameter (decreasing with increasing stage number), and zero for particles with smaller aerodynamic diameters. However, in practice this will not be the case and there will be an overlap between the stages. This feature complicates the deduction of aerodynamic diameter distributions from cascade impactor samples. The accuracy of the measured size distributions depends on the amount of overlap between the stages. Other error sources in aerosol classification with cascade im-

Factors are wall losses, rebound of particles from the collection plates, re-entrainment and disaggregation of collected particles. Nevertheless, at present cascade impactors are still the most widely used instruments for the classification of atmospheric aerosol. The reasons for this are the simplicity of operation of the impactors and their large aerosol sampling flows (from 17.5 l/min [59], up to 85 l/min [58]. An exception is the Lovelace impactor [65], the sampling flow of which is about 0.1 l/min).

Judging the cascade impactor as a possible aerosol classifier in the present study, it must be remarked that disaggregation of collected particles, which may occur, would be disastrous. Furthermore the classification achieved with cascade impactors is rather poor in the aerodynamic diameter range below 2 μm . Particles having aerodynamic diameters below 2 μm are divided by cascade impactors in 2 or 3 classes. An exception forms the Lovelace device, which classifies particles with aerodynamic diameters between 0.12 μm and 2.2 μm in 7 size classes.

A single stage impactor has been designed by Zebel and Hochrainer [115]. This impactor classifies aerosol particles over a continuous aerodynamic diameter region, in contrast to cascade impactors, which classify particles into discrete classes. Zebel and Hochrainer's device is based on the separation possibility of the impact mechanism as is shown in figure I.8.

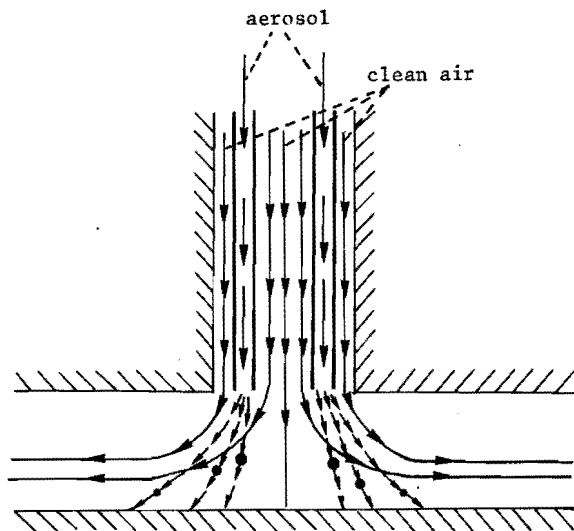


Figure I.8. Separation principle of a single stage impactor.

The velocity at which particles leave the gasstream depends on their aerodynamic diameter. As a result the distance of the particles deposition location from the centre decreases with increasing aerodynamic diameter (cf. figure I.8).

The single stage impactor described above, deposits particles according to their aerodynamic diameters in concentric circles. The original calibration data of Zebel and Hochrainer show that the instrument is capable of classifying particles in the aerodynamic diameter region from 4 μm down to 0.5 μm corresponding to deposition circles with diameters of 0.3 mm up to 1.3 mm.

It can be concluded that this single stage impactor is a handy apparatus for industrial hygiene control purposes, but its classification capacity is too poor to be used for aerosol classification in the present study.

I.3. Systematic errors

The measurement of aerodynamic diameters by the methods described above may include a systematic error due to the difference between the conditions of the particles settling in the instrument and in the practical

situation. These differences are connected with the nature and the strength of the forces applied. The different settling conditions might result in an orientation of the particles during settling in the instrument, deviating from the orientation of the particles in their practical situation. This may cause a difference between the measured aerodynamic diameters and the aerodynamic diameters the particles show in the practical situation.

Furthermore the difference between the settling rates of the particles in the instrument and their practical situation may cause measuring errors, because of a possible dependence of dynamic shape factors on the Reynolds number (Re). Furthermore in case Re becomes larger than 0.1 there will be deviations of the fluid drag from equation (2.2.1), due to fluid inertia effects.

The above mentioned phenomena will be discussed further, especially with respect to the aerodynamic diameter classifiers discussed in the previous section.

Particle orientation

The influence of the orientation of a particle on its dynamic shape factor and therefore on its aerodynamic diameter, may be considerable as has been shown in chapter 2 with respect to cylinders and spheroids. In chapter 2 it was also remarked, that, due to the Brownian rotation, particles will undergo a random change of orientation, unless forces acting on the particles are strong enough to counteract the Brownian rotation and to have the particles adopt a specific orientation.

Generally submicron aerosol particles will not adopt a specific orientation due to gravitational forces. Therefore if submicron particles adopt a specific orientation in the aerodynamic diameter classifier, a systematic error may be introduced in the measurement.

Boose and Hochrainer [5] studied the orientation of doublets of submicron monodisperse polystyrene spheres in an electric mobility analyser. Their results show the doublets to be oriented mostly with their axis parallel to the electric field. A similar study done by Hochrainer [40] with respect to centrifuges, showed no specific orientation of doublets of monodisperse submicron spheres in the centrifugal field. However, the results of his study of dynamic shape factors of linear chains of submicron monodisperse spheres, made Stöber [93] suggest that in the Stöber centrifuge these linear chains preferably deposit with their axis perpendicular to the settling direction. This suggestion was dictated by the agreement of his results with the dynamic shape factors of prolate spheroids settling with their polar axis perpendicular to the direction of settling (eq. 2.2.5).

Concerning the impactors no experimental results with respect to the orientation of the particles during settling are known. Undoubtedly the effect of preferred orientation in impactors will be at least of the same order as in centrifuges.

Summarizing it can be said that the tendency of the particles to adopt a preferred orientation different from random orientation will be significant in electric mobility analysers. In centrifuges and impactors this tendency will be much smaller, while in elutriators and Millikan chambers (when no tension applied) this effect will be absent of course.

Reynolds number

To allow aerodynamic diameter evaluation in the submicron range, forces in aerodynamic diameter classifiers have to be much larger than gravity in order to make the particles settle sufficiently rapid. The Reynolds number corresponding to the particle settling velocity in the instrument therefore, will be much larger than in the practical situation.

Equation (2.2.21) shows that a dependence of κ on Re will cause an erroneous aerodynamic diameter evaluation. For $Re < 0.1$ it is generally accepted that κ will be independent of Re , and although the results of Pich (eq. 2.2.8) cast some doubt on this, in most practical cases this assumption will not be far from correct. For $Re > 0.1$, however, κ may significantly vary with Re as has been shown by Hochrainer and Hänel [41]. If in the classifier Re becomes larger than 0.1, besides the dependency of κ on Re , the measurements might be subject to a systematic error because equation (2.2.1) and therefore (2.2.21) do not hold for $Re > 0.1$. For $Re < 6$, the fluid drag on a particle is given by [32]:

$$F = \left\{ - \frac{3\pi\eta\kappa(Re)d_e v}{C_s(d_e)} \right\} \left\{ 1 + 0.13 Re(d_e)^{0.85} \right\} \quad (I.3.1)$$

with: $Re(d_e) = d_e \rho_g v / \eta$
 ρ_g = density of the fluid.

This leads to the following expression:

$$d_a^* = \left\{ \frac{1}{\kappa(Re)} \right\}^{\frac{1}{2}} \left(\frac{\rho}{\rho_0} \right)^{\frac{1}{2}} \left\{ \frac{C_s(d_e)}{C_s(d_a^*)} \right\}^{\frac{1}{2}} d_e \left\{ \frac{1 + 0.13 Re(d_e)^{0.85}}{1 + 0.13 Re(d_a^*)^{0.85}} \right\} \quad (I.3.2)$$

with: d_a^* = aerodynamic diameter measured with the classifier
 $Re(d_a^*) = d_a^* \rho_g v / \eta$

From equations (I.3.2) and (2.2.21) one obtains:

$$d_a = \left\{ \frac{C_s(d_a^*)}{C_s(d_a)} \right\}^{\frac{1}{2}} \left\{ \frac{\kappa(Re)}{\kappa} \right\}^{\frac{1}{2}} \left\{ \frac{1 + 0.13 Re(d_a^*)^{0.85}}{1 + 0.13 Re(d_e)^{0.85}} \right\} d_a^* \quad (I.3.3)$$

where d_a is the aerodynamic diameter of the particle in creeping motion. Equation (I.3.3) shows that when the Reynolds number corresponding to the particle settling in the classifier is larger than 0.1, there will be a

significant deviation between the measured aerodynamic diameter (d_a^*) and the aerodynamic diameter of the particle in creeping motion (d_a) one is interested in.

With respect to the classifiers discussed in paragraph (I.2), the phenomena discussed above are only of interest for impactors and electric mobility analysers, in which the Reynolds number corresponding to the settling of a particle may be considerably above 0.1.

I.4. Conclusion

In conclusion the aerosol classifier to be used in this study has to be chosen from the classifiers discussed in (I.2). Therefore these instruments have to be compared with respect to the demands the classifier has to satisfy. These demands are:

1. An accurate aerodynamic diameter classification for diameters smaller than 2 μm ;
2. It must be possible to study the structure of the particles in relation to their aerodynamic diameters.

Although measurements with elutriators are not troubled by the phenomenon causing systematic errors (I.3), this classifier is unsuitable for the present study because of its very limited applicability in the submicron range. Millikan chambers may be more useful in this range, especially when an electric field is applied. Millikan chambers, however, do not satisfy the second demand mentioned above. Thus Millikan chambers must also be removed from the list of candidate classifiers. Remain electric mobility analysers, centrifuges and impactors.

The inferior accuracy of impactors, together with the difficulties arising in aerodynamic diameter evaluation of non-spherical particles with electric mobility analyser, and the large systematic errors in these instruments lead to the choice of a centrifuge for the present study. From the known centrifugal classifiers the spiral centrifuge according to Stöber and Flachsbarth is chosen because this instrument meets the demands most perfectly.

APPENDIX II. THE POINT TO PLANE ELECTROSTATIC PRECIPITATOR

Extraction of particles from the gas phase by an electric field while they are simultaneously charged, is called electrostatic precipitation. This mechanism is widely used in industrial filters.

Morrow and Mercer employed the electrostatic precipitation mechanism in a device by which aerosol particles can be sampled directly on an electron microscope grid. This device, the so-called point to plane electrostatic precipitator (E.S.P.), is shown schematically in figure II.1.

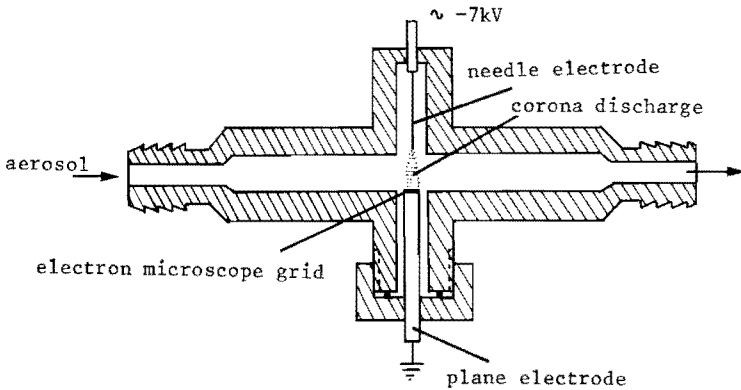


Figure II.1. Schematic picture of the point to plane electrostatic precipitator (E.S.P.) according to Morrow and Mercer [68].

The aerosol is drawn through a corona discharge which is generated between the needle electrode and the plane electrode. The former is kept at a high negative tension (about 7 kV), while the latter is grounded. In the corona discharge the aerosol particles are charged by collisions with negative ions. Consequently, the particles are deposited by electrical forces on a carbon coated electron microscope grid, which is placed on the plane electrode.

The sampling efficiency of the E.S.P. with respect to the particle size has been studied by van de Vate [106]. He sampled a polydisperse NaCl aerosol as well as monodisperse polystyrene test aerosols with two

E.S.P.'s placed in series. The deposit density as well as the particle size distribution of both samples was evaluated by means of electron microscopy. From these data the collection efficiency of the E.S.P. with respect to particle size was calculated. The results of these calculations are shown graphically in figure II.2. They show a collection efficiency of about 90 percent, irrespective of the particle size, in the size range below 1.5 μm , to which region the experiments were confined. Similar experiments carried out in the present study, using the poly-disperse polystyrene test aerosol described in section 3.3, fully confirmed the results of van de Vate. Therefore, it can be concluded that at least in the size range below 1.5 μm an E.S.P. samples non-size-selectively.

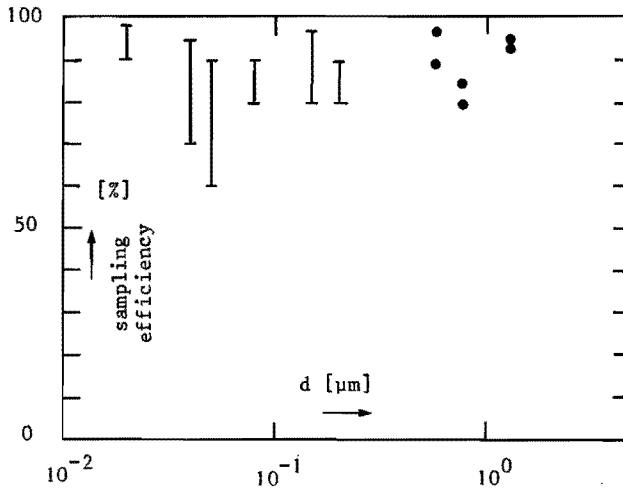


Figure II.2. Sampling efficiency of an E.S.P. with respect to particle size, as obtained by v.d. Vate [106] by means of poly-disperse NaCl test aerosols (I), and monodisperse polystyrene test aerosols (●).

REFERENCES

- [1] A.A. Andersen, J. Bacteriol, 76, (1958), 471.
- [2] D.W. Aylmore and W.B. Jepson, J. Scient. Instr., 38, (1961), 156.
- [3] A.G. Barkow, F.G. Karioris and J.J. Stoffels, Adv. in X-ray Anal., 6, (1963), 210.
- [4] R.A. Beebe, J.B. Beckwith and J.M. Honig, J. Am. Chem. Soc., 67, (1945), 1554.
- [5] Ch. Boose and D. Hochrainer, in Proceedings of "Jahrescongresz 1974 der Gesellschaft für Aerosolforschung", Bad Soden (Germany) (1974).
- [6] S. Brunauer, P.H. Emmett and E. Teller, J. of Am. Chem. Soc., 60, (1938), 309.
- [7] J.H. Burgers, Second report on Viscosity and Plasticity, N.V. Noord-Hollandsche Uitgeversmaatschappij, (Amsterdam), (1933), 199.
- [8] C.J.P. v. Buijtenen and F. Oeseburg, Atmosph. Env., 8, (1974), 885.
- [9] K.C. Chun and J.E. Quon, Env. Sci. Techn., 7, (1973), 532.
- [10] W.E. Clark and K.T. Whitby, J. Atm. Sci., 24, (1967), 677.
- [11] D.J. McConalogue and R.S. Srivastava, Proc. Roy. Soc., A307, (1968), 37.
- [12] M. Corn, Env. Sci. Techn., 5, (1971), 155.
- [13] H. Coudeville, P. Trepaud and E.A. Brun, Rarefied Gas Dynamics 4th Symp., 1, (1965), 44.
- [14] R.A. Cox, Tellus, 26, (1974), 235.
- [15] B.E. Dahneke, J. of Aerosol Sci., 4, (1973), 139.
- [16] B.E. Dahneke, J. of Aerosol Sci., 4, (1973), 147.
- [17] B.E. Dahneke, J. of Aerosol Sci., 4, (1973), 163.
- [18] C.N. Davies, Chem. and Ind., (1974), 441.

- [19] C.N. Davies, in Proceedings of "Jahrescongresz 1973 der Gesellschaft für Aerosolforschung, Bad Soden, (Germany), (1973).
- [20] C.N. Davies. J. of Aerosol Sci., 5, (1974), 293.
- [21] C.N. Davies, in Proceedings of Phys. Soc. of London, B63, (1950), 288.
- [22] R.T. Davis, T.W. de Witt and P.H. Emmett, J. Phys. Chem., 51, (1947), 1232.
- [23] G. Devitofrancesco and B. Sperduto, Staub, 30, (1970), 440.
- [24] G.A. Ferron and H.W.J. Bierhuizen, Aerosol Sci., 7, (1976), 5.
- [25] R.K. Finn, J. of Appl. Phys., 24, (1953), 771.
- [26] C.N. Fuchs, The Mechanics of Aerosols, (1964), Pergamon Press, (Oxford).
- [27] N.A. Fuchs and Stechkina, Trans. Faraday. Soc., 58, (1962), 1949.
- [28] F. Galton, Proc. of Roy. Soc. of London, 29, (1879), 365.
- [29] A. Goetz, Geofis. Pura. Appl., 36, (1957), 49.
- [30] S.J. Gregg and K.S.W. Sing, Adsorption, Surface Area and Porosity, (1967), Academic Press, (London).
- [31] G. Hänel, Atm. Env., 4, (1970), 289.
- [32] G. Hänel, Atm. Env., 3, (1969), 69.
- [33] J. Happel and H. Brenner, Low Reynolds number Hydrodynamics, (1973), Noordhoff. Intern. Publ., (Leyden).
- [34] T.F. Hatch and P. Gross, Pulmonary Deposition and Retention of Inhaled Particles, (1964), Academic Press.
- [35] R.A.W. Haul, Angew. Chem., 68, (1956), 238.
- [36] M.J. Heard, A.C. Wells and R.D. Wiffen, Atm. Env., 4, (1970), 381.
- [37] J.F. Heiss and J. Coull, Chem. Eng. Progress, 48, (1952), 133.
- [38] J. Heyder and J. Porstendörfer, Aerosol Sci., 5, (1974), 387.
- [39] D. Hochrainer, J. Colloid. and Interf., 36, (1971), 191.
- [40] D. Hochrainer, Staub, 33, (1973), 320.
- [41] D. Hochrainer and G. Hänel, Aerosol Sci., 6, (1975), 97.
- [42] H. Horvath, Staub, 34, (1974), 251.

- [43] F.K. Hurd and J.C. Mullins, *J. Colloid Sci.*, 17, (1962), 91.
- [44] H.S. Judeikis and S. Siegel, *Atm. Env.*, 7, (1973), 619.
- [45] C. Junge, *Air Chemistry and Radioactivity*, (1963), Academic Press.
- [46] F.G. Karioris and B.R. Fish, *J. of Coll. Sci.*, 17, (1962), 155.
- [47] W. Kast, *Staub*, 21, (1961), 215.
- [48] C.N. Keith and J.C. Derrick, *J. Coll. Sci.*, 15, (1960), 340.
- [49] M. Knudsen and S. Weber, *Ann. Physik*, 36, (1911), 982.
- [50] P. Kotrappa and M.E. Light, *Rev. Sci. Instr.*, 43, (1972), 1106.
- [51] F. Kottler, *J. of Phys. Chem.*, 56, (1952), 442.
- [52] F. Kottler, *J. of Franklin Inst.*, 250, (1950), 339.
- [53] W.B. Kunkel, *J. Appl. Phys.*, 19, (1948), 1056.
- [54] H. Lamb, *Hydrodynamic* 6th Ed., (1932), Cambridge Univ. Press, 613.
- [55] I. Langmuir, *J. Am. Chem. Soc.*, 37, (1915), 1137.
- [56] S. Laskin, in *Pharmacology and Toxicology of Uranium Compounds I*, (1949), ed. Voegtlin and Hodge, McGraw-Hill, (New York), 463.
- [57] R.E. Lee, *Env. Sci and Techn.*, 6, (1972), 1025.
- [58] D. Lundgren, *Apca J.*, 17, (1967), 225.
- [59] K.R. May, *J. Sci. Instr.*, 22, (1945), 187.
- [60] D. McAllister, *Proc. of Roy. Soc. of London*, 29, (1879), 367.
- [61] J.S. McNown and J. Malaika, *Tras. Am. Geophys. Union*, 31, (1950), 74.
- [62] W.J. Megaw and R.D. Wiffen, *J. Rech. Atm.*, 2, (1966), 69.
- [63] W.J. Megaw and A.C. Wells, *J. of Sci. Instr.*, 2, (1969), 1013.
- [64] T.T. Mercer, *Aerosol Technology in Hazard Evaluation*, (1973), Academic Press, London, 204.
- [65] T.T. Mercer, M.I. Milton and G.J. Newton, *J. Aerosol Sci.*, 1, (1970), 9.
- [66] R.A. Millikan, *The Physical Rev.*, 22, (1923), 1.
- [67] F.J. Mönig, N. Schwarzer and W. Stöber, in *Proceedings of "Jahreskongress der Gesellschaft für Aerosolforschung"*, Bad Soden, (Germany), (1973).

- [68] P.E. Morrow and T.T. Mercer, *Am. Ind. Hyg. Ass. J.*, 25, (1964), 8.
- [69] T. Navakov, S.G. Chang and A.B. Harker, *Science*, 186, (1974), 259.
- [70] F. Oeseburg, F.M. Benschop and R. Roos, *J. of Aerosol Sci.*, 6, (1975), 421.
- [71] F. Oeseburg and R. Roos, *Atm. Env.*, 9, (1975), 859.
- [72] C. Orr and J.M. Dalla Valle, *Fine particle measurements*, (1938), The McMillan Company, (New York).
- [73] A. Overbeck, *Crelles J. Math.*, 81, (1876), 62.
- [74] R.F. Phalen, *Aerosol Sci.*, 3, (1972), 395.
- [75] J. Pich, *Coll. and Int. Sci.*, 29, (1969), 91.
- [76] J. Porstendörfer and J. Heyder, *Aerosol Sci.*, 3, (1972), 141.
- [77] T.J.M. Pouw, J.F. v.d. Vate and H. Spoelstra, in *Proceedings of the "Jahrestagung 1975 der Gesellschaft für Aerosolforschung"*, (1975).
- [78] M.J. Prager, E.R. Stephens, and W.E. Scott, *Ind. Eng. Chem.*, 52 (1960), 521.
- [79] O. Preining, in *Proceedings of "Jahreskongress 1974 der Gesellschaft für Aerosolforschung"*, (1974).
- [80] O. Preining, *Atm. Env.*, 1, (1967), 271.
- [81] O.G. Raabe, *Aerosol Sci.*, 2, (1971), 289.
- [82] M.B. Ranada, D.T. Wasan and R. Davies, *Am. Inst. Chem. Engrs. J.*, 20, (1974), 273.
- [83] N.A. Renzetti and G.J. Doyle, *Int. J. Air Poll.*, 2, (1960), 327.
- [84] D. Rimberg and J.W. Thomas, *J. Coll., Sci.*, 32 (1970), 101.
- [85] A.J. Rosenberg, *J. Phys. Chem.*, 51, (1947), 1232.
- [86] K.F. Sawyer and W.H. Walton, *J. Sci. Instr.*, 27, (1950), 272.
- [87] K.S.W. Sing, and D. Swallow, *Proc. Brit. Ceram. Soc.*, 5, (1965), 39.
- [88] F. Stein, R. Quinlan and M. Corn, *Am. Ind. Hyg. Ass. J.*, 28, (1966), 39.
- [89] A.C. Stern, *Air Pollution 2nd Ed.*, vol. 1, (1968), Academic Press, 15.

- [90] H.J.R. Stevenson, D.E. Sanderson and A.P. Altshuller, *Int., J. Air. Wat. Poll.*, 9, (1965), 367.
- [91] K. Stewart, *Trans. of Faraday Soc.*, 52, (1956), 161.
- [92] W. Stöber, Assessment of Airborne Particles, ed. by Mercer, Morrow and Stöber, Charles C. Thomas, Springfield, Illinois, (1972), 249.
- [93] W. Stöber, Design, Performance and Applications of Spiral duct Aerosol Centrifuges, presented at Symposium on fine particles, Minneapolis (U.S.A.), May 1975.
- [94] W. Stöber, *Aerosol Sci.*, 2, (1971), 453.
- [95] W. Stöber and H. Flachsbart, *Env. Sci. Techn.*, 3, (1969), 1280.
- [96] W. Stöber and H. Flachsbart, *Aerosol Sci.*, 2, (1971), 103.
- [97] W. Stöber and H. Flachsbart, *Atm. Env.*, 7, (1973), 737.
- [98] W. Stöber, H. Flachsbart and C. Boose, *J. Coll. Interf. Sci.*, 39, (1972), 109.
- [99] W. Stöber, H. Flachsbart and D. Hochrainer, *Staub*, 30, (1970), 277.
- [100] K.E. Stumpf, *Anorg. und Allg. Chem.*, 270, (1952), 114.
- [101] Task Group on Lung Dynamics, *Health Phys.*, 12, (1966), 173.
- [102] J.W. Thomas and R.H. Knuth, *Am. Ind. Hyg. Ass. J.*, 28, (1967), 229.
- [103] M.I. Tillery, in Assessment of Airborne Radioactivity, I.A.E.A., Vienna, (1967).
- [104] M.I. Tillery, *Am. Ind. Hyg. Ass. J.*, 35, (1974), 62.
- [105] V. Timbrell, in Assessment of Airborne Particles, ed. by Mercer, Morrow and Stöber, C.C. Thomas, Springfield, Illinois, (1972), 290.
- [106] J.F. v.d. Vate, The safety of S.N.R.-300 and the aerosol model; A summary report of the R.C.N. Aerosol research 1967-1971, R.C.N.-report 174 (Holland), (1972).
- [107] A.J. Vogel, A textbook of quantitative inorganic analysis, 3rd ed., Longmans, London (1962), 787.
- [108] R.A. Vomela and K.T. Whitby, *J. Coll. and Interf. Sci.*, 25, (1967), 568.
- [109] L. Waldmann and K.H. Schmitt, in Aerosol Science, ed. Davies, Academic Press, New York, (1966), 137.

- [110] K.T. Whitby and W.E. Clark, *Tellus*, 18, (1966), 573.
- [111] C.M. White, *Proceedings of the Roy. Soc.*, A186, (1946), 472.
- [112] R. Whytlaw-Gray and H.S. Patterson, Smoke, Edwards Arnold, London (1932).
- [113] M. de Wit, Approximate solutions to boundary layer problems in linear kinetic theory, Thesis, T.H. Eindhoven (Holland), (1975).
- [114] N.G. Wrigley, *J. Ultrastruct. Res.*, 24, (1968), 454.
- [115] G. Zebel, and D. Hochrainer, *Staub*, 32, (1972), 91.

LIST OF FREQUENTLY USED SYMBOLS

A	= empirical constant (cf. equation 2.1.4)
A_m	= area occupied per molecule of adsorbate
B	= empirical constant (cf. equation 2.1.4)
b	= coordinate on centrifuge strip (cf. figure 3.1)
b_r	= reference length (cf. equation 3.2.9)
c	= constant in B.E.T.-equation (cf. equation 5.2.3)
$C_s(d)$	= slip correction factor for a sphere (equation 2.1.4)
$C_n(Kn)$	= slip correction factor for a non-spherical particle
C'_n	= slip correction factor for a linear aggregate
C''_n	= slip correction factor for a three-dimensional network
d	= diameter of a sphere
\bar{d}_1	= mean diameter of the primary particles
d_{lg}	= geometric mean diameter of the primary particles
d_a	= aerodynamic diameter
d_c	= diameter of a cylinder
d_e	= volume equivalent diameter
d_p	= projected area diameter
d_{se}	= diameter of a sphere with the same surface area as the particle
F	= friction force exerted by the gas on the moving particle
f_1	= proportionality factor (cf. equation 4.3.7)
f_2	= constant (cf. equation 4.3.13)
K	= constant (cf. equation 4.4.2)
k_1	= proportionality factor (cf. equation 4.3.6)
k_2	= constant (cf. equation 4.3.12)
Kn	= Knudsen number = \bar{l}/L_c
L	= length of a cylinder
L_c	= characteristic length of a particle = $\frac{1}{2}d$ for a sphere
l	= coordinate on deposition strip of centrifuge (cf. figure 3.1)
\bar{l}	= mean free path of the gas molecules
m	= mass of an aggregate
n	= number of primary particles in an aggregate
$P(d_a)$	= probability function (cf. section 3.2)

p	= gas pressure
p_0	= saturation pressure of the gas
Q	= empirical constant (cf. equation 2.1.4)
q	= aspect ratio of a spheroid
r	= roughness factor = S_{BET}/S_{GEOM}
Re	= Reynolds number = $2L_c \rho_g v/\eta$
S	= specific surface area
S_{BET}	= specific surface area calculated from gas adsorption data
S_{GEOM}	= specific surface area calculated from particle dimensions
$T_{1,2,3}$	= cooling temperatures of the centrifuge rotor (cf. figure 3.9)
v	= velocity of a particle
w	= constant (cf. equation 2.2.17)
x	= amount of adsorbed gas
x_m	= monomolecular layer capacity of a sample
η	= dynamic viscosity of the gas
κ	= dynamic shape factor
$\kappa_{c\parallel}$	= dynamic shape factor of a cylinder moving parallel to its axis (cf. equation 2.2.6)
$\kappa_{c\perp}$	= dynamic shape factor of a cylinder moving perpendicular to its axis (cf. equation 2.2.8)
$\kappa_{p\parallel}$	= dynamic shape factor of a prolate spheroid moving parallel to its polar axis (cf. equation 2.2.4)
$\kappa_{p\perp}$	= dynamic shape factor of a prolate spheroid moving perpendicular to its polar axis (cf. equation 2.2.5)
$\tilde{\kappa}$	= $\kappa \cdot C_s(d_a)/C_s(d_e)$
κ_s	= dynamic surface area shape factor (cf. equation 4.3.14)
ρ	= density of the particles
ρ_0	= unit density = 1 g/cm^3
ρ_g	= gas density
σ_{1g}	= geometric standard deviation of the primary particle size distribution
ϕ	= sphericity = d_e^2/d_{se}^2
$\phi^*(1)$	= surface density of the deposit at the location 1 on the centre line of the collection foil
$\Phi(d_a)$	= aerodynamic diameter distribution
$\Phi^*(d_a) dd_a$	= number of particles entering the centrifuge with an aerodynamic diameter between d_a and $d_a + dd_a$
$(\omega^2)^{\frac{1}{2}}$	= mean Brownian rotation velocity

SUMMARY

This thesis deals with the physical characterisation of branched chain-like aggregates. These aggregates are frequently found in polluted air. They are produced inter alia by combustion of hydrocarbon fuels (e.g. in automobile engines) and by condensation of metallic vapors (e.g. near iron works). They are composed of a large number of primary particles. An important factor determining the health hazard of the aggregates is their aerodynamic behaviour. Furthermore, the specific surface area is an important parameter with respect to their role in atmospheric chemistry. Both the aerodynamic behaviour and the specific surface area depend on the microstructure of the aggregates, i.e. the number, and size distribution of the primary particles. The purpose of this study was to arrive at a detailed evaluation of this dependence.

Most of the experimental work was carried out with aggregates prepared by the exploding wire method. In this method a capacitor is discharged very rapidly through a metallic wire, causing the dispersion of the wire. The coagulates produced in this way are rather similar to aggregates found in the atmosphere. Aggregates of different primary particle size distributions can be obtained by varying the specific explosion energy. Studied were iron oxide, gold, and copper oxide aggregates, produced by exploding respectively iron, gold, and copper wires. Furthermore, a fluorescein aerosol was studied, produced by spraying a solution of ammonia-fluorescein.

Chapter 2 contains a theoretical treatment of the motion of small particles in a gas. Special attention is paid to the shape of the particles and to the influence of viscous slip.

In chapter 3 the calibration of an aerosol centrifuge, as developed by Stöber, is discussed. In such a centrifuge aerosol particles are deposited on a removable deposition strip, separated according to their aerodynamic diameter. This quantity is defined as the diameter of a sphere with unit

density ($= 1 \text{ g/cm}^3$) having the same settling velocity as the aggregate. From a discussion of existing methods for measuring aerodynamic diameters, given in appendix I, it is concluded that this aerosol centrifuge is the most suitable apparatus for the purpose of the present study. From the calibration experiments the relation between the aerodynamic diameter and the location of deposition of the particles was obtained. In addition, data needed for a proper measurement of the aerodynamic diameter distribution were evaluated.

In chapter 4 the experiments dealing with the aerodynamic characterisation of the aggregates are reported. For this purpose, the aggregates were separated according to their aerodynamic diameters with the aerosol centrifuge. The size distribution of the primary particles was obtained by means of electron microscopy, using negatively stained catalase crystals as an internal length standard. The results show that the relation between the aerodynamic diameter and the number of primary particles (n) of the aggregates can be divided into two regions. For n up to a certain critical value the aerodynamic diameter was found to be proportional to $n^{1/6}$, which corresponds with the aerodynamic behaviour of more or less linearly shaped aggregates. For n above this critical value the aerodynamic diameter was found to be proportional to $n^{1/3}$, corresponding with the behaviour of irregularly shaped three-dimensional networks.

In chapter 5 the results obtained for the specific surface area of iron oxide aggregates are reported. The specific surface areas are found by application of the B.E.T. method, using krypton as the adsorbed gas at a temperature of 78.8 K. The results do not deviate far from the specific surface areas calculated from the size distribution of the primary particles.

SAMENVATTING

Dit proefschrift handelt over de fysische karakterisering van vertakte ketenvormige koagulaten. Dergelijke aerosol deeltjes komen vaak voor in verontreinigde lucht. Zij worden o.a. gevormd bij verbranding van koolwaterstoffen (bv. in automotoren) en door condensatie van metallische dampen (bv. nabij ijzergieterijen). Ze zijn opgebouwd uit een groot aantal primaire deeltjes. Het aerodynamische gedrag van de koagulaten bepaalt in belangrijke mate hun schadelijkheid voor de gezondheid. Bovendien is hun specifieke oppervlakte een belangrijke parameter in verband met hun rol in chemische processen in de atmosfeer. Het aerodynamische gedrag en de specifieke oppervlakte zijn beide afhankelijk van de microstructuur van de koagulaten (aantal, en grootte-verdeling van de primaire deeltjes). De doelstelling van dit proefschrift was de vaststelling van deze relaties.

Het experimentele werk was grotendeels gericht op koagulaten gevormd met de "exploding wire" methode. Het principe van deze method is, dat een hoogspanningscondensator momentaan over een metaaldraad ontladen wordt, waardoor deze draad overgaat in de disperse vorm. De zo gevormde koagulaten gelijken sterk op de koagulaten gevonden in de atmosfeer. Koagulaten met verschillende grootte-verdelingen van de primaire deeltjes kunnen gevormd worden door variatie van de specifieke explosie-energie. Bestudeerd zijn ijzer-oxide, goud, en koper-oxide koagulaten, geproduceerd door de explosie van respectievelijk ijzer-, goud- en koperdraden. Verder is ook een fluorescine aerosol bestudeerd. Dit werd gegenereerd door versproeiing van een oplossing van ammonium-fluorescine.

In hoofdstuk 2 wordt de beweging van een deeltje in een gas theoretisch behandeld. In het bijzonder wordt aandacht besteed aan de deeltjesvorm en aan de invloed van visceuse slip.

In hoofdstuk 3 wordt de ijking beschreven van een aerosol centrifuge, ontwikkeld door Stöber. In een dergelijke centrifuge worden aerosol deeltjes naar hun aerodynamische diameter gescheiden, waarbij zij worden

neergeslagen op een uitneembare depositiestrip. De aerodynamische diameter is gedefinieerd als de diameter van een bolletje met een dichtheid van 1 g/cm^3 en dezelfde valsnelheid als het koagulaat. Uit de in appendix I gegeven discussie van bestaande methoden ter bepaling van aerodynamische diameters is geconcludeerd, dat een dergelijke aerosol centrifuge het meest geschikt is voor de doelstelling van dit proefschrift. De beschreven ijking leverde de relatie tussen de aerodynamische diameter en de depositieplaats van de deeltjes. Bovendien werden de benodigde gegevens verkregen voor nauwkeurige bepalingen van de verdeling der aerodynamische diameters.

In hoofdstuk 4 worden de experimenten ter verkrijging van de aerodynamische karakteristieken van de aggregaten beschreven. Hiertoe werden de aggregaten met behulp van de aerosol centrifuge naar hun aerodynamische diameter gescheiden. De primaire deeltjes grootte-verdelingen werden verkregen door middel van electronenmicroscopie, waarbij "negatively stained" catalase kristallen als een interne lengte standaard gebruikt werden. De resultaten tonen, dat de relatie tussen de aerodynamische diameter en het aantal primaire deeltjes (n) van de koagulaten verdeeld kan worden in twee gebieden. Voor n beneden een zekere kritische waarde bleek de aerodynamische diameter evenredig te zijn met $n^{1/6}$, hetgeen overeenkomt met het aerodynamische gedrag van min of meer lineaire koagulaten. Voor n boven deze kritische waarde is de aerodynamische diameter evenredig met $n^{1/3}$, hetgeen overeenkomt met het gedrag van onregelmatig gevormde driedimensionale netwerken.

In hoofdstuk 5 worden de specifieke oppervlaktebepalingen aan ijzer-oxide koagulaten beschreven. De specifieke oppervlakte werd door middel van de B.E.T.-methode bepaald uit de adsorptie-isotherm van krypton by 78.8 K. De resultaten wijken niet ver af van de specifieke oppervlakten berekend uit de verdelingsfunctie van de primaire deeltjesgrootte.

CURRICULUM VITAE

De samensteller van dit proefschrift werd geboren op 3 juli 1948 te Oosterhout(N.Br.). Na de lagere school, bezocht hij het Mgr. Frencken-college te Oosterhout, waar hij in 1965 het diploma H.B.S.-B behaalde.

In september 1965 begon hij de studie aan de Technische Hogeschool te Eindhoven aan de afdeling Technische Natuurkunde. Zijn afstudeerwerk verrichtte hij in de groep Warmte- en Materietransport onder leiding van prof. dr. D.A. de Vries. Het onderzoek omvatte een experimenteel onderzoek naar de diffusie van waterdamp door diverse gassen, alsmede een theoretisch onderzoek naar het transport van een gas langs een vlakke wand onder invloed van een temperatuurgradiënt. Op 28 januari 1971 behaalde hij het doctoraal examen.

Na zijn militaire dienstplicht vervuld te hebben, trad hij in november 1972 in dienst van Reactor Centrum Nederland. Hier verrichtte hij onderzoek aan sterk gekoaguleerde aerosoldeeltjes, welke studie ten grondslag ligt aan dit proefschrift.

Sinds juli 1975 is hij in dienst van Ultra-Centrifuge Nederland N.V.

Stellingen behorende bij het proefschrift van J.A.M.M. Kops.

1. Het meten van quasi-monodisperse verdelingen met aerosolcentrifuges is af te raden.

Dit proefschrift paragraaf 3.5.

2. In zijn argumentatie voor het gebruik van een "exploding wire" aerosolgenerator voor inhalatieëxperimenten gaat Phalen voorbij aan het feit dat bij deze methode stikstofoxiden gevormd worden.

R.F. Phalen, J. Aerosol Sci., 3, (1972), 395.

3. De door Eerkens gevonden verrijgingsfactor voor een verrijgingsproces van uranium door selectieve excitatie van UF_6 moleculen, gevolgd door een chemische reactie, indiceert dat deze methode een cascadeproces vereist. Dit cascadeproces zal echter ernstig bemoeilijkt worden door de benodigde chemische omzetting van het reactieproduct tot UF_6

Laser Focus, dec. 1975, 24, en Laser Focus, jan. 1976, 39.

4. Gegevens over aerosol-gas interacties die zijn verkregen uit experimenten waarbij het aerosol eerst wordt gestabiliseerd op een dragermateriaal, kunnen niet zonder meer geëxtrapoleerd worden naar atmosferische omstandigheden.

R.T. Cheng, J.O. Frohlinger en M. Corn, J. of Air Pollut. Control Ass., 21, (1971), 138.

M. Corn en R.T. Cheng, J. Air Pollut. Control Ass., 22, (1972), 870.

B.M. Smith en J. Wagman, Env. Sci. Technol., 3, (1969), 558.

5. Bij verhoging van de wanddruk in een gascentrifuge zal het potentiële scheidend vermogen door een maximum gaan, niettegenstaande het feit dat het theoretische scheidend vermogen, zoals geformuleerd door Cohen, geen functie van de wanddruk is.

K.P. Cohen, The theory of isotope separation as applied to the large scale production of U-235, Mc. Craw Hill, New York, (1951).

J.J.H. Brouwers, On the motion of a compressible fluid in a rotating cylinder, Thesis T.H.T., juni 1976.

6. De electrochemische oxidatie van benzaldehyde aan een kwikelectrode kan niet worden toegeschreven aan een oppervlaktreactie met kwikoxiden, zoals wordt gedaan door Manousek en Volke.

O. Manousek en J. Volke, J. Electroanal. Chem., 43, (1973), 365.

J. Bover en P. Zuman, J. Electrochem. Soc., 122, (1975), 368.

P. Zuman en T.J.M. Pouw, J. Electroanal. Chem., 67, (1976), 387.

7. Om snel te kunnen komen tot een efficiënte bewaking van het milieu dient er snel een betere samenwerking tot stand te komen tussen de op dit gebied werkzame researchinstellingen en de controlediensten (R.I.V., D.C.M.R., en de Provinciale Waterstaten), alsmede tussen de controlediensten onderling.

J.A.M.M. Kops

28 september 1976